DESIGN, MODELING AND EXPERIMENTAL VERIFICATION OF A NONLINEAR ENERGY SINK BASED ON A CANTILEVER BEAM WITH SPECIALLY SHAPED BOUNDARIES

A Dissertation

Submitted to the Faculty

of

Purdue University

by

Christian E. Silva

In Partial Fulfillment of the

Requirements for the Degree

of

Doctor of Philosophy

December 2019

Purdue University

West Lafayette, Indiana

THE PURDUE UNIVERSITY GRADUATE SCHOOL
STATEMENT OF DISSERTATION APPROVAL

Dr. Shirley J. Dyke, Co-Chair

School of Mechanical Engineering

Dr. James Gibert, Co-Chair

School of Mechanical Engineering

Dr. Charles M. Krousgrill

School of Mechanical Engineering

Dr. Jeffrey Rhoads

School of Mechanical Engineering

Dr. Arun Prakash

Lyles School of Civil Engineering

Approved by:

Jay P. Gore

School of Mechanical Engineering

To God.

To Ximena, the love of my life.

To Tomás, Ana, and Milu, our legacy to this world, without you guys this adventure of grad school and earning a Ph.D degree would have been meaningless, empty. I love you beyond reason.

A mis padres y hermanas, que soportaron siete años de nuestra ausencia. Los amo.

ACKNOWLEDGMENTS

I would like to express my deepest appreciation and gratitude to Dr. Shirley Dyke for her continuous support throughout both my Master's and Ph.D. tracks. Her dedication and interest in my academic progress have been paramount in my success. Her suggestions and eminent knowledge have contributed tremendously towards me becoming a critical thinker, an independent researcher and a resourceful experimentalist. Thank you from the bottom of my heart!

Another recipient of my sincere gratitude is my co-advisor, Dr. James Gibert. His patience and availability to meet with me on a regular basis were a fundamental support for the work presented herein. His insights in nonlinear dynamics and advanced math have helped me to understand and expand concepts that would have been overlooked otherwise. Under Dr. Gibert's tutelage I have learned valuable lessons and gained a lifelong friend and, hopefully, collaborator.

Besides my advisor and co advisor, I would like to express my gratitude to the other members of my graduation committee: Dr. Jeffrey Rhoads, Dr. Chuck Krousgrill and Dr. Arun Prakash. Though I met with all of them on a less frequent basis, every time I did I took away valuable ideas and questions that led me to improve and expand this work. Their thorough review and comments on my dissertation certainly elevated the quality of the final document.

I would also like to recognize the institutions that made possible my studies in the U.S.: the Government of Ecuador through the National Secretariat of Science, Technology and Innovation (SENESCYT); the School of Mechanical Engineering at Purdue University; and the Dean of the Graduate School for providing support for the research whose results are presented in this dissertation.

Finally, I won't forget the valuable support and help of my fellow colleagues at the IISL. Their suggestions, ideas and helping hands have been also an important pillar of this accomplishment. Thank you guys!

TABLE OF CONTENTS

LIST OF TABLES

LIST OF FIGURES

Figure Page

Figure Page

ABSTRACT

Silva, Christian E. Ph.D., Purdue University, December 2019. Design, Modeling and Experimental Verification of a Nonlinear Energy Sink Based on a Cantilever Beam with Specially Shaped Boundaries. Major Professors: Shirley J. Dyke and James M. Gibert, School of Mechanical Engineering.

Engineering requirements and system specifications tend to be rather broad in mechanical engineering design. Indeed, users want the broadest possible capabilities of an artifact with the least possible cost. Unfortunately, linear vibration absorbers designed for engineering applications are limited solutions. Most of the passive absorbers available for commercial use, such as tuned mass dampers, work over a very limited bandwidth and require fine tuning procedures and constant maintenance as they may suffer detuning over time. Therefore, innovative solutions are required to overcome these limitations thus enabling a more efficient way of reducing the vibratory response of structures with the least possible addition of mass.

Nonlinear energy sinks are devices that take advantage of nonlinear principles to absorb and dissipate energy produced during the vibration of a host system, in an irreversible way. Several different classes of devices have been proposed by scholars, most of them as proof of concept and experimental prototypes.

This dissertation focuses on the design, modeling, characterization and experimental verification of a class of nonlinear energy sink, based on a cantilever beam vibrating laterally between two specially shaped surfaces that limit the vibration amplitude, thus providing a variable beam length throughout its deflection, therefore producing a smooth nonlinear restoring force. First, a methodology to evaluate and visualize the energy interactions between the nonlinear energy sink and its host structure is developed. Then, an semi-analytical dynamic model for simulating the device

under actual working conditions is proposed, and finally, an experimental verification phase is conducted where the numerical results are verified and correlated.

1. INTRODUCTION

1.1 Motivation

Structural control is an increasingly important area in various fields of engineering, particularly mechanical, civil and aerospace engineering. The mitigation of excessive oscillatory response has been an object of extensive research since the first mass-spring undamped absorber was proposed by Ormondroyd and Den Hartog (1928). A considerable amount of literature has been published on structural control through the use of mass dampers since the mid-twentieth century, where the first closed-form expressions and design parameters for tuned mass dampers (TMD) were proposed, also by Den Hartog (1985). More recent attention has focused on the provision of new methodologies for structural control, which take advantage of emerging technologies, such as computer control, servo-hydraulic systems and signal transmission.

Four types of structural control systems are the most widely used: active, semi-active, passive and hybrid control strategies, the latter being a combination thereof (Elias and Matsagar, 2017). One major drawback of active, semi-active and hybrid structural control strategies is that they rely entirely or partially on the uninterrupted supply of power, which is not always guaranteed, especially in events such as natural disasters. TMDs, on the other hand have become widely popular for oscillation suppression due to their relative simplicity and passive nature. Moreover, there are hundreds of examples where TMDs have been successfully implemented in structures all over the planet, two of the most iconic are the Taipei 100 Tower in China and the Millenium Bridge in London. Existing TMD implementations fail, however, to resolve two salient limitations in their design: 1) they are subject to detuning, either because of changes in the physical characteristics of the TMD itself, or because of structural changes in the base structure, due to normal use and occupancy, and 2) their operation is limited to a very narrow frequency bandwidth, outside of which they becomes considerably less effective, if not counterproductive. TMDs are usually tuned at or around the first natural frequency of the base structure to which they are attached. (Alexander and Schilder, 2009; Yamaguchi and Harnpornchai, 1993)

1.2 Previous work on the theoretical treatment of targeted energy transfer and nonlinear energy sinks

A survey of past and current developments in the fields of targeted energy transfer phenomena (TET) and nonlinear energy sink (NES) devices is presented in this Section with the objective of putting the subjects into perspective.

1.2.1 Targeted Energy Transfer

Recent developments in nonlinear dynamic systems pertaining to vibrations have led to an increased interest in passive nonlinear vibration absorbers, following the realization of nonlinear energy transfer or energy pumpling in linear systems coupled with attached nonlinear mechanical oscillators, reported by Gendelman et al. (2001) (Vakakis and Gendelman, 2001). An ideal one-way transfer of vibratory energy from the base linear structure to the nonlinear attachment, where it finally localizes and dissipates by means of damping has been explained through three mechanisms: 1) fundamental resonance capture (FRC); 2) sub-harmonic resonance capture (SHRC); and 3) nonlinear beating phenomena (Vakakis et al., 2008; Tripathi et al., 2017). Two oscillators experiencing resonance capture vibrate at the same frequency depending on the level of energy that is inserted to the system. This synchronized frequency can be near, or at, the fundamental frequencies of the linear base structure (FRC), or at sub-frequencies of it (SHRC). The important difference between nonlinear and linear resonance capture (also called static mode localization) lies in that the latter occurs at stationary modes that do not change with respect to energy, whereas the former can occur at different frequencies and can vary in time with the amount of energy introduced into the system (Kerschen et al., 2005). Nonlinear energy transfer occurs above a specific level of energy of the system and is enhanced when the nonlinear oscillator is strongly coupled with the linear base oscillator and is weakly damped. A number of researchers have reported the development of devices based on nonlinear principles to reduce the vibrating response of structures through TET (Vakakis et al., 2008; Wierschem, 2014; Gendelman and Alloni, 2015; Kerschen et al., 2007a).

1.2.2 Nonlinear Energy Sinks

One especially interesting class of device based upon nonlinear principles and used for vibratory response reduction of base linear oscillators is the NES.

NESs are passive nonlinear isolation devices whose principal feature is an essentially nonlinear stiffness and a weak damping coefficient. Essentially nonlinear stiffness refers to a spring with nonlinear predominance in its behavior, rather than the usual spring with linear predominance (e.g.: a nonlinear spring with characteristic $F = \beta x^3$, where F is the spring force, β the nonlinear stiffness coefficient, and x the spring displacement). Different types of NESs have been studied extensively in many different configurations, both numerically and experimentally, and for applications to a broad spectra of engineering fields (Lu et al., 2018).

Despite the variety of studies in which NESs have been conceptually designed, characterized and experimentally tested, the existing accounts have only been carried out in laboratory environments without follow-up studies that lead to implementation in actual applications. Indeed, there is still a need and potential for passive nonlinear vibration reduction devices, both at the development and implementation stages. There have been several attempts to find new and more effective designs for NESs, based on **five basic physical principles** that produced different types of nonlinearities: 1) tensioned wires, which typically produce smooth cubic nonlinear restoring forces; 2) masses traveling along special shaped tracks, producing a restoring force shape which depends on the profile of the track (although only smooth cubic cases have been reported); 3) rotating eccentric masses, producing non-smooth type nonlinearities; 4) spring fixtures, also producing cubic smooth nonlinearities, and; 5) NESs having vibro-impact materials in their configuration, which are a combination of a NES with any of the former principles listed with the addition of end-bumpers fabricated from elastomeric materials that produce non-smooth (e.g.: piecewise linear) nonlinear restoring forces. A short survey of some relevant studies in each of these categories follows.

1. NESs based on strain: Commonly known as a wire-type NES, these devices constitute a classic problem in TET and NESs. They are based on the elastic principles of a mass stretching a wire that runs through it between two fixed points while the mass is allowed to travel along a linear trajectory. This motion stretches the wire back and forth, producing a smooth cubic restoring force. Studies by McFarland et al. (2005), Kerschen et al. (2007b), Vakakis et al. (2008) and Wierschem (2014), along with other follow-up reports are some of the most relevant works that evaluate the behavior and performance of such devices both theoretically and experimentally

2. Vibro-impact NESs (VI NESs): These devices combine viscoelastic dissipation with impact dissipation through specially-shaped end-bumpers made from elastomeric materials that contribute to the overall dissipation. The characteristic restoring force profile that such devices produce is in general non-smooth (piecewise linear). Additionally, VI-NESs are easier to fabricate in comparison to wire NES (Gourc et al., 2015). Different configurations of VI NES are reported in studies by Gendelman and Alloni (2015); Wierschem et al. (2013, 2017); Wierschem (2014); and Luo et al. (2014).

3. Rotational NESs (RO NESs): Nonlinear devices conceived for controlling vibration along directions other than the horizontal have been designed based on rotational principles. Common applications found for these types of implemen-

tations are in the aerospace industry. Theoretical and experimental studies of rotational NESs are reported in Al-Shudeifat et al. (2017); Gendelman et al. (2012); Sigalov et al. (2012a,b); Hubbard et al. (2012); and Hubbard et al. (2010).

4. Spring-based NESs: These devices have a principle of operation similar to wire-based NESs. The main difference resides in the springs, which are arranged in oblique directions along with horizontal and vertical springs, instead of using tensioned wires. These systems also provide smooth cubic nonlinearities but slightly different as the sources of this nonlinear profile are combinations of spring constants. Studies on such devices can be found in Gourc et al. (2015); Ramsey and Wierschem (2017); and Gourdon et al. (2007a).

5. Track NESs: A particularly interesting type is the track-type NESs. These devices base their operation on a carriage with a variable mass, which as a consequence of the resisting force, moves along a specially-shaped track profile. The type of nonlinearity produced depends on the profile of the track, a principle very similar to those used in cam design. Some examples of track NESs can be found in Wang et al. (2015a); and Lu et al. (2017).

6. Other cases: Many other numerical studies have covered NES systems in different configurations, particularly for the vertical vibrations of bridges and offshore structures. Although some research has been carried out on evaluating these cases analytically (Izzi et al., 2016; Goyal and Whalen, 2005; Bab et al., 2014; Kani et al., 2016), no studies have been found that surveyed them experimentally.

One major issue in the aforementioned literature is that much of the research up to now has focused on the reduction of vibrations in structures oscillating in horizontal direction, e.g., building structures. There has been few researchers that have investigated TET in vertical vibrations. However, the problem when analyzing NESs in vertical configurations is that the gravity component that interacts with the mass of the NES, creating an offset that is difficult to compensate for when the device is in action (Ramsey and Wierschem, 2017).

Cases of design of experiments involving vibrating structures coupled with NES devices found in literature are varied. In a series of studies, Gourdon and collaborators analyzed the interaction and efficiency of NES connected MDOF systems under earthquake excitations using a spring-type NES (Gourc et al., 2015; Gourdon et al., 2007a,b). Interactions between the base structures and the NESs, but focused on impulse excitations using combinations of wire-type NES and VI NES, are reported in Wierschem (2014); Wierschem et al. (2017); Luo et al. (2014); Wierschem et al. (2013); and Vakakis et al. (2008).

1.3 Energy and power flow in a nonlinear energy sink

Recent developments in nonlinear TET have led to a renewed interest in the experimental analysis of nonlinear systems for applications in structural dynamics and the vibration control of engineering systems. Extensive research regarding TET has been conducted over the past two decades (Kerschen et al., 2007a,b, 2005; McFarland et al., 2004; Mcfarland et al., 2005; Vakakis and Gendelman, 2001; Vakakis et al., 2008), and as a result, it has been conclusively demonstrated that energy from primary linear structures (with one or more degrees of freedom) can be conveyed to an attached secondary nonlinear dissipation mechanism, where it localizes and dissipates, thus reducing the vibratory response of the primary oscillator (Gendelman et al., 2001; Vakakis and Gendelman, 2001).

Two especially interesting applications of nonlinear TET are NES (McFarland et al., 2005; Kerschen et al., 2007a) and energy harvesters (Bernard and Mann, 2018; Kluger et al., 2015; Zhang et al., 2017). NESs have been broadly studied in many different configurations and applications over a vast range of engineering fields. Particularly in mechanical vibrations and structural dynamics, NESs have been analyzed primarily as vibration damping devices with principal energy transfer mechanisms based upon their essential nonlinearities. Unfortunately, despite the variety of studies in which NESs have been conceptually designed (Lamarque et al., 2011; Ramsey and Wierschem, 2017; Al-Shudeifat, 2014), numerically modeled (Nucera et al., 2010; Gendelman et al., 2011; Lu et al., 2017) and experimentally tested (McFarland et al., 2005; Goyal and Whalen, 2005; Mcfarland et al., 2005), most existing accounts have only been carried out in laboratory environments with little evidence of follow-up studies that could lead to implementation into actual applications. There is great potential for the use and implementation of passive NES devices in real structures and systems.

The energy transfer between primary oscillators and NESs occurs irreversibly as long as certain conditions are met, such as the presence of an essential nonlinearity (absence of a linear stiffness component), and low damping on the primary structure (Vakakis et al., 2008). However, in practice, the essential nonlinearity condition is rather difficult to achieve, mainly due to experimental implementation issues that lead to having some degree of small linear stiffness components in the physical setup. Several researchers have reported the presence of small linear stiffness components in their *essentially* nonlinear fixtures as undesired, as it hinders the essential transfer of energy from the primary oscillator (PO) to the NES. An interesting case is documented by Wierschem, who needed to stretch the wire on his nonlinear device, whose working principle is a tensioned wire, to avoid initial sag. This adjustment added linear stiffness to his system (Wierschem, 2014). Another case of the presence of a linear component of stiffness in a nonlinear passive damper is provided by Vakakis in an experimental setup for studying seismic mitigation by TET (Vakakis et al., 2008). Here, a weak linear spring was used as a centering mechanism for a passive nonlinear damper and the essential nonlinearity term was modified to *nearly* essential nonlinearity to account for this implementation limitation.

If the linear stiffness component present in an NES implementation is high, the essential nonlinear characteristics are lost, thus producing a behavior more akin to a linear damper. Recall that nonlinear devices provide enhanced characteristics with respect to their linear counterparts. Specifically, they offer higher robustness against detuning and superior dynamic properties that do not limit them to resonate around a specific frequency, rather they resonate over a wider bandwidth, depending on the initial conditions and properties of the vibratory response of the base structure (Kerschen et al., 2006).

A recognized but not yet fully understood effect in TET is energy *backflow* (energy spreading back to the main system re-exciting it). This is an undesirable effect present in TET, and can be attributed to a small number of possible causes, namely, proper selection of structural parameters like stiffness and damping (Vakakis et al., 2004), overlooked dynamics such as misalignment in the fixtures, different sources of damping and uncertainties in the physical elements of the system, and the presence of a high linear term in the spring stiffness. This effect has not been reported as an undesirable behavior to the best of the author's knowledge. Though, several authors have proposed the principles of backflow as a beneficial physical phenomena for applications such as energy harvesting. A particular example is the work by Tang and Yang (Tang and Yang, 2012), where dynamic magnifiers are used to achieve an amplified motion of the harvester in comparison to the case where no amplifier is used. This requires a linear coupling term, consistent with the definition of backflow presented in this work.

TET has been under extensive analytical scrutiny over the past twenty years. Numerous studies have successfully explained the different mechanisms through which TET occurs, namely 1) fundamental transient resonance capture; 2) sub-harmonic transient resonance capture, also known as cascades of resonance capture, and; 3) nonlinear beats (Vakakis et al., 2008, 2004; Starosvetsky and Gendelman, 2010; Tripathi et al., 2017). Yet, the research to date has tended to focus on the analytical treatment of the dynamics of TET through frequency-domain energy-based methods such as the frequency-energy plot, the wavelet and Hilbert transforms and the frequency response function, and some time-domain representations of energy-based quantities, such as the instantaneous energy per unit mass.

In this dissertation, I explore a novel methodology to visualize and quantify the negative effects of energy backflow in a vibratory system, as a consequence of the presence of linear stiffness or any other dynamics. It will be shown that a practical way of looking at backflow is through the instantaneous power per unit mass of the primary oscillator. This quantity, depending on its sign, indicates energy either entering (spreading back) or leaving (being dissipated) the PO. Section 2.1 is devoted to presenting the problem statement and the mathematical formulations of the models used. Section 2.2 contains the energy and power measures used for evaluating the transfer and direction of energy between subsystems. Section 2.3 discusses the application of the proposed methodology through simulations of seismic excitations, and includes a brief experimental verification of the methodology.

1.4 Cantilevered beams with bounded lateral vibration

Nonlinear springs can be constructed from many types of physical systems that take advantage of geometric nonlinearities. Important applications of nonlinear springs that have received notable attention in recent years are NES, and energy harvesting systems. The former are basically nonlinear springs that can be attached to primary vibratory systems to create passive vibration dampers that can pump the energy out of the primary oscillator into the nonlinear spring. However, the latter is implemented for an inverse purpose, i.e., the energy generated in the spring is stored by conveying it to an accumulation system.

Several classes of physical realizations of NES devices based on nonlinear spring systems have been reported in literature over the past twenty years. In a recent review paper, Lu provides a comprehensive overview of the contributions in the field of NES (Lu et al., 2018). Amongst NES devices, a widely studied and physically implemented prototype is the wire NES, reported in literature by several scholars (Vakakis et al., 2008; Wierschem, 2014; Mcfarland et al., 2005). However, other classes of nonlinear springs based on different physical phenomena have also been extensively reported

(Wang et al., 2015b,a; Wierschem et al., 2017). A more recent development in nonlinear springs was proposed by Kluger, who developed a type of nonlinear spring based on the concept of a cantilever beam with specially shaped (indented) lateral boundaries for its utilization as energy harvester with robust performance under uncertainties in the excitations. She also arranged the device in a way such that it would work as a high resolution load cell (Kluger et al., 2015, 2014). Similarly, Rivlin used a related concept for applications in gap-closing electrostatic actuators and mechanical batteries (Rivlin and Elata, 2012; Rivlin, 2012; Shmulevich et al., 2013, 2015). Wang et al., proposed a similar application of a wideband piezoelectric energy harvester using a quadruple-well potential, induced by a combination of boundary contact and magnetoelasticity (Wang et al., 2018). Similarly, Liu compared the effect that different curvature fixtures have on energy harvesters based on cantilevered beams (Liu et al., 2018). An interesting application related with automotive vibration transducers was proposed by Spreeman where he imposed a hardening behavior to a spring by adding a boundary of predefined characteristic (Spreemann et al., 2011).

This concept of a cantilever beam bounded by specially shaped rigid surfaces is not new. In fact, the first scholar who proposed a similar idea was Huygens in 1659, later reported in his famous *Horologium Oscillatorium* in 1672 (Blackwell, 1986). In his design, Huygens used specially shaped boundaries around a pendulum to enhance the isochronism of the pendulum, where a strictly identical oscillation period regardless of the amplitude was guaranteed. More recently, Timoshenko included a particular mechanism consisting of a beam with cylindrical boundaries as an example of a nonlinear spring in his book *Strength of Materials* (Timoshenko, 1940), while Keer & Silva, provided an analytical solution for such a problem, and compared the solution obtained using theory of elasticity concepts, with that obtained from beam theory (Keer and Silva, 1970). A considerable amount of research on a somewhat similar problem regarding centrifugal pendulum vibration absorbers can be found in literature. After the first attempt in proposing a centrifugal pendulum vibration absorber, made in France in 1935, whose purpose was to control torsional vibrations in radial aircraft engine propellers Sharif-Bakhtiar and Shaw (1988), Shaw and collaborators, in a series of papers reported on the theoretical dynamics, bifurcations and chaotic motion of these types of systems, followed by their industrial use as torsional vibration absorbers for automotive engine crankshafts. The centrifugal pendulum vibration absorber is a combination of a tuned device with nonlinear characteristics, but with a featured tautochronicity in its design that allows it to remain tuned regardless of the disturbance torque (Shaw, 1985a,b; Shaw and Wiggins, 1988; Sharif-Bakhtiar and Shaw, 1988; Borowski et al., 1991; Haddow and Shaw, 2003). Several other researchers have also proposed nonlinear springs based on beams and pendulums, but based on different mechanics principles. Canturu et al., reported on shape-varying cantliever beams to obtain different spring characteristics depending on the chosen beam surface profile (Caruntu, 2009).

In this dissertation, a model and experimental verification of a model of a nonlinear spring that can capture the dynamics under large deformations are developed. The device studied herein is based on a cantilever beam with nonlinear characteristics provided by two rigid boundaries placed on both sides of the beam, thus limiting the free length of the beam as it gradually wraps around said boundaries. These boundaries have a carefully selected surface order in their surfaces. This constraint to the lateral vibration produces a variable nature on the modal characteristics of the system as the beam does not have a preferred vibration frequency and it is highly sensitive to initial conditions and the amplitude of excitation. A model is developed based on the force-displacement (F-D) characteristic, obtained from a static analysis, to generate an appropriate restoring spring force term to be included in the equation of motion of the device, which itself is derived from plane kinematics of rigid bodies, assuming that the system behaves like a pendulum rotating around a fixed axis. This model is then numerically simulated using sine dwell signals, to obtain frequency response functions. Moreover, the model is experimentally verified by fabricating a set of devices and further testing them using base excitation generated by a shake table. The results demonstrate that the proposed device has a broadband frequency of operation around a range of excitation time, which extends to higher frequencies. This suggests that the device could enter in TET regimes, suitable for applications of nonlinear energy transfer.

1.5 Scope, contribution and outline of this work

The purpose of this dissertation is to systematically develop a novel type of NES device with a geometric nonlinearity produced by specially shaped rigid boundaries located on both sides of a cantilever beam such that when it begins to vibrate, it starts to wrap around the rigid boundary on one side, until the end of the period of vibration, after which it starts wrapping around the boundary on the opposing side. This systematic approach includes conceptual design; mathematical modeling; characterization and simulation; physical design, including engineering requirements and specifications; fabrication; assembly; model updating; and experimental validation.

Specific contributions of this work include the application of a concept for vibration suppression of linear structures, the development of a fully integrable numerical model based on a polynomial stiffness that replicates the actual force-displacement characteristic of the proposed spring, the application of perturbation methods and Floquet theory to obtain the approximated/quasi-analytical solution of the system and its stability behavior, respectively, and the analysis of time, frequency and energy domain visualization tools to study the energetic activity of the interacting oscillators.

This dissertation is outlined as follows: The development of a novel methodology for analyzing the energy transfer mechanisms between primary oscillator and NES, through the use of the concept of mechanical power are covered in Chapter 2. The introduction of a novel type of nonlinear energy sink for vibration attenuation is introduced in Chapter 3, where the static characterization and development of a refined dynamic model of the device are presented, including the corresponding analytical treatment of the solution to the equations of motion, and a short experimental verification section at the end. Chapter 4 presents the numerical and experimental demonstration of the potential of the proposed NES as a vibration absorber with non-linear characteristics, by attaching it to a scaled linear laboratory structure. Finally, in Chapter 5, the conclusions and future directions of this research are discussed.

2. EVALUATION OF ENERGY AND POWER FLOW IN A NONLINEAR ENERGY SINK ATTACHED TO A LINEAR PRIMARY OSCILLATOR

This Chapter explores a methodology to visualize and quantify the negative effects of energy backflow in a vibratory system, as a consequence of the presence of linear stiffness or any other dynamics. Section 2.1 is devoted to presenting the problem statement and the mathematical formulations of the models used. Section 2.2 contains the energy and power measures used for evaluating the transfer and direction of energy between subsystems, and includes a discussion on the application of the proposed methodology through simulations of seismic excitations, and in Section 2.3 a brief experimental verification is presented.

2.1 Problem Formulation

Wire NESs are a type of nonlinear device used for vibration attenuation that take advantage of the elastic properties of materials for generating a geometric nonlinearity (Kerschen et al., 2007b; Mcfarland et al., 2005; Wierschem, 2014; Vakakis et al., 2008). Wire NESs functioning principle is sketched in Fig. 2.1(a). These devices consist of a thin piano wire with no pretension, clamped at two points on the host structure, A and B, which move as a consequence of the base excitation, generating motion at the coupling point between the NES and the host structure. This motion produces a NES base acceleration denoted by ($\ddot{x}_{\mathrm{b,N}}$). The wire is also clamped internally to a mass m that moves along a track CD fixed at the NES base, thus generating tension in the wire which in turn produces the nonlinear force. Both, the nonlinear restoring, and the resulting dissipation forces are associated with physical properties of the system, namely: the size and mechanical properties of the wire, the magnitude and shape of the NES mass, the travelling mechanism of the mass, and the configuration of the system setup (e.g.: initial tension on the wire, lubrication of moving parts, and so forth). These forces result in a total interaction force between the linear primary structure and the NES, and will be hereafter referred to as the *restoring force*. It shall be clarified that though this term is traditionally associated with springs, other authors have used it when referring to the combined restoring plus dissipation forces (Wierschem, 2014).

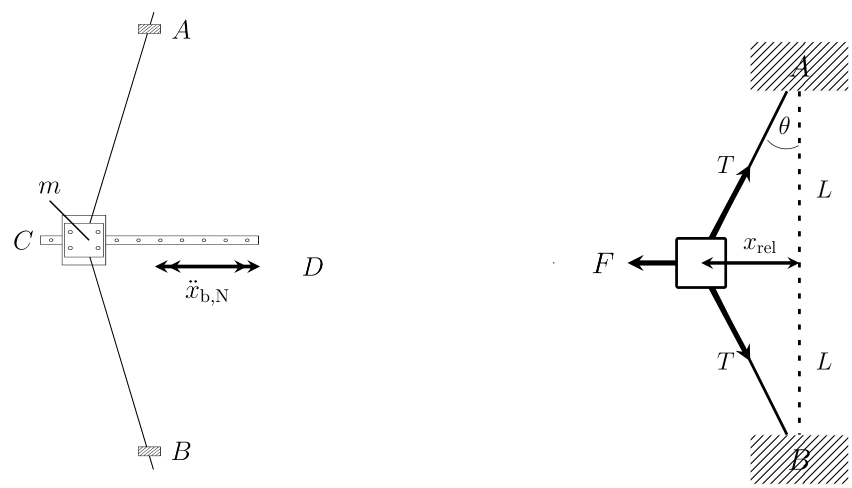

(a) (b)

Figure 2.1. : Wire NES diagram: a) schematic; b) free-body diagram.

2.1.1 NES resulting spring force

Consider the general schematic, and free-body diagrams, of the NES shown in Fig. 2.1. The NES consists of a mass (m) mounted over a bearing slider travelling back and forth in the direction of vibration indicated by the double arrow in Fig. 2.1(a). The mass is constrained by a wire fixed at points A and B which prevents it from escaping from the track. The complete NES assembly is mounted on top of an oscillating base ($\ddot{x}_{\mathrm{b,N}}$). As a consequence of the motion of the mass, a force (F) is generated, producing a tension T on the wire, which depends on its mechanical and material properties, and on the position of the mass with respect to the equilibrium point, given by the angle θ, and the relative position $x_{\mathrm{rel}} = x_{\mathrm{NES}} - x_{\mathrm{b,N}}$ (here, $x_{\mathrm{b,N}}$ is the displacement of the base where the NES is mounted, not to be confused with the base displacement of the whole structure). The distance between the anchor points is constant and equal to $2L$. The resulting force produced solely by the wire stiffness, which has been studied and derived in previous publications (Vakakis et al., 2008; Mcfarland et al., 2005) is:

$$f_{\mathrm{spring}} \approx k_{\mathrm{L}} x_{\mathrm{rel}} + \kappa_{\mathrm{NL}}\, x_{\mathrm{rel}}^3, \tag{2.1}$$

where k_{L} and κ_{NL} are the linear and nonlinear stiffness coefficients, respectively. As mentioned earlier, the linear component of the spring force, though small, is also included, as a linear stiffness is present in physical systems due to the initial tension necessary to avoid possible wire sagging (Wierschem, 2014). The other term, has been derived to be:

$$\kappa_{\mathrm{NL}} = \frac{EA}{L^3}. \tag{2.2}$$

Here, L and A are the length and cross-sectional area of the wire, and E is the modulus of elasticity of the wire material.

2.1.2 NES resulting dissipation force

There are also dissipation forces in the NES dynamics. The baseline design only accounts for a single viscous damping component added to the total resisting force, and most studies only include this component (Vakakis et al., 2008; Wierschem, 2014). However, to account for all of the dissipation mechanisms in more detail, three damping forces are considered in this study: i) dissipation through the viscous damping of the system; ii) dissipation through Coulomb friction at the interface between mass track and ball bearings; and iii) dissipation through drag between the mass and its surroundings. The complete dissipation expression is:

$$f_{\mathrm{diss}} = c_{\mathrm{L}}\, \dot{x}_{\mathrm{rel}} + \mu\, \mathrm{sign}(\dot{x}_{\mathrm{rel}}) + d_{\mathrm{d}}\, |\dot{x}_{\mathrm{rel}}| \dot{x}_{\mathrm{rel}}, \tag{2.3}$$

where $\dot{x}_{\mathrm{rel}}$ is the relative velocity of the mass with respect to the base where it is located, c_{L}, μ, and d_{d} are the viscous damping, friction coefficient and drag coefficient, respectively, and overdots indicate time-derivatives. In this work, the reduction of energy backflow is proposed by systematically increasing the viscous and drag coefficients. Therefore, with these considerations, the resulting restoring force can be defined as the sum of f_{spring} and f_{diss}, and can be written as:

$$f_{\mathrm{R}} = c_{\mathrm{L}}\,\dot{x}_{\mathrm{rel}} + \mu\,\mathrm{sign}(\dot{x}_{\mathrm{rel}}) + d_{\mathrm{d}}\,|\dot{x}_{\mathrm{rel}}|\dot{x}_{\mathrm{rel}} + k_{\mathrm{L}}x_{\mathrm{rel}} + \kappa_{\mathrm{NL}}\,x_{\mathrm{rel}}^3. \tag{2.4}$$

2.1.3 Primary oscillator

A physics-based model of a primary oscillating system and its interaction with the restoring force of the NES can be constructed to predict the system's behavior. In this study, a two-DOF mass-spring-damper system is considered as the primary oscillator (PO), with the NES attached to the second mass (see Fig. 2.2).

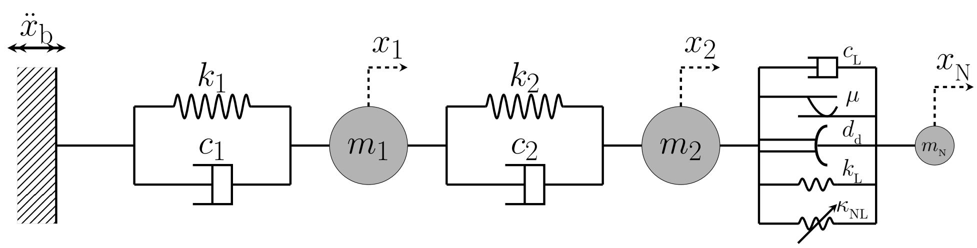

Figure 2.2. : Model of a two DOF-system with an NES on the second mass subjected to base excitation.

From Newton's second law of motion, the equations of motion (EOM) of the full system are:

$$\begin{aligned} m_1\ddot{x}_1 + c_1\dot{x}_1 + c_2(\dot{x}_1 - \dot{x}_2) + k_1x_1 + k_2(x_1 - x_2) &= -m_1\ddot{x}_{\mathrm{b}} \\ m_2\ddot{x}_2 + c_2(\dot{x}_2 - \dot{x}_1) + k_2(x_2 - x_1) + f_{\mathrm{R}}(x_2 - x_{\mathrm{N}}, \dot{x}_2 - \dot{x}_{\mathrm{N}}) &= -m_2\ddot{x}_{\mathrm{b}} \\ m_{\mathrm{N}}\ddot{x}_{\mathrm{N}} + f_{\mathrm{R}}(x_{\mathrm{N}} - x_2, \dot{x}_{\mathrm{N}} - \dot{x}_2) &= -m_{\mathrm{N}}\ddot{x}_{\mathrm{b}}, \end{aligned} \tag{2.5}$$

The quantity f_{R} is obtained from Eq. (2.4), m_i, c_i, and k_i are the mass, damping, and stiffness associated with each one of the masses ($i = 1, 2, \mathrm{N}$), and x_{b} is the base acceleration. In this expression, displacements and velocities are relative, and accelerations are absolute.This system can be treated as a discrete two-DOF state-space system with the NES force considered as a feedback force acting upon the 2nd mass. To express this system in state-space form, let us start by writing its EOM in matrix form:

$$\mathbf{M}\ddot{\mathbf{x}} + \mathbf{C}\dot{\mathbf{x}} + \mathbf{K}\mathbf{x} + \mathbf{f}_{\mathrm{R}} = -\mathbf{M}\,\boldsymbol{\iota}\,\ddot{x}_{\mathrm{b}}, \tag{2.6}$$

where

$$\mathbf{M} = \begin{bmatrix} m_1 & 0 \\ 0 & m_2 \end{bmatrix}, \quad \mathbf{C} = \begin{bmatrix} c_1 & -c_2 \\ -c_2 & c_1 + c_2 \end{bmatrix}, \mathbf{K} = \begin{bmatrix} k_1 & -k_2 \\ -k_2 & k_1 + k_2 \end{bmatrix},$$
$$\mathbf{f}_{\mathrm{R}} = \begin{Bmatrix} 0 \\ f_{\mathrm{R}}(x_{\mathrm{N}} - x_2, \dot{x}_{\mathrm{N}} - \dot{x}_2) \end{Bmatrix}, \quad \mathbf{x} = \begin{Bmatrix} x_1 \\ x_2 \end{Bmatrix}, \quad \boldsymbol{\iota} = \begin{Bmatrix} 1 \\ 1 \end{Bmatrix}.$$

In Eq. (2.6), overdots indicate time derivatives. This system may be expressed in state-space form, considering the interaction between the NES and the second mass as a feedback force in the input matrix. The state-space representation of a general system of differential equations has the form:

$$\begin{aligned} \dot{\mathbf{z}} &= \mathbf{A}\mathbf{z} + \mathbf{B}\mathbf{u} \\ \dot{\mathbf{y}} &= \mathbf{G}\mathbf{z} + \mathbf{H}\mathbf{u}, \end{aligned} \tag{2.7}$$

where $\mathbf{A}$, $\mathbf{B}$, $\mathbf{G}$, and $\mathbf{H}$ are the state, input, output and feedthrough matrices, respectively. $\mathbf{z}$, $\mathbf{y}$, and $\mathbf{u}$ are the state, output, and input vectors, respectively, which for the present case are $\mathbf{z} = [\mathbf{x} \quad \dot{\mathbf{x}}]^{\intercal}$, $\mathbf{y} = [\mathbf{x} \quad \dot{\mathbf{x}} \quad \ddot{\mathbf{x}}]^{\intercal}$, and $\mathbf{u} = [\ddot{x}_{\mathrm{b}} \quad 0 \quad f_{\mathrm{R}}]^{\intercal}$. The state-space matrices can be written as:

$$\begin{aligned} \mathbf{A} &= \begin{bmatrix} \mathbf{0}_{2\times2} & \mathbf{I}_{2\times2} \\ -\mathbf{M}^{-1}\mathbf{C} & -\mathbf{M}^{-1}\mathbf{K} \end{bmatrix}_{4\times4}, \quad \mathbf{B} = \begin{bmatrix} \mathbf{0}_{2\times1} & \mathbf{0}_{2\times2} \\ \boldsymbol{\iota}_{2\times1} & \mathbf{M}^{-1} \end{bmatrix}_{4\times3} \\ \mathbf{G} &= \begin{bmatrix} \mathbf{I} & \mathbf{0} \\ \mathbf{0} & \mathbf{I} \\ -\mathbf{M}^{-1}\mathbf{C} & -\mathbf{M}^{-1}\mathbf{K} \end{bmatrix}_{6\times4}, \quad \mathbf{H} = \begin{bmatrix} \mathbf{0}_{4\times1} & \mathbf{0}_{4\times2} \\ \mathbf{1}_{2\times1} & \mathbf{M}^{-1} \end{bmatrix}_{6\times3}. \end{aligned} \tag{2.8}$$

Velocity and displacement signals are obtained by integrating the acceleration of the second mass twice. The results of this integration are then multiplied by the appropriate damping and stiffness parameters to further obtain the restoring force f_{R}. In all of the simulations that follow, a Simulink model, built based upon these equations and the previously defined parameters is used.

2.1.4 Structural parameters and physical characteristics

To demonstrate the effectiveness of the proposed methodology, a physics-based model of a two-DOF base structure is produced as the underlying linear system. The structural parameters of the base structure are defined based upon identified values of a physical structure located in the Intelligent Infrastructure Systems Lab at Purdue University. The structure consists of two steel base plates connected by four steel spring columns, which give the system the behavior of a simple two-DOF spring system, similar to that shown in Fig. 2.2. The masses are defined to be $m_1 = 12.2\,\mathrm{kg}$, and $m_2 = 24.3\,\mathrm{kg}$. The spring stiffness coefficients are $k_1 = k_2 = 2.9 \times 10^4\,\mathrm{N/m}$. In addition, the structure has been identified to have modal damping ratios of $\zeta_1 = 0.62\,\%$ and $\zeta_2 = 0.53\,\%$ for the structure's first and second modes, respectively. The resulting natural frequencies of the structure are 3.67 Hz (23.06 rad/s), and 11.85 Hz (74.45 rad/s) for the first and second modes, and the mode shape vectors are $[0.49,\ 0.87]^{\intercal}$ and $[0.96,\ -0.27]^{\intercal}$, for the first and second mode.

The NES device is defined such that it has approximately 2% of the mass of the primary structure, with $m_{\mathrm{N}} = 0.7\,\mathrm{kg}$, a wire length of $L = 500\,\mathrm{mm}$, wire diameter $D = 0.5\,\mathrm{mm}$, and modulus of elasticity $E = 200\,\mathrm{GPa}$. Using these physical parameters, the damping coefficient and restoring force coefficients are estimated according to four cases defined in Table 2.1. Case 1 is considered as the baseline model, whose parameters were obtained from previous experimental identification results of similar systems (Wierschem, 2014), and using Eq. (2.2). The other three cases are proposed as possible candidates for minimizing energy backflow. It should be mentioned that friction is considered to be zero in the evaluation of the energy terms to be introduced in Section 3, for brevity, and also since the actual friction value is very small when compared to the magnitude of the other components of the restoring force. The models are simulated using a sampling frequency of $F_s = 1024$ Hz with an ODE4 Runge-Kutta fixed time-step solver.

Table 2.1. : Parameter identification results for the four case studies: a baseline NES system with unmodified damping characteristics (Case 1), and three NES systems with modified damping characteristics (Cases 2, 3 and 4).

Model	c_L (N s/m)	μ	d (N s^2/m^2)	k_L (N/m)	κ_{NL} (N/m^3)
Case 1	0.5	0	0	20	7.0×10^5
Case 2	2.5	0	0	20	7.0×10^5
Case 3	5	0	0	20	7.0×10^5
Case 4	0.5	0	3	20	7.0×10^5

2.1.5 Dynamics of TET in the two-DOF system with NES

It has been comprehensively demonstrated in Vakakis et al. (2008, 2004) and Starosvetsky and Gendelman (2009, 2010) that TET between a linear primary oscillator and an NES attached to it can take place when the right conditions of essentially nonlinear behavior in the NES and light damping in the PO, are met. When these conditions occur, there are three mechanisms for achieving TET in a system:

1. Fundamental transient resonance capture. Due to a 1:1 transient resonance capture of the dynamics, occurring when the system follows either the $S11{+}{+}{+}$ or the $S11{+}{-}{-}$ branches of the frequency-energy plot (FEP) shown in Fig. 2.3, at frequencies lower than the first fundamental frequency, or between the first and second fundamental frequencies (the letter S indicates a symmetric solution, and the symbols $+++$ or $+--$ indicate the phase of the three masses in the periodic orbit).

2. Fundamental sub-harmonic resonance capture. Similar to the previous case but occurring when the initial conditions of the system are not high enough to excite the fundamental resonance capture, but some sub-harmonic branch of the FEP, for example the branch labeled sub-harmonic in Fig. 2.3.

3. Nonlinear beating phenomena. The most desirable and powerful mechanism of transference of energy, occurring when the initial conditions cause the NES to engage in nonlinear beats with the PO, after which it gets trapped onto one of the fundamental energy transfer modes or sub-harmonic modes of the system. An example of this case will be apparent briefly.

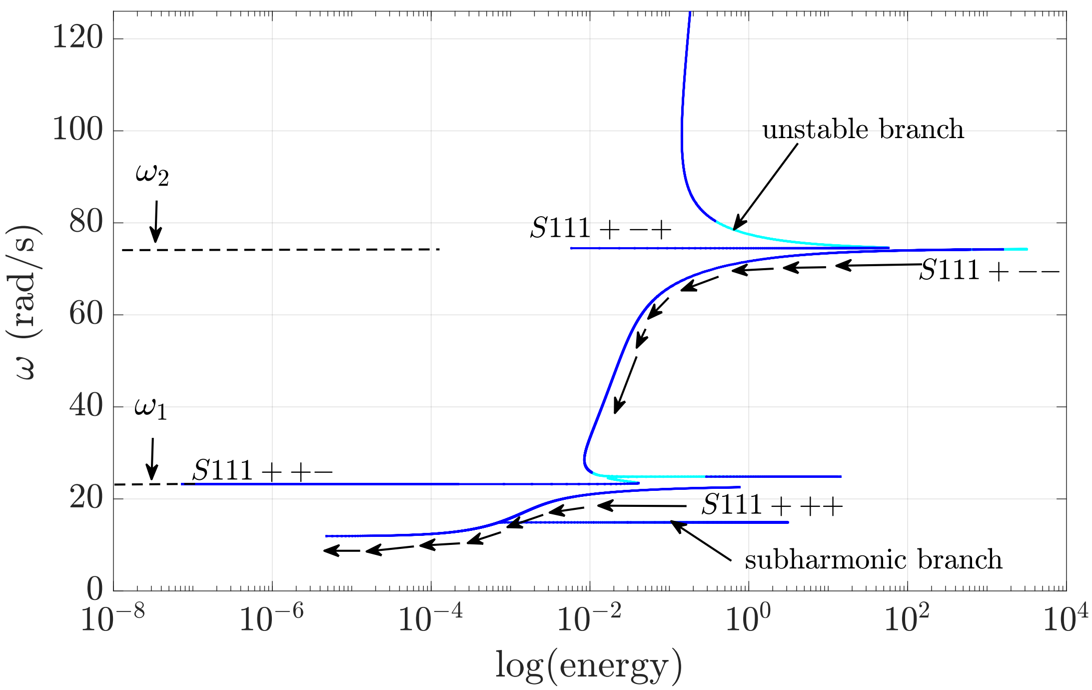

Figure 2.3. : Frequency-energy plot of periodic orbits of the system (Tao and Gibert, 2019).

Qualitatively, each one of these mechanisms will have different contributions to the energy backflow. However, to date, most measures of analysis focus on the energy transfer through the three aforementioned mechanisms without looking into how energy leaves/returns to the PO. An extensively used method of determining energy travel is through the wavelet transform superimposed to frequency-energy plots, where the energetic activity can be visualized with respect to the forcing frequency, and the trajectory of such energy can be followed and compared with the frequency-energy trajectory. In addition to this technique, the power per unit mass time history of the PO can be used to visualize this missing piece of information, such that further optimization or any other type of analysis can be realized upon the system with a much clearer vision of the energy flow.

2.2 Energy balance and power flow in targeted energy transfer

In this section it will be demonstrated that energy flow between the primary oscillator and the NES is not irreversible for all NES damping levels. Though an important amount of energy is indeed transferred to, and dissipated by, the NES, a portion of this energy inevitably returns, re-exciting the primary oscillator. The analysis begins by demonstrating the flow of energy in the system under simple impulse excitation, introduced in the form of initial velocity to the system's masses. This is equivalent to integrating the system using the initial conditions $x_1(0) = 0$; $x_2(0) = 0$; $x_{\mathrm{N}}(0) = 0$; $\dot{x}_1(0) = v_{1,0}$; $\dot{x}_1(0) = v_{2,0}$; and $\dot{x}_{\mathrm{N}}(0) = 0$.

The various energy terms can be defined by taking the integral of the Eq. (2.5) with respect to displacement (Chopra, 2012), as follows:

$$\int \ddot{\mathbf{x}}(t)^{\intercal}\mathbf{M}\mathbf{dx} + \int \dot{\mathbf{x}}(t)^{\intercal}\mathbf{C}\mathbf{dx} + \int \mathbf{x}(t)^{\intercal}\mathbf{K}\mathbf{dx} = -\int \ddot{x}_{\mathrm{b}}(t)\boldsymbol{\iota}^{\intercal}\mathbf{M}\mathbf{dx} - \int \mathbf{f}_{\mathrm{R}}^{\intercal}(t)\mathbf{dx}. \tag{2.9}$$

To simplify the integration procedure, the integrands of Eq. (2.9) are switched to time by means of the relationship $\mathbf{dx} = \dot{\mathbf{x}}dt$ (Zahrah and Hall, 1984; Uang and

Bertero, 1990), and the time-dependence of the responses is dropped for brevity, yielding:

$$\underbrace{\int_0^t \ddot{\mathbf{x}}^\intercal \mathbf{M}\dot{\mathbf{x}}\,dt}_{\textbf{kinetic}} + \underbrace{\int_0^t \dot{\mathbf{x}}^\intercal \mathbf{C}\dot{\mathbf{x}}\,dt}_{\textbf{dissipated}} + \underbrace{\int_0^t \dot{\mathbf{x}}^\intercal \mathbf{K}\mathbf{x}\,dt}_{\textbf{potential}} = \underbrace{-\int_0^t \dot{\mathbf{x}}^\intercal \mathbf{M}\,\iota\,\ddot{x}_\mathrm{b} dt}_{\textbf{input}} \underbrace{-\int_0^t \mathbf{f}_\mathrm{R}^\intercal \dot{\mathbf{x}} dt}_{\textbf{NES}}. \tag{2.10}$$

Dividing both sides by the total structural mass, a measure of the energy per unit mass of primary structure is obtained.

2.2.1 Metrics of evaluation

To further analyze the impact of different NES damping levels in the behavior of a primary oscillator, attenuated with an NES attached to the 2nd DOF, a series of simulations are carried out using computational tools developed in MATLAB and Simulink (The Mathworks Inc., 2018). For a clear interpretation of the results of these simulations, several performance measures are examined herein. A common measure used in similar problems (Vakakis et al., 2008; Kremer and Liu, 2014) is to calculate the total percentage of energy that is absorbed and dissipated by the NES ($\mathcal{E}_{\mathrm{NES},\,\%}$), which is the proportion of initial energy dissipated through the total damping of the NES throughout the duration of the time response. This quantity is defined as:

$$\mathcal{E}_{\mathrm{NES},\%} = \frac{c_\mathrm{L}\int_0^{t_\mathrm{end}} [\dot{x}_2(t) - \dot{x}_\mathrm{N}(t)]^2 dt + d\int_0^T [\dot{x}_2(t) - \dot{x}_\mathrm{N}(t)]^3 dt}{0.5\,[m_1\dot{x}_1^2(0) + m_2\dot{x}_2^2(0)]}, \tag{2.11}$$

where t_end is the total duration of the response. In this expression, the denominator is the initial energy stored in the primary oscillator. When the initial energy is continuous, the expression is slightly modified ($\mathcal{E}'_{\mathrm{NES},\,\%}$) to include the total input energy in the denominator, given by:

$$\mathcal{E}'_{\mathrm{NES},\%} = \frac{c_l\int_0^{t_\mathrm{end}} [\dot{x}_2(t) - \dot{x}_\mathrm{N}(t)]^2 dt + d\int_0^{t_\mathrm{end}} [\dot{x}_2(t) - \dot{x}_\mathrm{N}(t)]^3 dt}{\int_0^{t_\mathrm{end}} \dot{\mathbf{x}}(t)^\intercal \mathbf{M}\,\iota\,\ddot{x}_\mathrm{b}(t) dt}. \tag{2.12}$$

The second measure, used for calculating the level of effectiveness of the NES, is the percentage of instantaneous mechanical energy stored in the NES, which is defined as:

$$\mathcal{D}(t) = \frac{T_\mathrm{NES} + U_\mathrm{NES}}{T_\mathrm{PO} + U_\mathrm{PO} + T_\mathrm{NES} + U_\mathrm{NES}}, \tag{2.13}$$

where T is kinetic energy and U, potential energy. Subscripts $(\cdot)_{\mathrm{NES}}$ and $(\cdot)_{\mathrm{PO}}$ refer to the NES and primary oscillator, respectively. Here, the energy expressions of the primary oscillator are obtained from Eq. (2.10), and those of the NES are:

$$\begin{aligned} T_{\mathrm{NES}}(t) &= 0.5\, m_{\mathrm{N}} \dot{x}_{\mathrm{N}}^2 \\ U_{\mathrm{NES}}(t) &= 0.5\, k_l x_{\mathrm{N}}^2 + 0.25\, k_{nl} x_{\mathrm{N}}^4. \end{aligned} \tag{2.14}$$

The third measure is the total energy of the attenuated system (primary oscillator with NES unlocked), which is the sum of the kinetic plus potential energies of the primary oscillator. This quantity is useful for visually determining the amount of dissipation that the NES provides to the primary oscillator. Finally, the fourth measure to be studied is necessary for determining whether the energy is entering or leaving the primary oscillator. To this extent, the concept of power flow is used. From classical dynamics (Rowell, 2003), the power flow into a dynamic system is:

$$\mathcal{P}(t) = \frac{d\mathcal{E}(t)}{dt}, \tag{2.15}$$

where $\mathcal{P}(t)$ and $\mathcal{E}(t)$ are the instantaneous net power flow and stored energy, respectively. Here, power flow is defined as positive into the system, and negative out from the system. It follows that in a power flow time response, instances where the flow is negative indicate dissipation of energy, and instances where the flow is positive indicate backflow of energy into the system. The power flow variables to be calculated happen to be the integrands of Eq. (2.10), where the corresponding power variables of each forcing term are:

$$\begin{aligned} d\mathbf{W}_{\mathrm{pot}} &= \dot{\mathbf{x}}^{\intercal}(t)\mathbf{F}_{\mathrm{pot}}(t) \\ d\mathbf{W}_{\mathrm{kin}} &= \dot{\mathbf{x}}^{\intercal}(t)\mathbf{F}_{\mathrm{kin}}(t) \\ d\mathbf{W}_{\mathrm{diss}} &= \dot{\mathbf{x}}^{\intercal}(t)\mathbf{F}_{\mathrm{diss}}(t). \end{aligned} \tag{2.16}$$

2.2.2 System analysis with impulse excitation

The initial conditions are enforced proportionally to the first mode shape of the host structure, i.e.: the first mass is excited proportionally to the first entry of the mode shape, and similarly, the second mass is excited proportionally to the second entry of the mode shape, taking into account a normalized mode shape vector. Prior to conducting the simulations of the system, a sensitivity analysis of the performance of the NES under different initial conditions was carried out, as NESs are amplitude dependent systems. To this end, the percentage of initial energy dissipated in the NES ($\mathcal{E}_{\mathrm{NES},\%}$) is computed for a wide range of initial velocities, from 0 to 3 m/s, and each resulting point is then used to construct the plot shown in Fig. 2.4. This

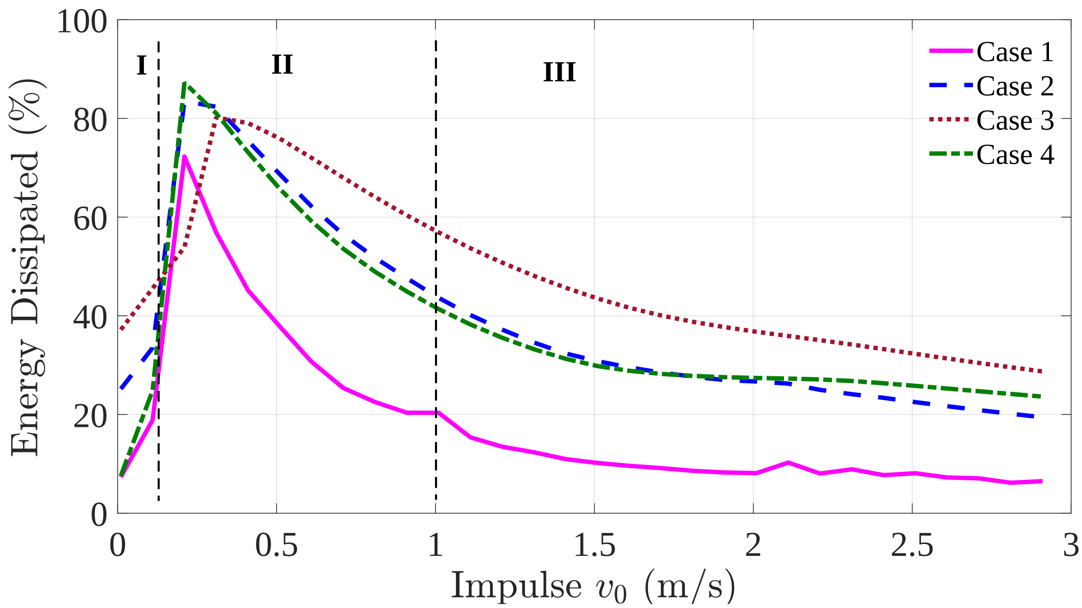

Figure 2.4. : Percentage of energy dissipated in the NES ($\mathcal{E}_{\mathrm{NES},\,\%}$) for different impulse excitation levels. Regions I, II and III correspond to low, medium and high energy levels, respectively.

plot is constructed to identify different regions of energetic activity of the primary oscillator-NES system for the four defined cases, and it shows that the NES is most effective at intermediate levels of impulsive input energy. The divisions between regions I, II and III were defined by identifying a critical point in the impulsive initial energy below which no significant energy dissipation takes place in the NES (around 0.15 m/s), and a similar point above which this same phenomenon occurs at high impulsive energy values (around 1 m/s) (Vakakis et al., 2008). Clearly, the NES is most effective at intermediate energy levels (region II). However, within this region, each case of damping in the NES may exhibit different sensitivity to a specific initial condition. This occurs, for example, when observing the percentage of NES energy of the system of Case 1, Case 2 and Case 4 (solid, dashed and dash-dotted lines in Fig. 2.4), all of which achieve a maximum performance at an initial velocity of $v_0 = 0.21\,\mathrm{m/s}$. In contrast, the system of Case 3 reaches its maximum performance at an initial velocity of $v_0 = 0.31\,\mathrm{m/s}$ (dotted line in Fig. 2.4). Depending on the damping scheme, it dissipates from 70 up to 90% of the total energy in this region. Conversely, at low energy levels (region I) all four cases of damping have no significant effect on the amount of energy extracted, which also occurs at high energy levels (region III). Therefore, the rest of this analysis will focus in the medium energy region from $v_0 = 0.15$ to $v_0 = 0.3\,\mathrm{m/s}$ because it constitutes the region where the NES is most effective and the understanding of its behavior is most valuable for the present analysis.

Four simulations are carried out, one for each damping level of the NES (Table 2.1), using the initial condition that produces the maximum extraction of energy from the primary oscillator (Fig. 2.4). The results corresponding to Case 1 are presented in Fig. 2.5. The dissipated energy within the NES in the form of nonlinear beats, reaches almost 90% of the total energy of the system at $t = 4\,\mathrm{s}$, while it remains high for most of the response duration. This is apparent when looking at the total instantaneous energy per unit mass, where a significant reduction of total energy with respect to the system with the NES locked (inactive) is observed. However, high levels of energy backflow are also observed in Fig. 2.5 (bottom plot). This suggests that while the NES performs well acting as a passive damper, an undesired flow of mechanical energy returns to the primary oscillator re-energizing its activity after some dissipation has already taken place.

If this result is compared to the classical approach of analysis where the damped dynamics of the system, represented by the continuous wavelet transform (CWT), are

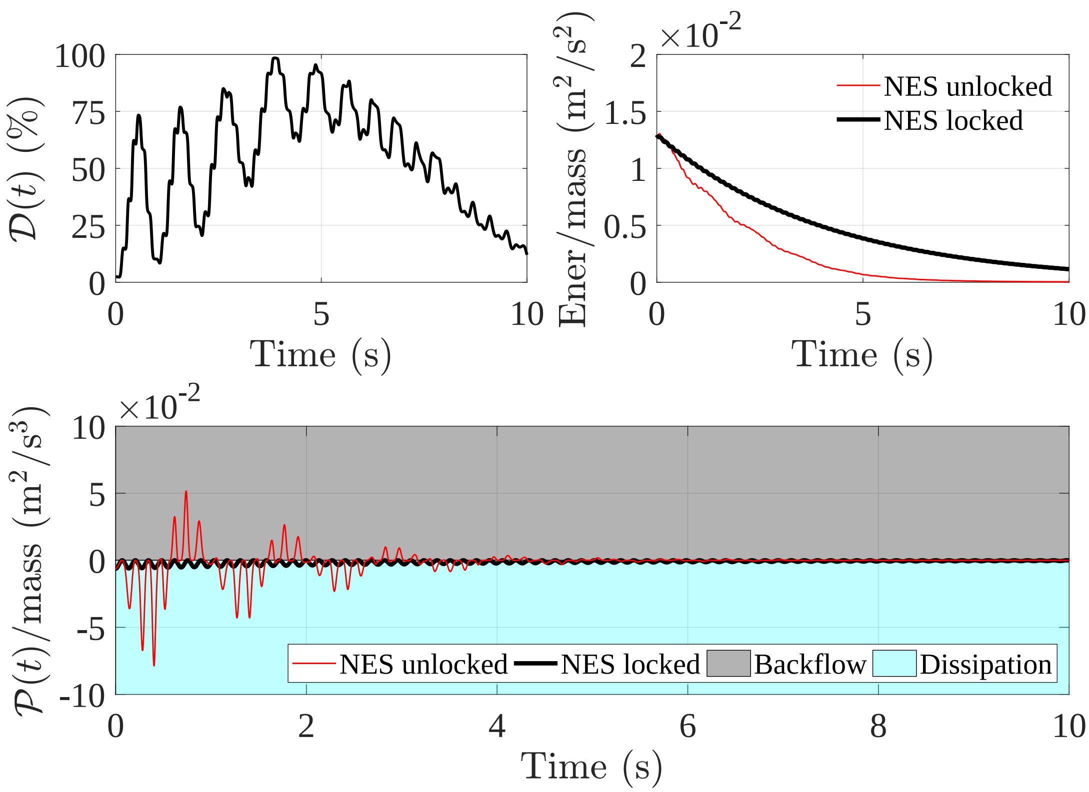

Figure 2.5. : Energy and power flow measures of an NES attached to a primary dynamic system. A simulation of Case 1 under impulsive excitation $v_0 = 0.21\,\mathrm{m/s}$. Top left: the percentage of instantaneous mechanical energy in the NES. Top right: a comparison of the total energy per mass unit of the linear primary system; bottom: the power flow per mass unit of the linear primary system.

superimposed on the frequency-energy representation of the nonlinear normal modes of the undamped system, as shown in Fig. 2.6, it is difficult to draw conclusions regarding energy backflow. It can be inferred from this plot though that energy transfer is taking place in the form of nonlinear beats to higher order modes, and that the system has engaged in fundamental transient resonance capture in the $S111+++$ branch, as well as some in the $S111+--$ branch. But we do not possess clear information on how energy backflow is affecting our primary oscillator in contrast to the clear time history of power shown in Fig. 2.15 (bottom).

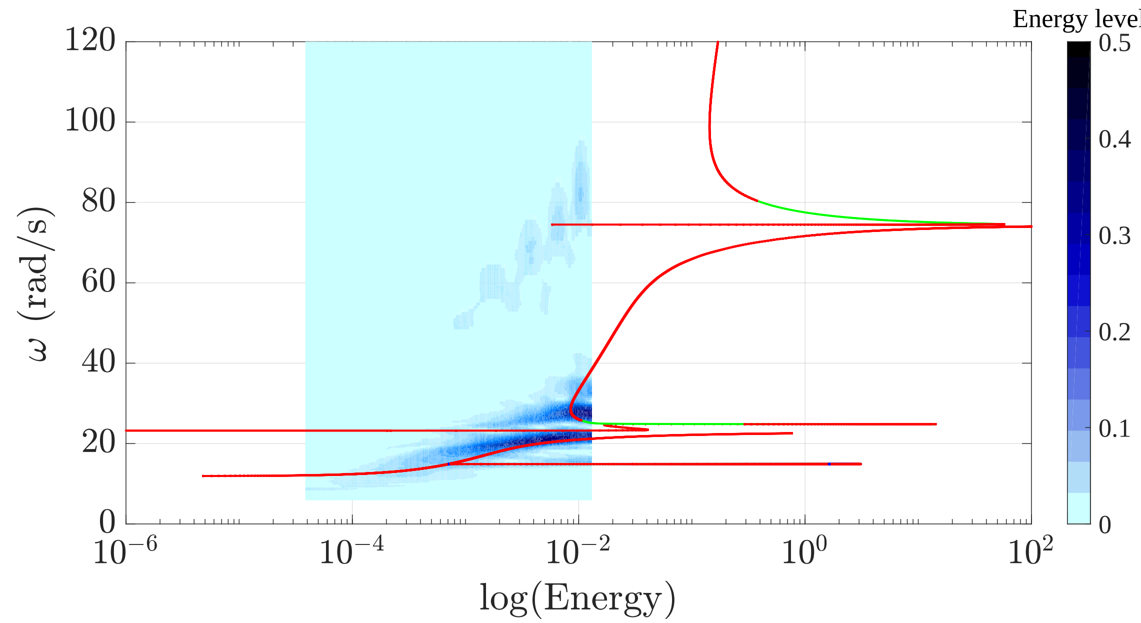

Figure 2.6. : Wavelet transform spectrum of the Case 1 NES energy, superimposed on the backbone of frequency-energy plot of the underlying Hamiltonian system.

Similarly, for Case 2 whose results are shown in Fig. 2.7, high dissipative activity is observed to appear quickly after the initial excitation (from $t = 0$ to $t = 2\,\mathrm{s}$). In this case, fundamental transient resonance capture is observed, causing the response to come to a near stop shortly after, as compared to $t \approx 6\,\mathrm{s}$ in the previous case. Here, it is clear that the changes in damping in the NES significantly reduce the amount of instantaneous energy present in the system (top right plot). Also, the power flow is observed to be in its majority below zero, meaning a dissipative flow instead of jumping from dissipation to backflow. This response is much more desirable in the system.

A similar contrast to the undamped versus damped dynamics of the system in the CWT superimposed on the backbone curves of the NES of Case 2 is shown in Fig. 2.8. The plot conclusively shows that the transfer mechanism is through a fundamental

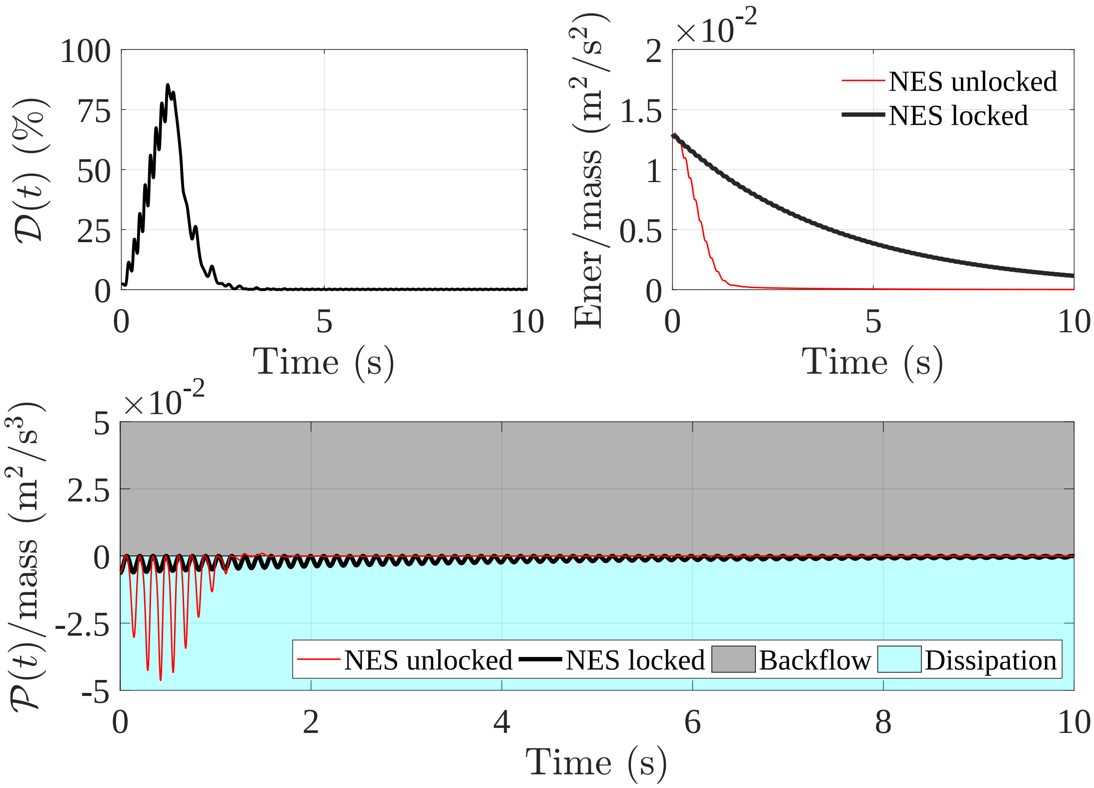

Figure 2.7. : Energy and power flow measures of an NES attached to a primary dynamic system. A simulation of Case 2 under impulsive excitation $v_0 = 0.21\,\mathrm{m/s}$. Top left: the percentage of instantaneous mechanical energy in the NES. Top right: a comparison of the total energy per mass unit of the linear primary system; bottom: the power flow per mass unit of the linear primary system.

transient along the $S111++-$ branch, with some energy also being transferred to the second mode. A solid conclusion about the direction of the energy cannot be drawn from this plot alone. The continuous nature of the energy traveling to the second mode suggests that the NES may be dissipating energy with low presence of backflow, in comparison to the discontinuous areas of Fig. 2.8. If this results are added to those on Fig. 2.7, one will have a much clearer picture of the energy transactions between PO and NES, which for this case implies that the latter is indeed extracting and dissipating the majority of the energy of the system without spreading it back to the system.

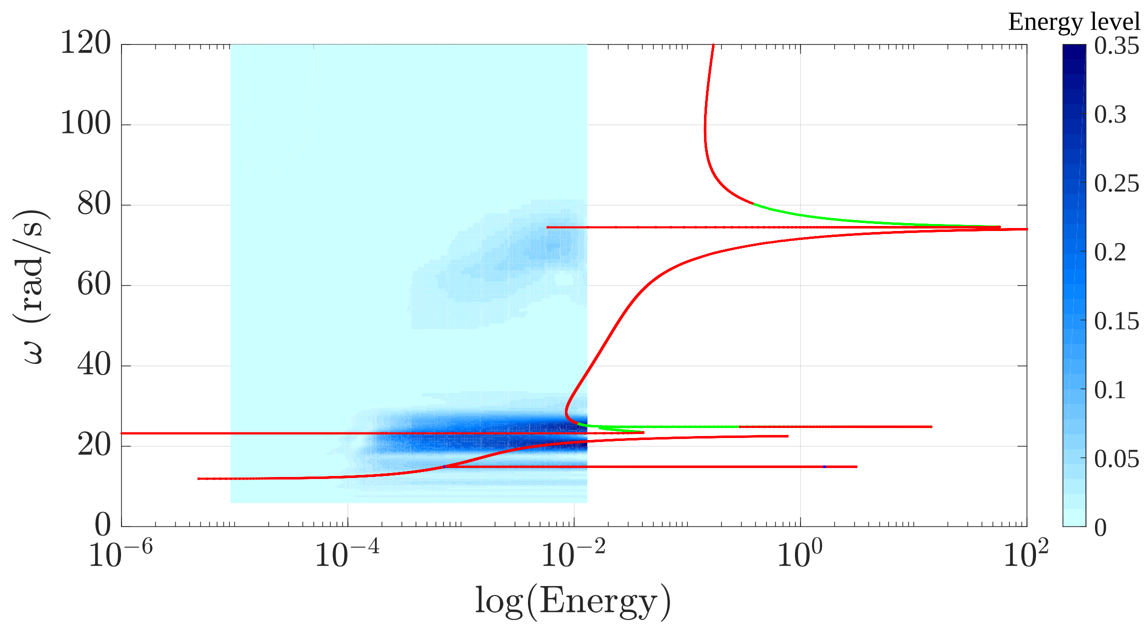

Figure 2.8. : Wavelet transform spectrum of the Case 2 NES energy, superimposed on the backbone of frequency-energy plot of the underlying Hamiltonian system.

The simulation results for Case 3 are presented in Fig. 2.9. Though a reduction in oscillations is observed also rather early, at approximately $t = 2\,\text{s}$, a lower percentage of energy dissipated in the NES is observed (top left plot). The power plot (bottom) shows fully dissipative behavior without any energy backflow. However, the low percentage of instantaneous energy observed suggests that the energy removed by this mechanism is less due to TET and more due to dissipation alone. This behavior also suggests a threshold in damping of the NES beyond which the NES is not as effective. In the CWT superimposed on the backbone curves of the NES of Case 3 shown in Fig. 2.10, it can be observed that the NES does not engage in much activity as in the previous two cases. Rather, most of the dissipation is due to sub-harmonic transient resonance capture below the first mode. However, by looking into the power plot of Fig. 2.9, this observation can be expanded to the fact that all of this energetic activity, though small, is of the dissipative form not returning to the base structure.

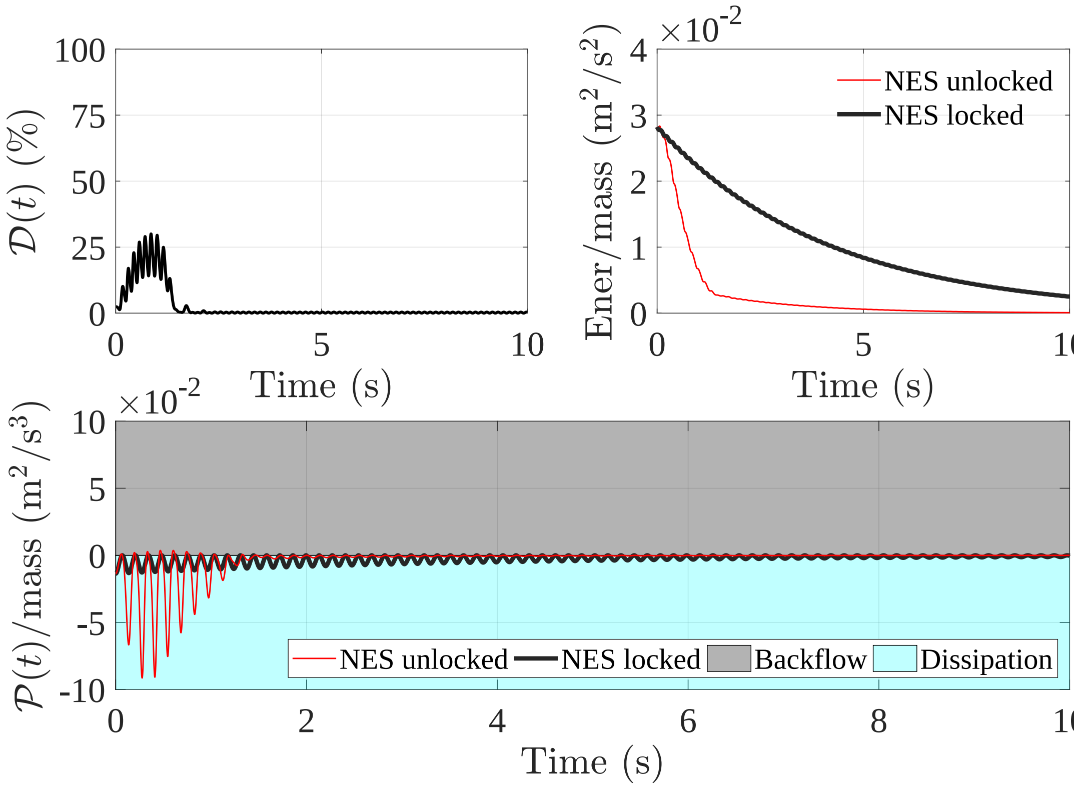

Figure 2.9. : Energy and power flow measures of an NES attached to a primary dynamic system. A simulation of Case 3 under impulsive excitation $v_0 = 0.31\,\mathrm{m/s}$. Top left: the percentage of instantaneous mechanical energy in the NES. Top right: a comparison of the total energy per mass unit of the linear primary system; bottom: the power flow per mass unit of the linear primary system.

The last simulation corresponds to Case 4 and its results are shown in Fig. 2.11. Interestingly, a high amount of TET is observed: 1) through fundamental transient resonance capture between $t = 0$ and $t = 2\,\mathrm{s}$; and 2) through nonlinear beats from $t = 2\,\mathrm{s}$ onward. This constitutes a case where a combination of TET and dissipation is achieved through a combination of damping mechanisms in the NES. The total

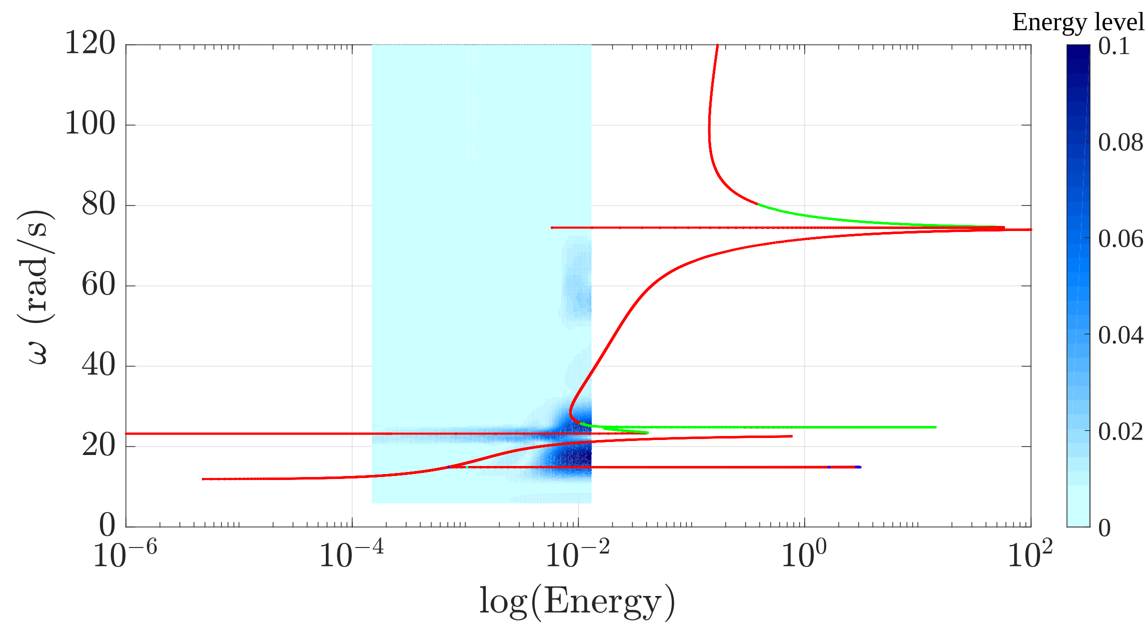

Figure 2.10. : Wavelet transform spectrum of the Case 3 NES energy, superimposed on the backbone of frequency-energy plot of the underlying Hamiltonian system.

energy per unit mass plot (top right) shows a fast decay in the response before $t = 2\,\mathrm{s}$, consistent with the high energy transfer by fundamental transient resonance capture mentioned previously. The total power per unit mass of the system shows that there is no significant return of energy to the primary oscillator, as the majority of impulsive energy is dissipated by the passive device. Similar to the previous three cases, the CWT of the energy is superimposed on the FEP, on Fig. 2.12. From this it can be concluded that a highly efficient transference of energy is taking place between the PO and Case 4 NES, in the form of fundamental transient resonance capture on both the $S111+++$, and $S111++-$ branches. Some nonlinear beating phenomena is also observed sending energy to the second mode, which appears in a continuous region. This suggests low backflow. Again, this result in combination with that of Fig. 2.18 provides a full picture of the energy on the primary system, NES and the interaction between these. An important observation from these sets of figures is that Case 1 and

Case 4 are comparable in energy transfer efficiency, but Case 4 offers a comparative advantage to Case 1 in the fact that it causes much less backflow into the system.

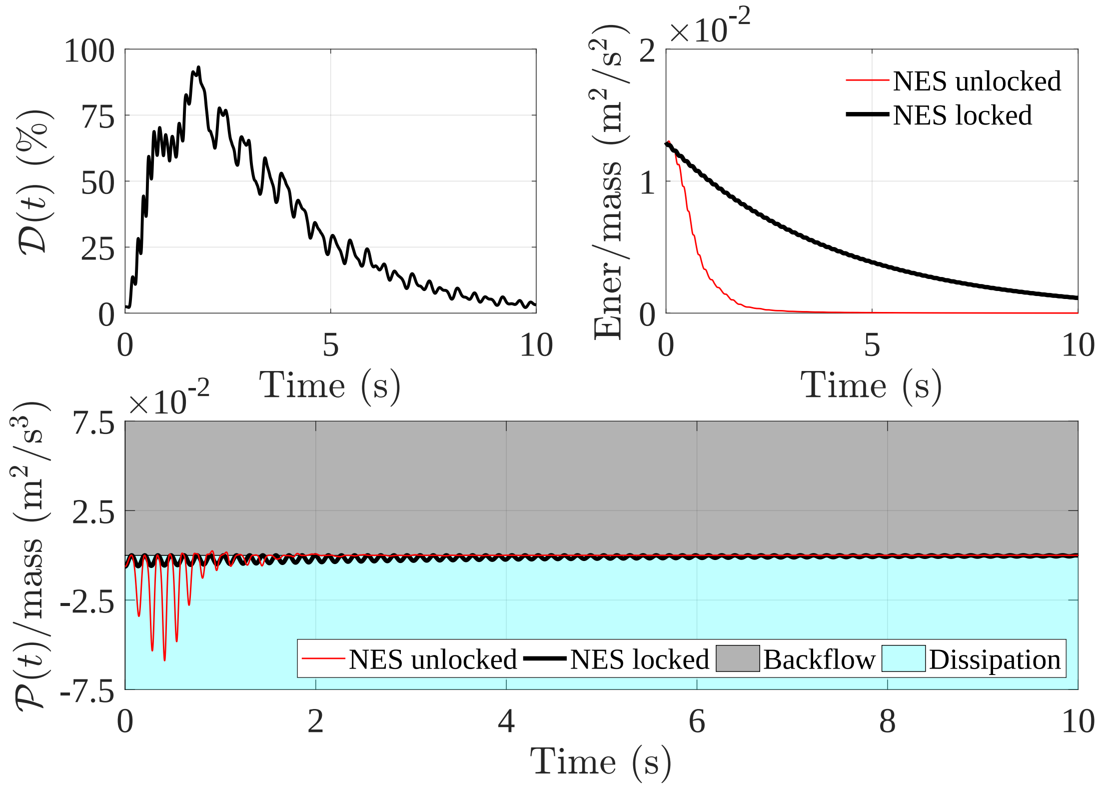

Figure 2.11. : Energy and power flow measures of an NES attached to a primary dynamic system. A simulation of Case 4 under impulsive excitation $v_0 = 0.21\,\mathrm{m/s}$. Top left: the percentage of instantaneous mechanical energy in the NES. Top right: a comparison of the total energy per mass unit of the linear primary system; bottom: the power flow per mass unit of the linear primary system.

2.2.3 System analysis with seismic excitation

A similar approach as that taken in the previous section is extended here for a seismic excitation. It has been demonstrated that NES are effective mechanisms for reducing excessive displacement responses of primary structures subjected to earth-

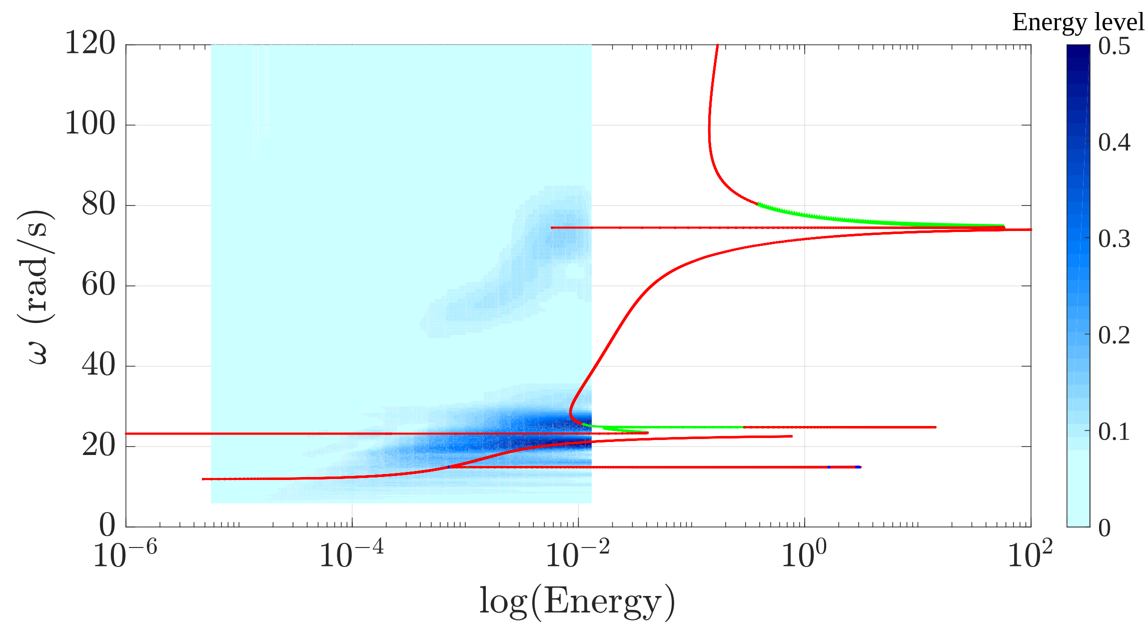

Figure 2.12. : Wavelet transform spectrum of Case 4 NES energy, superimposed on the backbone of frequency-energy plot of the underlying Hamiltonian system.

quake excitation (Desalvo, 2007; Nucera et al., 2010; Wierschem, 2014). Unprotected structures subjected to earthquake events are excited primarily around their first natural frequency due to the low frequency content of earthquakes. The addition of an NES to such systems modify their characteristics thus causing them to oscillate around more than just the first natural frequency, hence increasing their dissipation capability (Nucera et al., 2008).

The seismic record used in this study is the N-S component of the earthquake that occurred in Imperial Valley, CA on May 18, 1940, recorded with a strong motion seismograph in a station located in El Centro, CA, scaled in amplitude to produce a realistic response in the experimental specimen available in the lab, and also to account for the physical capability of the hydraulic actuator of the shake table that moves in the corresponding direction of excitation, whose maximum stroke is 63 mm. Therefore, a maximum base displacement of 15 mm is set as the scaling limitation of the historic record. The scaled acceleration record used for this part of the study, and its corresponding numerically-integrated displacement are shown in Fig. 2.13.

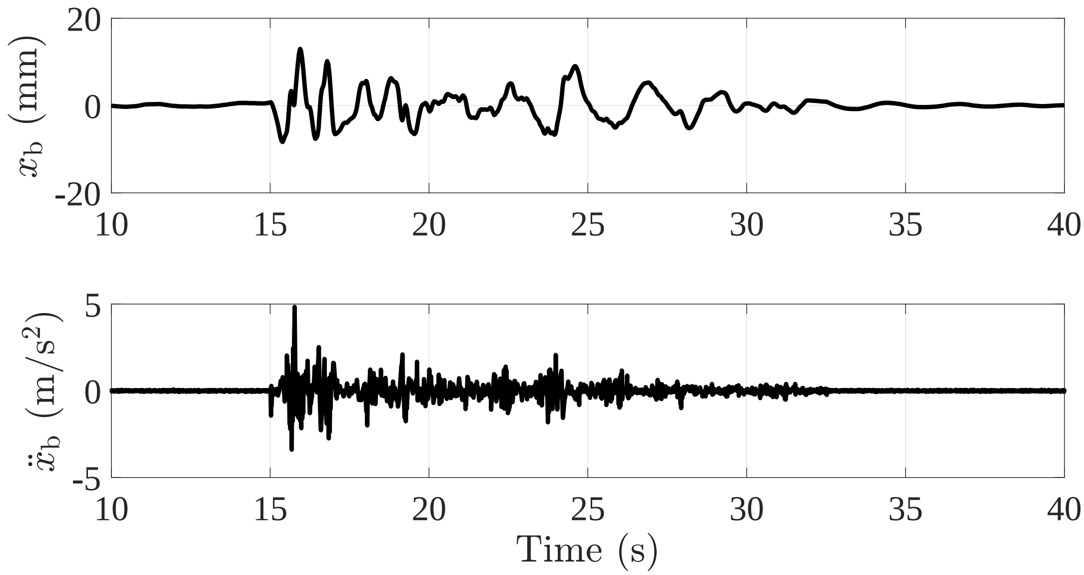

Figure 2.13. : Historic record of the El Centro earthquake, scaled in amplitude to provide a peak base displacement of 15 mm. Top: displacement record; bottom: acceleration record.

The advantages of using this type of excitation in contrast to impulse is twofold: 1) it provides more insights about events that are more likely to occur to a structure such as that used in this study; 2) it allows researchers to understand the behavior of a system when the input energy is not constant (e.g., the input energy to the structure in Case 1 of Table 2.1 is different to the input energy to the structure of Case 2, despite the initial excitation being the same). Moreover, time-dependent random base excitation such as earthquakes produce a continuous insertion of energy throughout the duration of the event. This is why the comparison of instantaneous energy is not as powerful as with the impulse excitation. Also, since earthquake excitation introduces a high degree of transients to the system, some of the performance measures used in the previous section may not reflect the actual behavior of the system under transients.

The aim of this section is to identify trends in the behavior of the combined system (primary plus NES). To this extent, three performance measures are analyzed in this case: 1) the percentage of instantaneous mechanical energy stored in the NES (Eq. (2.13)); 2) the instantaneous energy per unit mass, and; 3) the power per unit mass of the system. The proportion of initial energy absorbed and dissipated by the NES is used only to verify that the trends shown in Fig. 2.4 occur for the case of seismic excitation as well.

The sensitivity of the system to El Centro record with different amplitude scale factors to explore its nonlinear behavior is shown in Fig. 2.14. Here, the percentage of energy dissipated by the NES (similar to Eq. 2.11) is defined as:

$$\mathcal{E}'_{\mathrm{NES},\%} = \frac{c_l \int_0^{t_{\mathrm{end}}} [\dot{x}_2(t) - \dot{x}_{\mathrm{N}}(t)]^2 dt + d \int_0^{t_{\mathrm{end}}} [\dot{x}_2(t) - \dot{x}_{\mathrm{N}}(t)]^3 dt}{\int_0^{t_{\mathrm{end}}} \dot{\mathbf{x}}(t)^{\intercal} \mathbf{M}\, \boldsymbol{\iota}\, \ddot{x}_{\mathrm{b}}(t) dt}. \tag{2.17}$$

As mentioned earlier, for this phase of the study, this measure is used as a referential means for determining whether the level of seismic excitation plays a role in the behavior and performance of the NES at extracting energy from the primary system. It can be observed that similar to the impulse excitation, the NES is more effective at moderate energy levels (region II in the figure). This suggests, as in the case of impulse excitation that there exist lower and upper thresholds beyond which the NES does not get excited enough to a desired optimal energy extraction level (Fig. 2.14). It should be mentioned that divisions between regions I, II, and III follow a similar reasoning than in Fig. 2.4, that is to say, they were defined by identifying a critical point in the seismic energy level, expressed as a scaling factor of the seismic record, below which no significant energy dissipation takes place in the NES (around scale 0.2), and a similar point above which this same phenomenon occurs at high seismic energy level (around scale 1).

The results of Case 1 under seismic excitation are shown in Fig. 2.15. For this series of simulations, the initial conditions of all of the masses are zero both in velocity and displacement. The percentage of energy dissipated in the NES (top left plot) is as high as 90 % at some points of the response, mostly in the form of nonlinear beats,

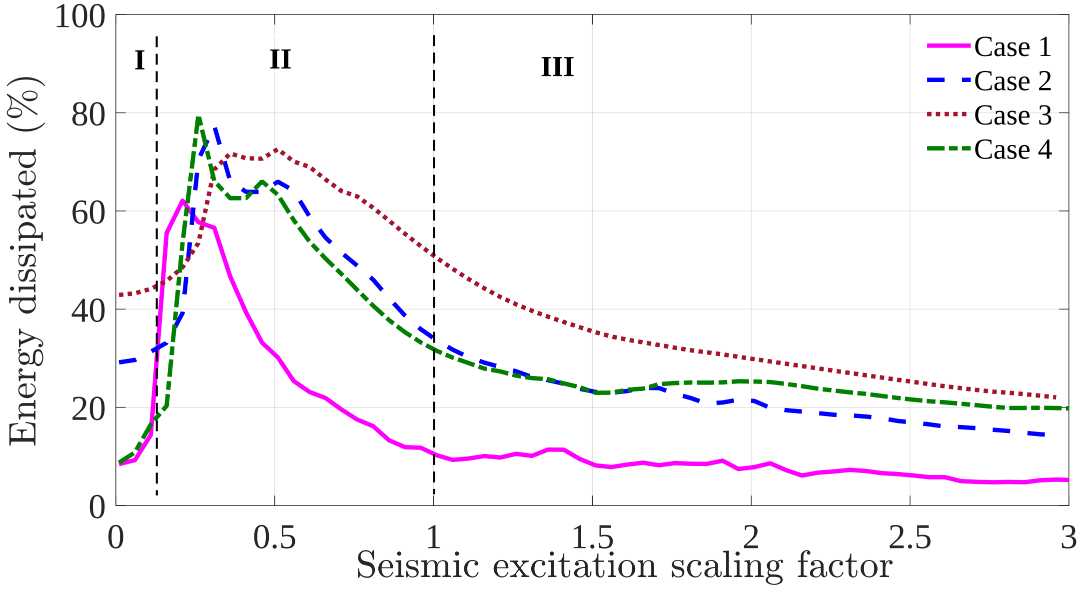

Figure 2.14. : Percentage of energy dissipated in the NES ($\mathcal{E}'_{\text{NES, \%}}$) for a system subjected to El Centro excitation, scaled to different amplitude levels.

becoming maximum after $t = 20\,\text{s}$. This is consistent with the total energy per unit mass of the linear system which after $t = 20\,\text{s}$ undergoes a significant reduction with respect to the linear system with the NES inactive (top right plot). The interchange of power flow between dissipation and backflow is evident, as in previous results where the nonlinear beating phenomena was present. Power jumps between the dissipation and backflow regions are observed sequentially (bottom plot), which suggests that though the percentage of input energy dissipated by the NES is high, the primary oscillator is subjected to vibration dissipation and backflow because it experiences energy transfer through beating phenomena.

Similarly, results corresponding to Case 2, are presented in Fig. 2.16. There is little evidence of nonlinear beating phenomena in this case, as the percentage of energy dissipated in the NES, though lower than in the previous case, occurs through resonance capture (top left plot). Here, the energy content of the system with the NES active is lower than that with the NES inactive almost in the entirety of the

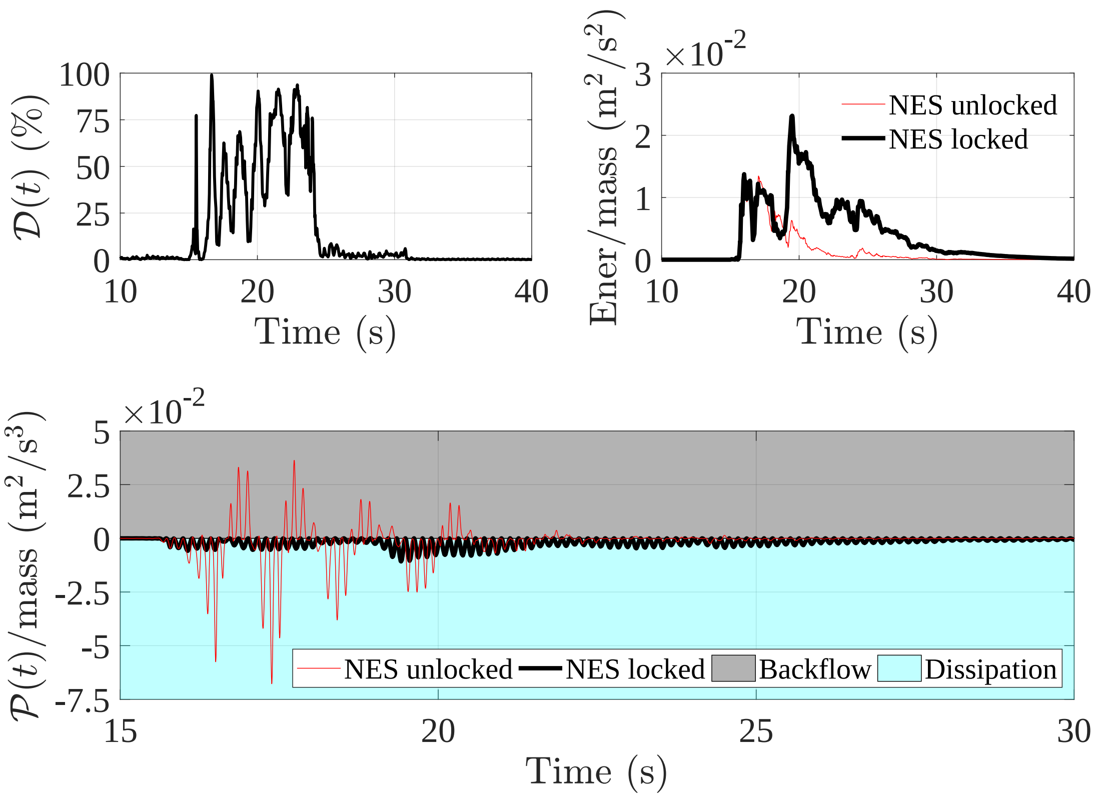

Figure 2.15. : Energy and power flow measures of a NES attached to a primary dynamic system. A simulation of Case 1 under seismic excitation (El Centro, 1940 – scaled to produce a peak base displacement of 15 mm. Top left: the percentage of instantaneous mechanical energy in the NES. Top right: a comparison of the total energy per mass unit of the linear primary system; bottom: the power flow per mass unit of the linear primary system.

response, except for a small instant at $t = 17$ s. The majority of backflow power has been eliminated (bottom plot), turning the system to a primarily dissipative one. It is interesting to mention here that a small addition in the damping of the NES produces a significant effect on the power flow of the system. In a simulation corresponding to Case 3, whose results are presented in Fig. 2.17, a lower percentage of dissipation is achieved in the NES (top left), but it is occurring in the form of fundamental

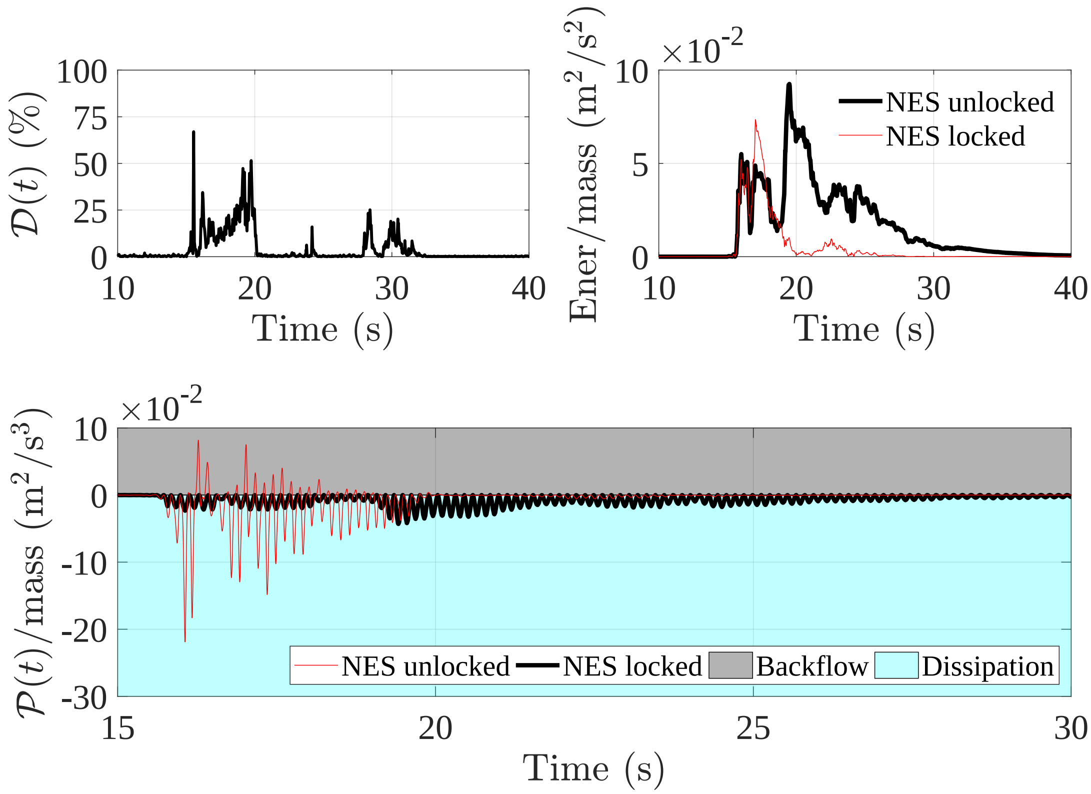

Figure 2.16. : Energy and power flow measures of an NES attached to a primary dynamic system. Simulation of Case 2 under El Centro, 1940 – scale factor = 1 excitation. Top left: the percentage of instantaneous mechanical energy in the NES. Top right: a comparison of the total energy per mass unit of the linear primary system; bottom: the power flow per mass unit of the linear primary system.

transient resonance capture. A slight reduction in the total energy per unit mass is observed (top right plot), particularly the peak at $t = 17\,$s. The most remarkable results are observed in the total power per unit mass (bottom plot), where almost the entire response occurs in the dissipation region, contrary to Case 2 where backflow was still present. Of course there are small occurrences of backflow in Case 3 as well, particularly at $t = 16.3$ and $t = 17\,$s, but for very short periods of time and low amplitudes.

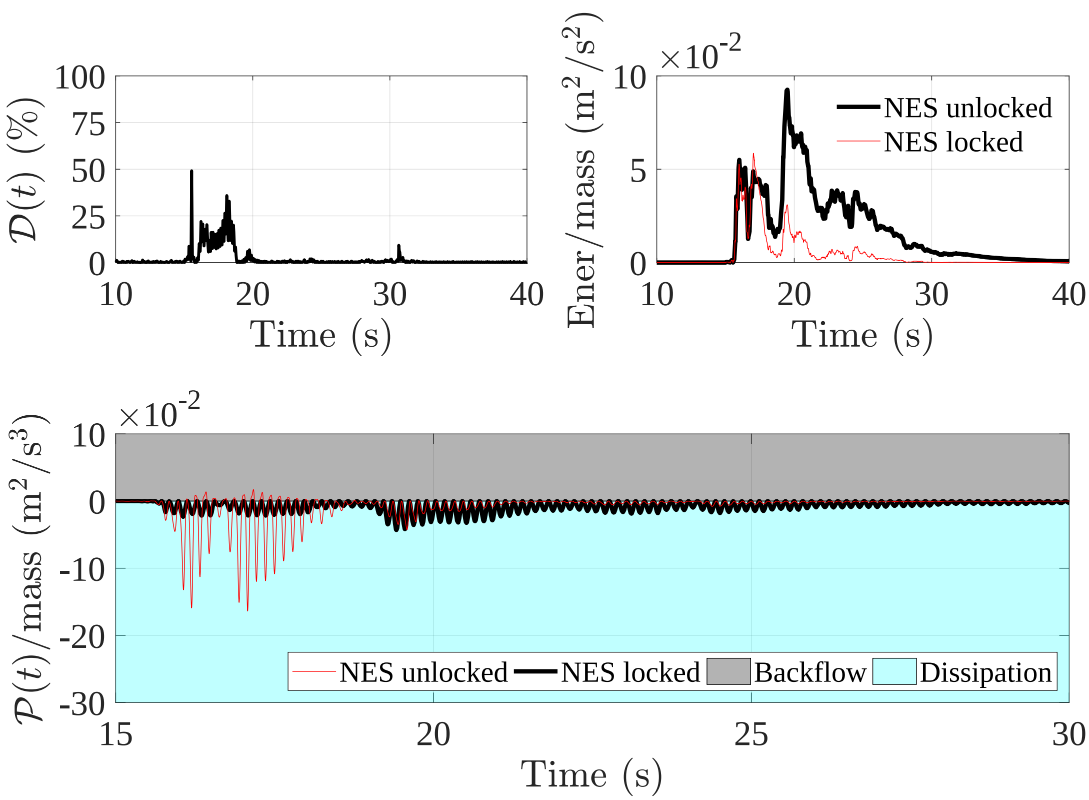

Figure 2.17. : Energy and power flow measures of an NES attached to a primary dynamic system. A simulation of Case 3 under El Centro, 1940 – scale factor = 1 excitation. Top left: the percentage of instantaneous mechanical energy in the NES. Top right: a comparison of the total energy per mass unit of the linear primary system; bottom: the power flow per mass unit of the linear primary system.

The final simulation results presented in this section correspond to quadratic damping (Case 4) whose results are presented in Fig. 2.18. The percentage of instantaneous mechanical energy in the NES depicted in the top left plot shows higher amplitudes than those of Case 3, throughout the duration of the simulation, mostly in the form of resonance capture which suggests that more dissipation of the response occurs in the NES as compared to Case 3. The reduction of energy in the system and the power flow are also very similar to those presented in Case 3. This again suggests that there is a threshold in the performance of the NES when its damping is increased.

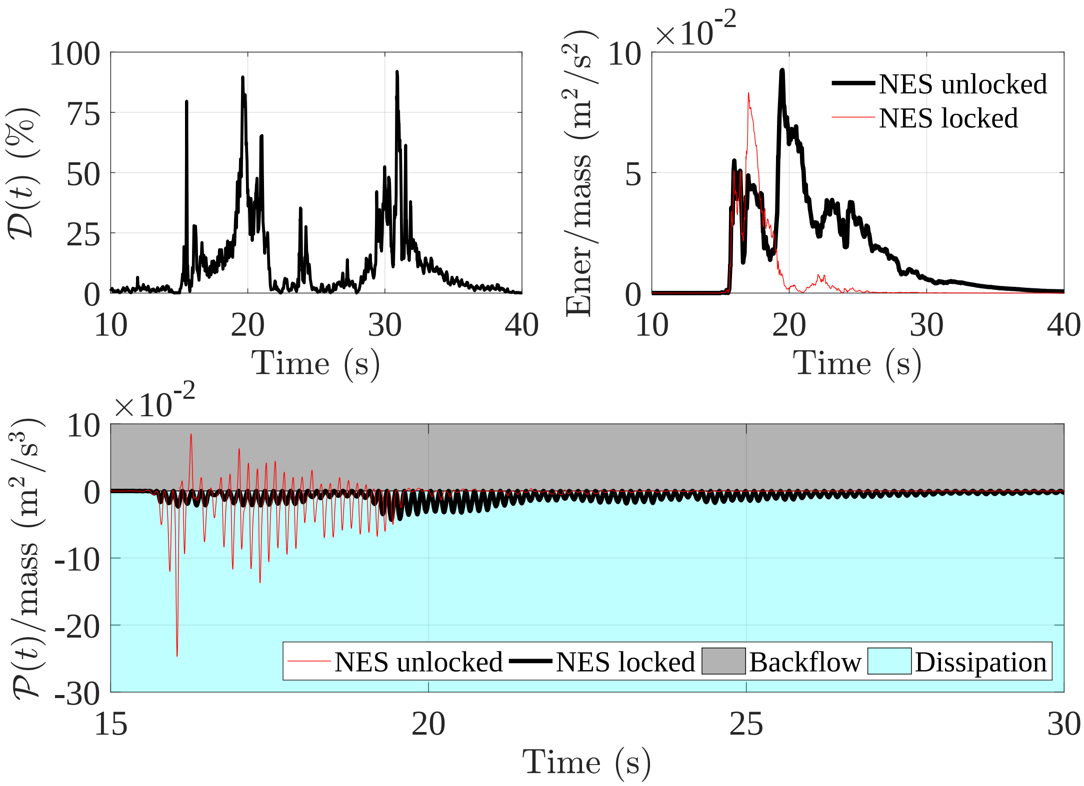

Figure 2.18. : Energy and power flow measures of an NES attached to a primary dynamic system. Simulation of Case 4 under El Centro, 1940 – scale factor = 1 excitation. Top left: the percentage of instantaneous mechanical energy in the NES. Top right: a comparison of the total energy per mass unit of the linear primary system; bottom: the power flow per mass unit of the linear primary system.

2.3 Experimental Validation

Experimental seismic testing of the system described in Section 2.1 is executed using a servo-hydraulic shake table. The equipment is a six-DOF servo-hydraulic shake table with table dimensions of 760×760 mm, a maximum payload of up to 200 kg, controlled by a built-in SC6000 PID-type controller for each DOF, manufactured by Shore Western Manufacturing. The excitation is executed in a single direction for these tests to avoid undesirable torsional effects.

A two-DOF primary oscillator with the NES mounted on the top floor as shown in Fig. 2.19(a) is used as the physical specimen. The dimensions of the structure and NES provided in Section 2.1 are based on this physical structure that exists in the lab.

The specially-fabricated NES used in this study consists of an aluminum mass, mounted over a steel carriage, part of a linear ball-bearing assembly travelling along a track in the same direction as the base excitation. The mass-wire interface has two cylindrical surfaces that minimize wear and tear of the wire when stretched, and the fixing of the wire to the base is through screw clamps. The wire used is a stainless steel piano string 0.62 mm of diameter.

Data acquisition is performed with an m+p International VibPilot8 DAQ box with built-in anti-aliasing filtering of the signal and up to 10 kHz sampling rate capability. This particular experiment uses a sampling rate of 1024 Hz. Four PCB-3711B1130G acceleration transducers, mounted on each DOF of the structure, the shake table surface, and the NES are used for recording the acceleration responses of the system.

The post-processing of the acquired signals is as follows: the signal is filtered through a low-pass filter with a cut-off frequency of 75 Hz to minimize the effects of high-frequency noise. To minimize the phase shift due to the filtering procedure, a two-way filtering procedure is applied using the MATLAB function *filtfilt.m*. Next, two steps of numerical integration are applied to the signals, to obtain velocity and displacement information. It should be noted that upon each integration step, a drift correction process is carried out by performing the following steps: 1) elimination of the initial bias in the signals by subtracting the mean of the noise; 2) elimination of any linear trend, generated during the first integration step, by subtracting an interpolated linear deviation from the integrated signal; 3) elimination of any quadratic trend, generated during the second integration step, by subtracting an interpolated quadratic deviation from the integrated signal. After these steps, a full set of acceleration, velocity and displacement responses are available for analysis.

The damping-optimized NES cases of Table 2.1 are physically realized by the following mechanisms: 1) the installation of two mechanical screw-variable air dashpots mounted on the top-floor of the structure, acting in the direction of motion of the NES carriage (Fig. 2.19(b)), and; 2) the design and installation of a *sail* to the NES configuration for the case of quadratic damping (Fig. 2.19(c)).

(a) (b) (c)

Figure 2.19. : Physical implementation of optimized damping cases: a) baseline NES; b) with high damping; c) with high drag.

For this experimental validation only three out of the four cases are compared in a similar fashion as the simulations: 1) a low damping case, comparable to Case 1 in Table 2.1; 2) a high damping case, comparable to Case 3 in Table 2.1, and; 3) a high drag case, comparable to Case 4 in Table 2.1.

The validation procedure starts by subjecting the original structure with the NES locked to the base excitation to obtain a reference response. Similarly, the next three NES cases are subjected to the same excitation to verify that the experimentally measured behaviors are similar to those observed in the simulations. The reference linear case is tested first and the same performance measures (Eqns. 2.13, 2.15, and 2.12) are calculated using the experimental responses.

The results of the first experiment, corresponding to a case of low damping similar to Case 1, are presented in Fig. 2.20. The percentage of energy dissipated in the NES (top left) shows a combination of resonance capture and beating phenomena. The peak value reaches around 80% at $t = 25\,\mathrm{s}$. The total energy per unit mass (top right) of the primary system shows a decrease after $t = 20\,\mathrm{s}$, but not much before this instant. Although, the power content per unit mass (bottom) does not show clearly divided regions of energy dissipation and backflow as in the simulation case, it does show a high presence of power flow in both directions. Zones of high dissipation can be identified by the amplitude of the peaks. Moreover, there are some regions where dissipation is clearly higher than backflow and vice versa. The results shown here are less clear than those obtained from the simulations, which may be due to the numerical integration procedure performed to the experimental data to obtain the velocity and displacement responses. These numerically-determined displacements and velocities are used to construct this plot. As mentioned earlier, only acceleration sensors are used in this experiment, Velocity and displacement information is obtained from integration. Despite the use of filtering, trend elimination, and end effects minimization in the integrated signals, there are always undesirable transients that hinder this process, here preventing us from obtain cleaner results.

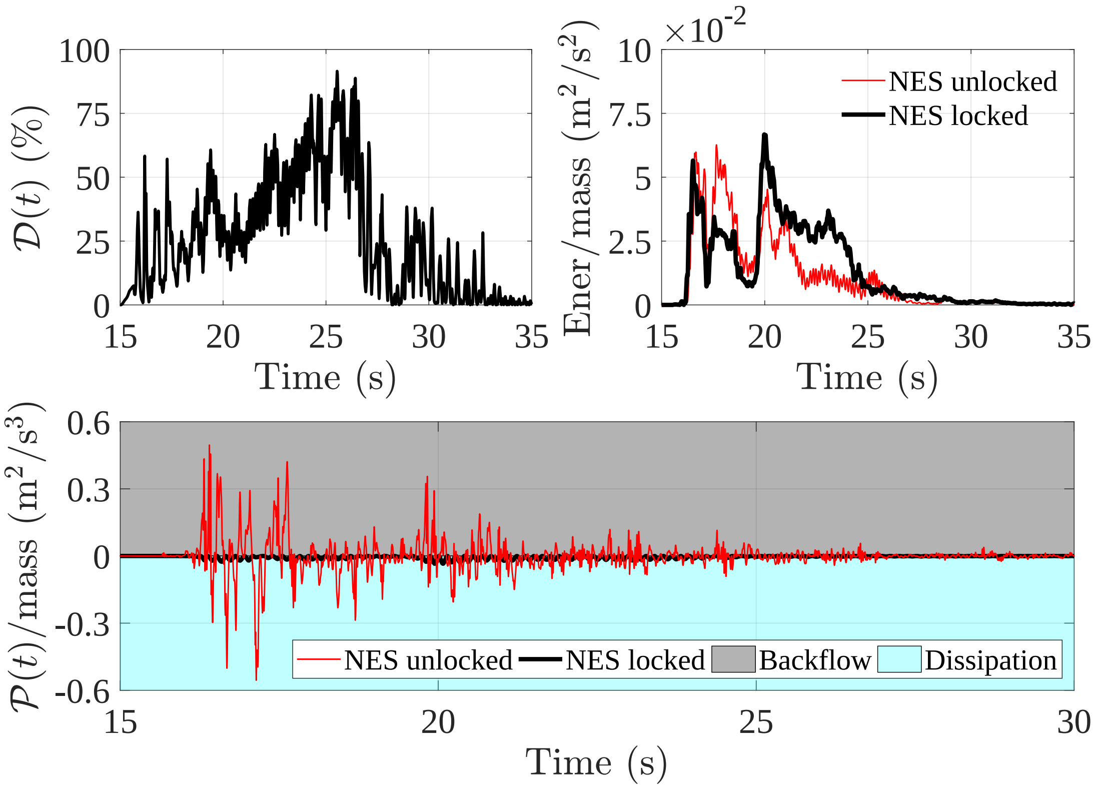

Figure 2.20. : Experimental performance of an NES on energy extraction from a PO. Seismic excitation: El Centro, 1940 – scaled to achieve a peak base displacement of 15 mm. Low damping (similar to Case 1). Top left: the percentage of energy dissipated in the NES. Top right: the total energy per unit mass. Bottom: the total power per unit mass.

Let us now examine the second case, in which an NES with high damping is used, similar to Case 3 in Table 2.1. The results are presented in Fig. 2.21. Here the percentage of energy dissipated in the NES does not reach high levels, though minimal presence of nonlinear beats is observed. High frequency transient behavior is also observed in this plot (top left). The total energy per unit mass plot shows no significant difference with the previous case, probably due to the system reaching a threshold in damping where further increases in damping do not cause significant changes in the energy activity. Similarly, the power plot shows no significant differences with the previous case, but it still demonstrates more dissipation than backflow.

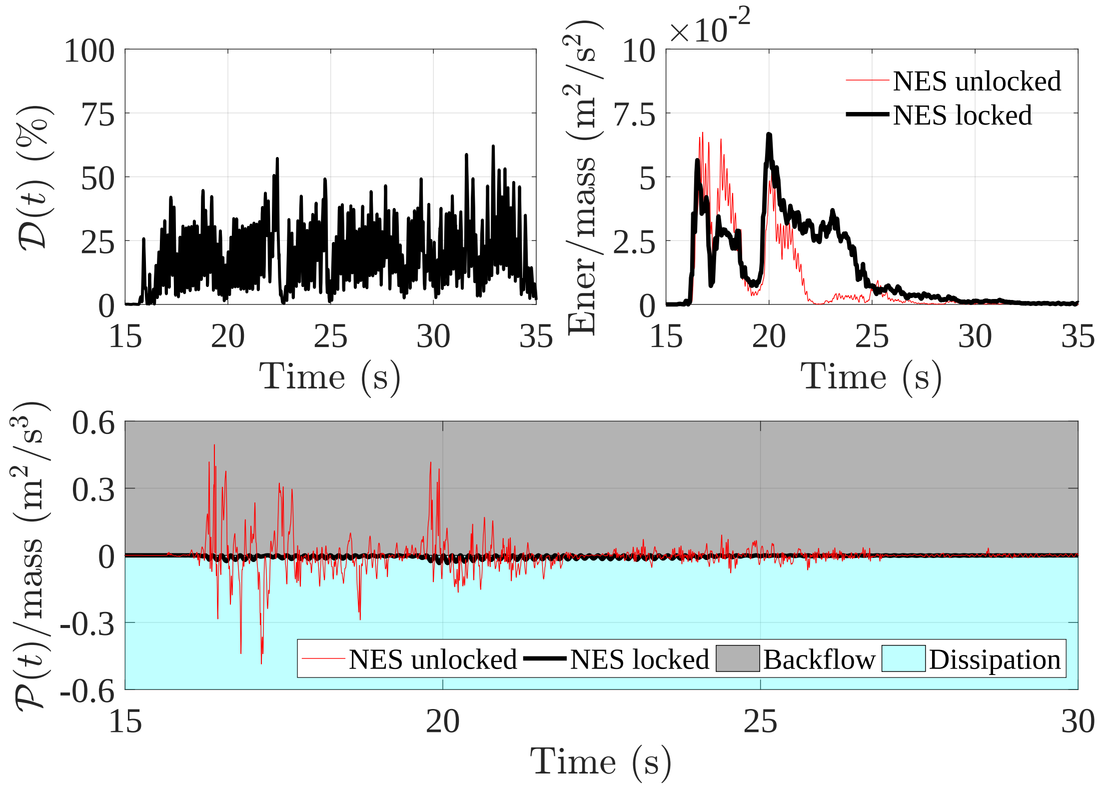

Figure 2.21. : Experimental performance of an NES on energy extraction from a PO. Seismic excitation: El Centro, 1940 – scaled to achieve a peak displacement of the 2nd mass of 15 mm. High damping (similar to Case 3).

Finally, for the third experiment we examine a case where extra damping in the form of a quadratic term is present due to the attachment of a sail in the NES setup (Fig.2.19(c)). This experiment is similar to Case 4 and its results are presented in Fig. 2.22. Here, a high percentage of energy is dissipated in the NES from $t = 19$ to $t = 275\,$s, reaching values up to 80 %, corroborated by the total energy per unit mass plot (top right) where a reduction in the energy is observed for the same time period. Conclusive statements from the power per unit mass plot cannot be drawn however.

Nonetheless lower backflow is observed than in previous cases through a comparison of peaks at similar time instances with dissipation behavior staying constant. This behavior suggests a superior performance of the device with less energy backflow.

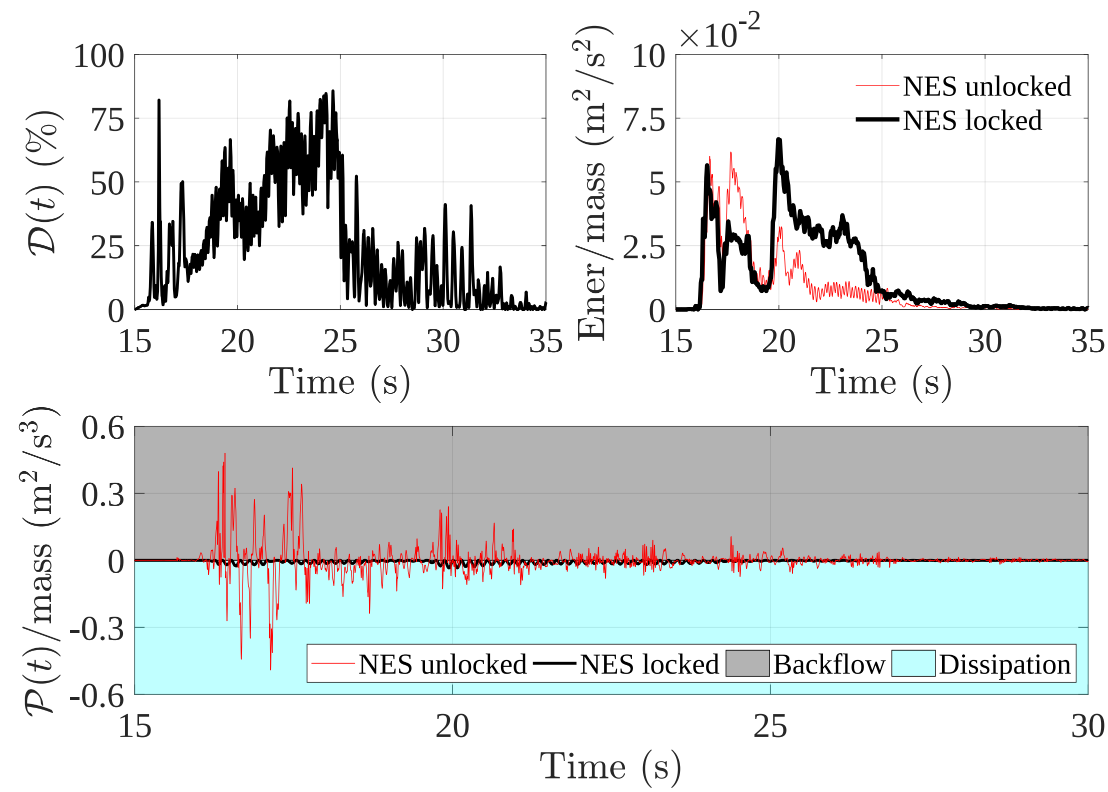

Figure 2.22. : Experimental performance of an NES on energy extraction from a PO. Seismic excitation: El Centro, 1940 – scaled to achieve a peak displacement of the 2nd mass of 15 mm. high drag (similar to Case 4).

The presented experimental results are qualitatively similar to those obtained in the numerical study in Section 2.2. The main purpose of presenting this comparison is to stress the importance, and usefulness, of the technique presented here, *i.e,* the use of power to evaluate direction and state of dissipation of energy of the system. To ensure that the experimental results are indeed qualitatively similar to the numerical ones, an additional verification step was taken by looking into the power spectral density of the three quantities that have been compared in this section: 1) the energy dissipated in the NES, 2) the total energy per unit mass, and 3) the total power per unit mass. All three of the plots show similar dominant peaks for both the numerical and the experimental results, with a slight increase in the power magnitude for the entire bandwidth of interest. As mentioned earlier, the differences in the power plots corresponding to the numerical and experimental cases can be attributed to several sources of error, some of which are:

- System identification estimation errors, process in which some parameters are extracted from the experimental setup. In this case, least squares estimation was used, which introduces certain levels of errors in the identified values.
- Double integration with their subsequent filtering and detrending processes.
- Introduction of measurement noise from sensors and digital-to-analog (D/A), and analog-to-digital (A/D) systems, which introduce computational errors.
- Small mechanical discrepancies in the setup (e.g., small gaps between mass and dashpots, bumping of the mass towards the end of the motion).

2.4 Summary

This study has been conducted with the intent to provide the community with additional tools for evaluating and assessing the energy dynamics in a nonlinear passive damper system for structural vibration, particularly under seismic excitations. This methodology is intended to complement the already available and widely used tools in this regard, such as the instantaneous percentage of mechanical energy dissipated in the NES, and the comparison of mechanical energy in the host structure before and after the NES is active.

Past numerical results and experimental observations demonstrate the occurrence of energy backflow between a nonlinear energy sink and the primary system to which it is attached. The causes for this phenomenon are not yet fully understood. However, the presence of linear components of stiffness in experimental and applied scenarios are thought to be responsible for a good portion of it. The introduction of the quantity power per unit mass of the primary oscillator is presented as a practical and straightforward methodology for evaluating the direction of the energy in targeted energy transfer systems, with quantity being in the negative region when the structure acts in pure dissipation (energy leaving), and in the positive region when the structure acts in pure oscillation (energy returning). This methodology aims to build upon existing techniques for the energy evaluation of nonlinear energy sinks and the energy activity between these and the primary structures to which they are attached. Results obtained from simulations and experiments demonstrate that it may be a powerful method in addition to the already available energy measures of percentage of instantaneous energy dissipated in the NES and energy per unit mass of the primary system. The developed models also constitute powerful tools for analyzing different types of responses of a two-DOF primary system with an NES mounted on the second mass. A controlled increment in the damping of the dissipation device is used as a means to lower the effects of energy backflow. To achieve this, two mechanical alternatives are explored: 1) the increment of viscous damping in the NES (experimentally through variable force air dashpots), and, 2) the addition of a very simple steady-state aerodynamic quadratic damping term from a drag source (experimentally achieved through the attachment of a "sail" to the NES). A series of computational simulations of defined damping cases are performed, and the responses of the NES-retrofitted systems show a significant decrease of oscillating response (energy interchange between primary system and NES). Some undesirable effects may appear in the experimental measurements of the simulated systems due to several possible sources of error, particularly because of the presence of measurement noise amplification, and integration errors. Further investigation extending this methodology may include state-estimation techniques, such as the use of nonlinear state estimators to obtain a better set of state responses.

3. DYNAMICS OF A NONLINEAR SPRING BASED ON A CANTILEVERED BEAM WITH SPECIALLY SHAPED RIGID BOUNDARIES

The objective of this chapter is to develop and experimentally verify a dynamic model of a novel nonlinear spring that can predict its behavior when coupled to a host structure. The device studied herein is based on a cantilever beam with nonlinear characteristics provided by two rigid boundaries placed on both sides of the beam, thus limiting the free length of the beam as it gradually wraps around said boundaries. These boundaries have a carefully selected surface order in their surfaces. This constraint to the lateral vibration produces a variable nature in the modal characteristics of the system as the beam does not have a preferred vibration frequency and it is highly sensitive to initial conditions and amplitude of excitation. First, a model is developed based on the force-displacement (F-D) characteristic, obtained from the static analysis, to generate an appropriate restoring spring force term to be included in the equation of motion of the device, which is then derived from the plane kinematics of rigid bodies, assuming that the system behaves like a pendulum rotating around a fixed axis. This model is then numerically simulated using sine dwell signals, (i.e.: stationary frequency sweeps, allowing the system to reach steady state at each excitation frequency, before increasing the frequency to the next value) thus obtaining frequency response functions. Moreover, the model is experimentally verified by fabricating a set of devices and further testing them using base excitation generated by a shake table.

3.1 Semi-analytical model

The equations of motion (EOMs) of the nonlinear spring for dynamic analysis are derived in this section, first by studying the static behavior of the spring with respect to the imparted force, and with this information, a mathematical expression of the response of the system is obtained.

3.1.1 Static analysis

To develop a dynamic model for the proposed spring, a force-displacement relationship is required as first step, and then based on the static analysis, two different dynamic models of the device are derived for comparison and verification purposes.

Consider a cantilever beam supported by a smooth rigid curved boundary of height H_{S}, and length L_{S}, and with a prescribed shape, described by a function $f(l-x)$, as shown in Fig. 3.1. The quantity l is the total length of the beam, x is the length of the free end of the beam after the last point of contact between itself and the boundary surface, u' is the transverse displacement of the neutral axis of the beam at its joint with the tip mass, and u is the displacement of the center of mass of the tip mass. For the sake of clarity in the figure, only half of the system is shown as another curved boundary is present on the upper side of the beam, completely bounding its lateral vibration. The beam is loaded by a concentrated load P at the tip and, as it deflects, becomes gradually in contact with the rigid support, such that part of the beam is resting on the support (portion $l-x$), and the remaining portion is free (portion x), working as a regular cantilevered beam but with a shorter length, and slightly tilted. The last point of contact between the beam and the support is indicated in the figure as contact point.

Depending on the applied load and surface order, the beam will wrap around a certain portion of the rigid support, and beyond the contact point, it will deflect a certain distance u' given by:

$$u' = f(l-x) + \frac{\mathrm{d}[f(l-x)]}{\mathrm{d}x}x + \frac{Px^3}{3EI}. \tag{3.1}$$

The first term in Eq. (3.1) is associated with the vertical distance from the equilibrium position to the contact point and it is equivalent to evaluating the surface function f at point $(l-x)$. The second term is the additional vertical distance due to the slope

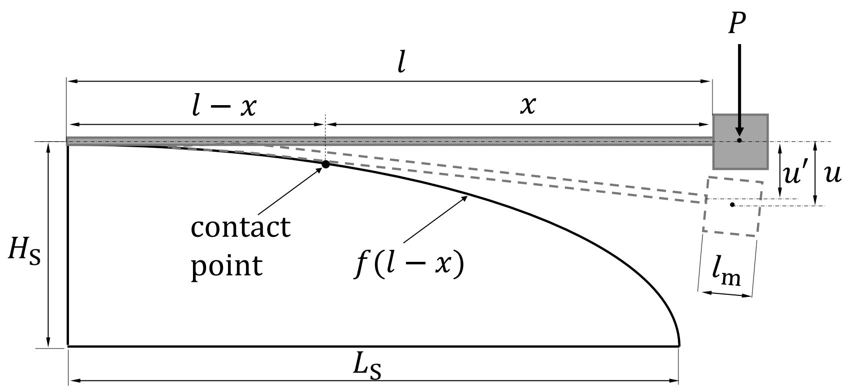

Figure 3.1. : Schematic and dimensions of the nonlinear spring.

of the beam at the contact point. After the beam wraps around portion $l - x$, the free portion of the beam x becomes a new inclined cantilever beam with initial slope given by $\frac{\mathrm{d}[f(l-x)]}{\mathrm{d}(l-x)}$. The distance between the equilibrium position and the tip of this inclined beam is calculated by multiplying the slope by the free end x. The third term is the static deflection of the free portion x due to bending where E and I are the modulus of elasticity of the material, and the second moment of area of the cross-section, respectively. An additional component of the deflection is also contributed by the deflection of the tip of the mass (quantity $u' - u$), which results from the multiplication of half the mass length l_m by the cantilever slope. By combining Eq. (3.1) with the expression of the slope of a cantilever beam, the mass deflection is given by:

$$u = u' + \frac{Px^2}{2EI} + \frac{\mathrm{d}[f(l-x)]}{\mathrm{d}x}x, \tag{3.2}$$

where u, u' and x are clearly indicated in Fig. 3.1. Four examples of surfaces with different surface orders are shown in Fig. 3.2, to give the reader an idea of the topological differences between surface orders. A general expression for the function of the boundary surface is given by:

$$f(l-x) = d(l-x)^n, \tag{3.3}$$

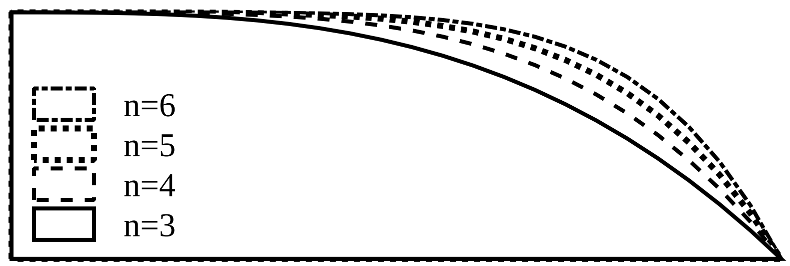

Figure 3.2. : Effect of order n on the boundary surface order.

where

$$d = \frac{H_\mathrm{S}}{L_\mathrm{S}^n}. \tag{3.4}$$

The quantities H_S and L_S (depicted in Fig. 3.1) are the height and length of the rigid surface, and n is the surface order function of the boundary. In this analysis n ranges from 3 to 5 as it was demonstrated that the spring achieves strongly nonlinear characteristics for $n \geq 3$ (Kluger et al., 2015). Depending on the order of the surface function, the length of the beam l is adjusted accordingly to set it equal to the arc length AD, such that a theoretical infinite stiffness is achieved when the beam completely wraps around the surface, leaving no portion of the beam extending beyond the boundary edge.

To determine the characteristic of the nonlinear spring, the force-displacement relationship must be obtained. Thus, the location of the contact point is required for a given applied load. Since the deflection of the beam in this system is not a function of the applied force alone but of the contact point, the calculation is carried out in two steps: 1) determination of the contact point; and 2) determination of the deflection as a function of the contact point. The contact point is obtained by equating the radius of curvature of the surface, approximated by the second derivative of the surface profile function, and the radius of curvature of the beam at the contact point, given by the known formula of radius of curvature of a cantilever beam:

$$\frac{\mathrm{d}^2}{\mathrm{d}x^2}[d(l-x)^n] = n(n-1)d(l-x)^{n-2} = \frac{Px}{EI}. \tag{3.5}$$

Equation (3.5) has a single-valued solution for $n \leq 3$. For $n > 3$, distance x must be obtained using numerical techniques as the expressions for x become polynomials of order $n - 2$. Thus, a closed-form expression for the deflection as functions of the applied force is not realizable for a beam of any order, and a calculation of the total deflection must be carried out for each surface order case, n, according to Table 3.1:

Table 3.1. : Contact point x expressions for each order of n.

n	Expression for x
2	$Px = 2dEI$
3	$Px = 6dEI(l - x)$
4	$Px = 12dEI(l - x)^2$
5	$Px = 20dEI(l - x)^3$

The nonlinear spring defined in Section 3.1.1 has several parameters that can be selected to produce different effects in the static and dynamic responses of the system. Obvious choices are those related to the geometry of the problem including the surface order of the boundary, n, the aspect ratio d, and the length of the beam (l). Moreover, non-geometrical parameters such as the material properties and inertia of the beam will also play a role. The resulting force-displacement curve (P vs u) of the nonlinear spring is a function of the contact point location x, which is expressed implicitly in the equation of motion of the system. An schematic diagram of the nonlinear spring, considering base excitation, is presented in Fig. 3.3

The behavior of this spring can be described by a general nonlinear function $f_{\text{sp}} = f(u)$. This spring force is equivalent to variable P in Section 3.1.1, which is obtained by solving a two-step problem: (1) finding the solution the corresponding equation of Table 3.1, for x; and (2) replacing this solution from step (1) into Eq.(3.1) for f_{sp}. This result is then used to compute a force versus deformation (F-D) characteristic of the spring. The resulting nonlinear stiffness curve is bounded by the

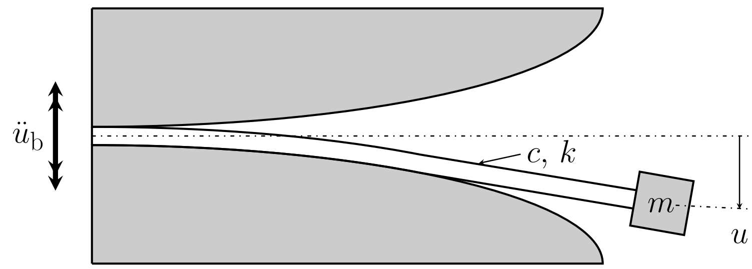

Figure 3.3. : Proposed nonlinear spring subjected to base excitation.

surface height H_{S} on one axis, and the maximum applied force $P_{\mathrm{max},i}$ on the other axis, as indicated in Fig. 3.4, where three example F-D curves are shown.

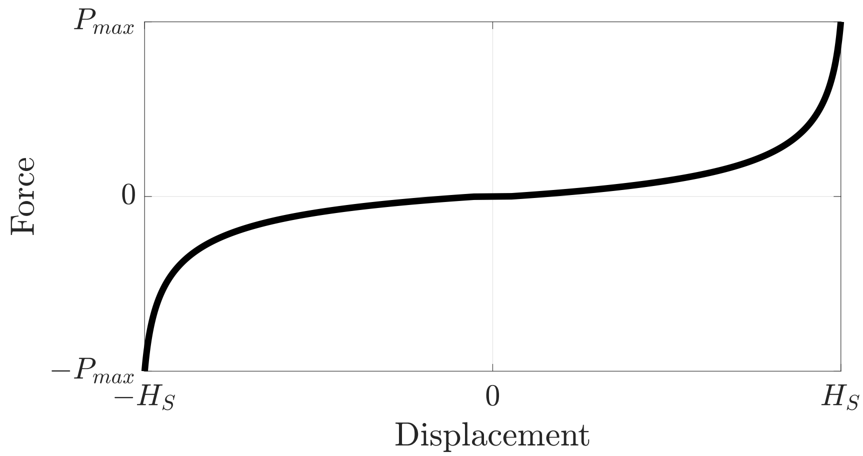

Figure 3.4. : Variation of hardening behavior with the surface order.

For a higher-order boundary surface, a higher force is needed to reach the edge, which in practice means that such system would produce a higher nonlinear stiffness. Because of the nature of this problem, where the stiffness theoretically reaches infinity when the beam fully wraps around the surface and no portion of the beam extends beyond the boundary edge, the F-D diagram has an asymptotic behavior towards the maximum beam deflection (at $u = \pm H_{\mathrm{S}}$). This behavior is difficult to interpolate into an analytic function that can be incorporated into the f_{sp} quantity. One approach is to model this system with an interpolation look-up table as the source of the nonlinear stiffness, and the other to approximate this behavior with a general power series of the form:

$$f_{\mathrm{sp}} = \sum_{j=1}^{N} k_j u^k, \tag{3.6}$$

where N is the order of nonlinearity, consisting of odd powers only as the nonlinearity is an odd function, and k_i are the stiffness coefficients corresponding to each degree of nonlinearity (e.g.: for a cubic nonlinearity, the spring force is $f_{\mathrm{sp}} = k_1 u + k_3 u^3$). The order of nonlinearity, is to be determined in a later section.

3.1.2 Dynamic model

One of the greatest potential uses of this device for passive vibration reduction is its capability to work in any direction of the Cartesian reference frame. Now, a simple and reasonably accurate way to model this system would be to use the beam model of a cantilever beam with a mass on its tip, attached to a nonlinear spring that captures the nonlinearities described in Eq. (3.6). However, to account for the additional inertia, the possibility of the beam undergoing bucking, and the gravitational implications of the device if configured in a vertical direction, a model is proposed based on a pendulum, similar to Huygen's pendulum clock with the main difference being in the rigid boundary surface order. The EOMs are derived using the equations of plane kinematics of rigid bodies.

The system is idealized as an inverted massless pendulum with a concentrated mass m at the tip, fixed at its origin to a moving cart that represents the base acceleration $\ddot{x}_{\mathrm{b}}$, and supported by a side spring of those nonlinear characteristics derived in Section 3.1.1, which is shown schematically in Fig. 3.5.

Here, ϕ is the angle of the pendulum with respect to the vertical equilibrium position, k_{l} and k_{nl} are the linear and nonlinear stiffness coefficients of the spring, c is the damping coefficient, and g represents the gravitational acceleration. Also, several assumptions need to be made, namely that: 1) the beam is rigid, so all bending

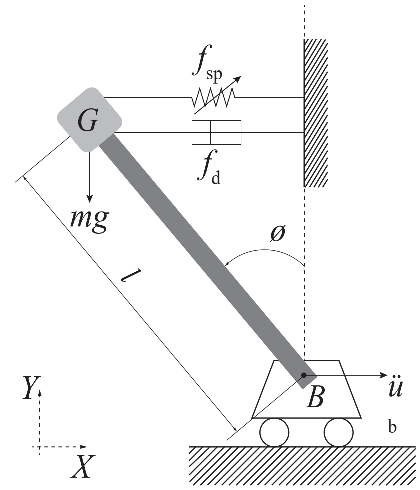

Figure 3.5. : Beam NES schematic.

characteristics from its elastic physical features are assumed to be captured by the nonlinear spring constants; 2) the radius of curvature is constant, which is not true in reality as the length of the beam changes progressively as it wraps around the curved surface of the boundary; and, 3) the beam is massless, as its actual mass is much smaller than the concentrated mass at its tip.

Consider the free body diagram shown on Fig. 3.6. The external forces that produce a moment around point B are the spring force (f_{s}), damping force (f_{d}), and the gravitational force (mg), each one multiplied by the appropriate moment arm length to B. The vector equation of the acceleration of point G, accounting for its relative motion with respect to point A is given by:

$$\mathbf{a}_G = \mathbf{a}_B + \boldsymbol{\alpha} \times \mathbf{r}_{G/B} - \omega^2 \mathbf{r}_{G/B} \tag{3.7}$$

$$= \mathbf{a}_B \hat{\mathbf{i}} + \ddot{\phi}\hat{\mathbf{k}} \times [-l\sin(\phi)\hat{\mathbf{i}} + l\cos\phi\hat{\mathbf{j}}] + [\dot{\phi}^2 l\sin(\phi)\hat{\mathbf{i}} - \dot{\phi}^2 l\cos(\phi)\hat{\mathbf{j}}], \tag{3.8}$$

where $\mathbf{r}_{G/B}$ is the position vector from point G to point B, $\boldsymbol{\alpha}$ is the angular acceleration vector of the beam, ω is the scalar angular velocity of the beam, and $\mathbf{a}$ is the acceleration vector of its corresponding point in the diagram indicated by the

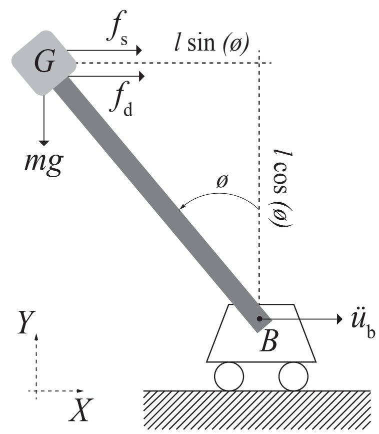

Figure 3.6. : Beam NES free body diagram.

subscript. Note that bold letters represent vector quantities. Now, expanding the cross products of the rightmost side of Eq.(3.7) produces:

$$\mathbf{a}_G = [\mathbf{a}_B - \ddot{\phi} l \cos\phi + \dot{\phi}^2 l \sin(\phi)]\hat{\mathbf{i}} + [-\dot{\phi}^2 l \cos(\phi) - \ddot{\phi} l \sin(\phi)]\hat{\mathbf{j}}, \tag{3.9}$$

and, enforcing Newton's second law for rotational motion, yields the angular acceleration relationship:

$$\sum \mathbf{M}_B = I_G \boldsymbol{\alpha} + \mathbf{r}_{G/B} \times m\mathbf{a}_G, \tag{3.10}$$

where I_G is the rotational moment of inertia of the mass, $\boldsymbol{\alpha} = \ddot{\phi}\hat{\mathbf{k}}$, and the sign convention for positive moments is in the counter clockwise sense. Once more, from the free body diagram, one obtains:

$$\begin{aligned}(mgl\sin\phi + f_{\mathrm{sp}} l \cos\phi + f_{\mathrm{d}} l \cos\phi)\hat{\mathbf{k}} &= I_G \ddot{\phi}\hat{\mathbf{k}} \\ &+ (-l\sin\phi\hat{\mathbf{i}} + l\cos\phi\hat{\mathbf{j}}) \times m[(\mathbf{a}_B - \ddot{\phi} l \cos\phi)\hat{\mathbf{i}} - \ddot{\phi} l \sin\phi\hat{\mathbf{j}}].\end{aligned} \tag{3.11}$$

After computing all the cross-products, the resulting expression is only in the $\hat{\mathrm{k}}$ direction, as expected for planar rotation, so the directional vector is dropped:

$$(mgl\sin\phi + f_{\mathrm{sp}} l \cos\phi + f_{\mathrm{d}} l \cos\phi) = I_G \ddot{\phi} + m\ddot{\phi} l^2 - ma_B l \cos\theta.$$

The nonlinear spring force given in Eq. (3.6), is thus substituted into the equation above, the base acceleration variable name is changed to $\ddot{u}_{\mathrm{b}}$, the equation in expressed in terms of angular moments, and assuming small angle approximations yield:

$$(I_G + ml^2)\ddot{\phi} + cl(l\dot{\phi}) + k_{\mathrm{l}}l(l\phi) + k_{\mathrm{nl}}l(l\phi)^{\beta} - mgl(l\phi) = -ml\ddot{u}_{\mathrm{b}}. \tag{3.12}$$

This constitutes the equation of motion (EOM) of this class of nonlinear spring in terms of angular states. Clearly, this expression captures more of the underlying physics of the system, as correction terms are present for the inertial mass of the device (in the form of $(I_G + ml^2)$), and gravitational effects (in the form of mgl). The base acceleration takes the form $\ddot{u}_{\mathrm{b}} = A\Omega_{\mathrm{r}}^2 \cos\Omega_{\mathrm{r}} t$, where A is the prescribed amplitude of the displacement, and Ω_{r} is the excitation frequency. In order to retrieve the motion states in the u direction, a simple substitution has to be made to the ϕ quantity recalling that $u = l\phi$. Thus the angular and linear quantities are related by:

$$u = l\phi, \quad \dot{u} = l\dot{\phi}, \quad \ddot{u} = l\ddot{\phi}.$$

3.1.3 System expressed in nondimensional form

The relative contribution of terms in Eq. (3.12) must be evaluated through nondimensionalization. By scaling the time variable by the characteristic time, T_{c}, and noting that the displacement is already in nondimensional form, as it is expressed in radians, let:

$$\tau = \frac{t}{T_{\mathrm{c}}}, \quad \varphi = \phi, \quad \varphi' = T_{\mathrm{c}}\dot{\phi} \quad \varphi'' = T_{\mathrm{c}}^2\ddot{\phi}, \tag{3.13}$$

where $T_c = \sqrt{\frac{I_{\mathrm{eff}}}{k_1 l^2}}$, and $I_{\mathrm{eff}} = I_G + ml^2$. Substituting Eqns. (3.13) into Eq. (3.12), and simplifying:

$$\varphi'' + \mu\varphi' + (1-\lambda)\varphi + \epsilon\varphi^{\beta} = \Lambda\Omega_{\mathrm{r}}^2 \cos\Omega_{\mathrm{r}}\tau, \tag{3.14}$$

where:

$$\mu = \frac{cl^2}{\sqrt{I_{\mathrm{eff}}(k_1 l^2)}}, \quad \varepsilon = \frac{k_{\mathrm{nl}} l^{\beta+1}}{k_{\mathrm{l}}}, \quad \Omega_r = \omega\sqrt{\frac{I_{\mathrm{eff}}}{k_1 l^2}}, \tag{3.15}$$
$$\lambda = \frac{mg}{k_1 l}, \quad \text{and} \quad \Lambda = \frac{mAl}{k_{\mathrm{l}} l^2}.$$

Note that λ represents the critical mass needed to induce buckling if the cantilevered is mounted vertically. The relative difference between the linear and nonlinear term of the stiffness confirms indeed that the system is highly nonlinear, based on the fact that the nonlinear stiffness term is several orders of magnitude greater than the linear stiffness term.

3.2 Approximate analytical solution

An approximation of the analytical solution of the developed EOMs is presented. A preliminary step in determining a set of adequate parameters for having a fully described system is also required.

3.2.1 Parametric design

With the EOM and F-D characteristics completed, a parametric model is generated from physical constraints defined beforehand for this nonlinear spring, mainly ensuring that it would be easy to build, from commercially available materials, and that it shall produce relevant results when attached to existing physical components available in the lab, which are expected to be used during the experimental verification of the model. Thus, physical characteristics for the spring are defined accordingly, and shown in Table 3.2. The rigid boundaries are defined and assumed to be made from a material such that elasticity does not play a role when interacting with the beam, and friction implications are considered to be within the status of a lightly damped system. It should also be mentioned that the tip mass considers the additional weight of the instrumentation and bolts that will be used in the physical realization of the experiments.

With all the constant parameters defined and assumed, MATLAB interpolation capabilities through the function `cftool.m` is used to obtain a fit to the curves generated in the static analysis. From the combined use of Eq. (3.5), Table 3.1, and

Table 3.2. : Material and geometric properties of the nonlinear spring.

CONSTANT PARAMETERS			
Parameter	**Value**	**Units**	**Notation**
Beam width (measured)	12.7	mm	b
Beam thickness (measured)	0.9	mm	h
Tip mass (measured)	0.13	kg	m
Boundary height (measured)	50.8	mm	H_{S}
Boundary length (measured)	150	mm	L_{S}
2nd moment of area (calculated)	0.743	mm^4	$I = \frac{bh^3}{12}$
Elastic modulus (from material)	200×10^9	Pa	E
Gravitational acceleration (constant)	9.81	$\mathrm{m/s}^2$	g
VARIABLE PARAMETERS			
Surface order 1	3		n
Surface order 2	5		n
Beam length ($n = 3$, meas.)	165	mm	l
Beam length ($n = 5$, meas.)	173	mm	l

subsequent fitting of the F-D curve, the resulting form of the nonlinear stiffness defined in the power series of Eq. (3.6) is:

$$f_{\mathrm{sp}} = k_{\mathrm{l}}u + k_{\mathrm{nl}}u^9. \tag{3.16}$$

Several candidates for the spring force were considered here, from a purely cubic, quintic, order 7 and order 9 expression, to combinations thereof. The criteria for selecting the final shape included the smoothness of the interpolation, the coefficient of determination given by the R^2, and the root mean squared error to evaluate the degree of correlation between the calculated and interpolated F-D curves. The expression that produced the highest R^2 value with smoother behavior was a ninth-order polynomial nonlinear force. It should be mentioned that a combined polynomial including intermediate powers of u would produce an undesired wiggly behavior in the interpolated curve. Coefficients corresponding to two boundary surface order cases ($n = 3$, and $n = 5$) extracted from interpolating the F-D curves of Fig. 3.7 are shown in Table 3.3.

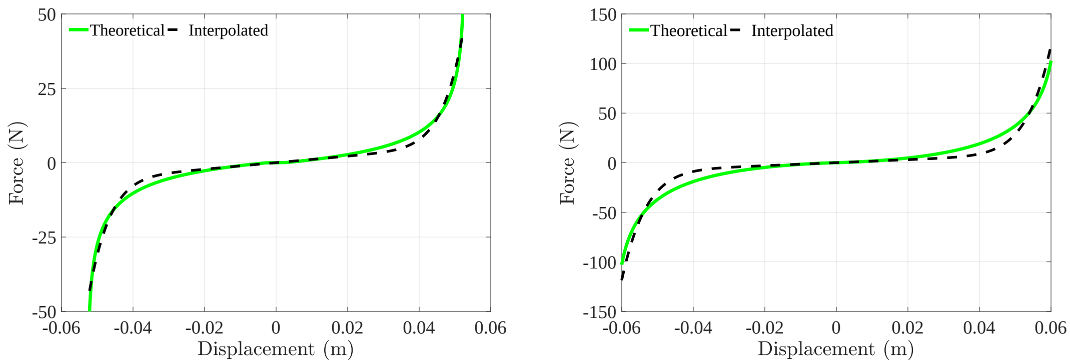

(a) Case 1: $n = 3$ (b) Case 2: $n = 5$

Figure 3.7. : Nonlinear spring polynomial stiffness interpolation.

Table 3.3. : Nonlinear stiffness parameters and natural frequencies of the unbounded cantilever beam.

Surface order	k_1 (N/m)	k_9 (N/m^9)	ω_n (Hz)
$n = 3$	110	1.307×10^{13}	3.97
$n = 5$	150	1.084×10^{13}	4.15

3.2.2 Damping identification

In order to identify the linear damping and linear natural frequency of the system, the cantilevered oscillator with mass attached is clamped horizontally to the table and given an initial excitation (hammer hit). The response is recorded and shown in Fig. 3.8.

Table 3.4. : Damping and natural frequency estimates due to small perturbation.

	Exp.	ω_n (rad/s)	ζ
	1	25.8393	0.0049
n=3	2	25.8393	0.0049
	3	25.8393	0.0049
	1	29.1135	0.0056
n=5	2	29.1135	0.0056
	3	29.1135	0.0056

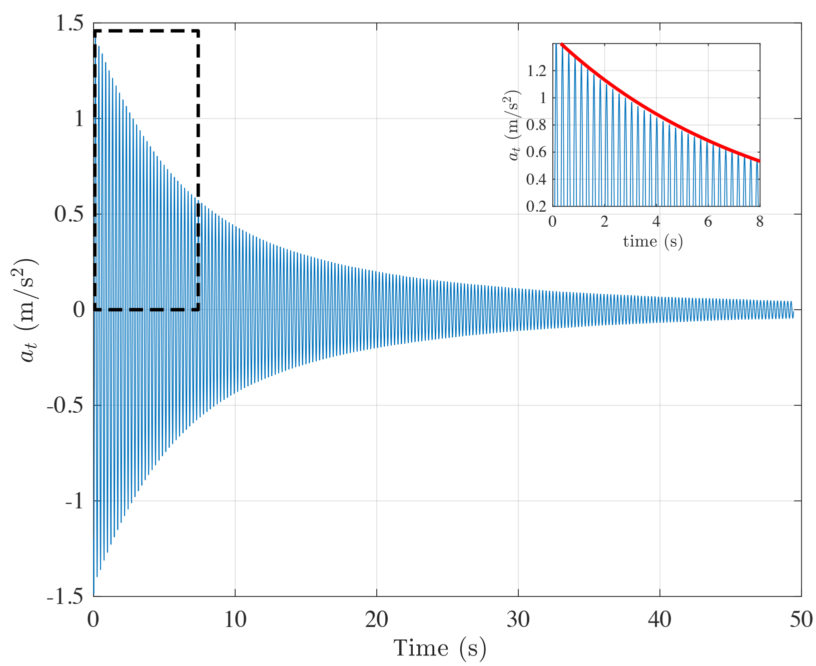

Figure 3.8. : Time waveform for linear fit of ω_n and ζ.

Once these preliminary steps are completed, numerical simulations of the determined nonlinear spring of 9^{th} order, using the derived EOM corresponding to the two cases in hand ($n = 3$ and $n = 5$) are carried out using Simulink (The Mathworks Inc., 2018), with a Runge-Kutta (ode45) integrator, running at a variable time step within the `ode45.m` environment. Three numerically-generated sine dwell diagrams are run between frequencies of interest: from 3.0 to 5 Hz, for the case of $n = 3$, and from 4 to 6 Hz, for the case of $n = 5$ surface order. Each run is carried out at amplitudes of 0.8, and 1.2 mm. To generate the frequency domain response numerically, the integration is performed in ascending order of frequencies (forward integration), and then in descending order of frequencies (backward integration) at each excitation frequency point, using the last steady state maximum amplitude as the initial condition for the next frequency point.

3.2.3 System response near resonance

Due to the high-order terms present in the EOM, a closed-form solution is rather difficult to obtain. Therefore, a numerical approximation through perturbation methods, specifically the method of harmonic balance, is posted as an alternative. Recall Eq. (3.14) and using the relationship of the nonlinear force of Eq. (3.6), corrected for φ ($f_{\text{sp}} = \varphi + \varepsilon\varphi^9$), the dynamic model results in the expression:

$$\varphi'' + \mu\varphi' + (1 - \lambda)\varphi + \varepsilon\varphi^{\beta} = \Lambda\Omega_r^2 \cos\Omega_r\tau, \tag{3.17}$$

where Ω_{r} is the frequency of excitation normalized by the linear natural frequency, and the remaining parameters were already defined in Eq. 3.15. Due to the difficulty in obtaining an analytical solution for the differential equation of motion of the spring due to the high order of the nonlinear force, an alternative approach of analysis using the method of harmonic balance is sought, as this method is suitable for systems with polynomial nonlinear terms and strong nonlinearities (hardening type). Therefore, a solution is assumed of the form

$$\varphi(t) \approx \varphi_{\text{h}} = A\cos(\Omega_{\text{r}}\tau) + B\sin(\Omega_{\text{r}}\tau), \tag{3.18}$$

where A and B are the Fourier coefficients. Here, single frequency is assumed as we are only interested in low frequency harmonics. The detailed procedure of derivation is mathematically extensive, yielding long expressions. Therefore, some steps of the procedure are briefly mentioned herein. Substituting Eq. (3.18) in Eq. (3.17) yields an expression in terms of powers of sines and cosines:

$$\begin{aligned}
&- A\Omega_{\mathrm{r}}^2 \cos(\Omega_{\mathrm{r}}\tau) - B\Omega_{\mathrm{r}}^2 \sin(\Omega_{\mathrm{r}}\tau) - \lambda A\Omega_{\mathrm{r}} \sin(\Omega_{\mathrm{r}}\tau) + \lambda B\Omega_{\mathrm{r}} \cos(\Omega_{\mathrm{r}}\tau) \\
&+ A\cos(\Omega_{\mathrm{r}}\tau) + B\sin(\Omega_{\mathrm{r}}\tau) + \varepsilon A^9 \cos(\Omega_{\mathrm{r}}\tau)^9 + 9\varepsilon A^8 \cos(\Omega_{\mathrm{r}}\tau)^8 B\sin(\Omega_{\mathrm{r}}\tau) \\
&+ 36\varepsilon A^7 \cos(\Omega_{\mathrm{r}}\tau)^7 B^2 \sin(\Omega_{\mathrm{r}}\tau)^2 + 84\varepsilon A^6 \cos(\Omega_{\mathrm{r}}\tau)^6 B^3 \sin(\Omega_{\mathrm{r}}\tau)^3 \\
&+ 126\varepsilon A^5 \cos(\Omega_{\mathrm{r}}\tau)^5 B^4 \sin(\Omega_{\mathrm{r}}\tau)^4 + 126\varepsilon A^4 \cos(\Omega_{\mathrm{r}}\tau)^4 B^5 \sin(\Omega_{\mathrm{r}}\tau)^5 \\
&+ 84\varepsilon A^3 \cos(\Omega_{\mathrm{r}}\tau)^3 B^6 \sin(\Omega_{\mathrm{r}}\tau)^6 + 36\varepsilon A^2 \cos(\Omega_{\mathrm{r}}\tau)^2 B^7 \sin(\Omega_{\mathrm{r}}\tau)^7 \\
&+ 9\varepsilon A\cos(\Omega_{\mathrm{r}}\tau) B^8 \sin(\Omega_{\mathrm{r}}\tau)^8 + \varepsilon B^9 \sin(\Omega_{\mathrm{r}}\tau)^9 + \Omega_{\mathrm{r}}^2 \Gamma F_0 \sin(\Omega_{\mathrm{r}}\tau) = 0.
\end{aligned} \tag{3.19}$$

Expanding and using trigonometric identities for reducing these power terms (e.g.: $\sin^3(\Omega_{\mathrm{r}}\tau) - \frac{3}{4}\sin(\Omega_{\mathrm{r}}\tau) = \frac{1}{4}\sin(3\Omega_{\mathrm{r}}\tau)$, and so on), produces an expression in terms of sines and cosines of multiple angles up to $(9\Omega_{\mathrm{r}}\tau)$. All the higher order $(> 3\Omega_{\mathrm{r}}\tau)$ terms are dropped as only lower harmonics are of interest here. Next, gathering the fundamental harmonics in sine yields:

$$\begin{aligned}
A + (63/128)\varepsilon A^9 + (63/32)\varepsilon A^3 B^6 + (63/128)\varepsilon AB^8 - MA\Omega_{\mathrm{r}}^2 + CB\Omega_{\mathrm{r}} \\
+ (63/32)\varepsilon A^7 B^2 + (189/64)\varepsilon A^5 B^4 = 0,
\end{aligned} \tag{3.20}$$

and an equation for the cosine terms, given by:

$$\begin{aligned}
B + (63/128)\varepsilon B^9 + (189/64)\varepsilon A^4 B^5 + (63/32)\varepsilon A^2 B^7 - MB\Omega_{\mathrm{r}}^2 - CA\Omega_{\mathrm{r}} + \\
(63/128)\varepsilon A^8 B + (63/32)\varepsilon A^6 B^3 = -\Omega_{\mathrm{r}}^2 \Gamma.
\end{aligned} \tag{3.21}$$

At this point, a polar substitution is made such that $A = a\cos(\theta)$, and $B = b\cos(\theta)$, to both Eq. (3.20), and Eq. (3.21). This produces two expressions in power terms of $\sin(\theta)$, and $\cos(\theta)$, let's call them h_1 and h_2, respectively. Now, equation h_1 is again multiplied by $\sin(\theta)$ to produce equation f_1, and by $\cos(\theta)$ to produce equation

f_2. Similarly, equation h_2 is also multiplied by $\sin(\theta)$ to produce equation g_1, and by $\cos(\theta)$ to produce equation g_2. The reason for doing these artifices is to eliminate trigonometric terms by combining the formed equations. After combining and reducing, using trigonometric identities, equations f_1+f_2, and g_1+g_2, two phase equations are generated, which are given by:

$$a + \frac{63}{128}\varepsilon a^9 - Ma\Omega_{\mathrm{r}}^2 = \Omega_{\mathrm{r}}^2 \Gamma F_0 \cos(\theta), \tag{3.22}$$

and:

$$\lambda a \Omega_{\mathrm{r}} = \Omega_{\mathrm{r}}^2 \Gamma F_0 \cos(\theta). \tag{3.23}$$

Squaring and adding Eq. (3.22) and Eq. (3.23), and recalling the relationship $\sin^2(\theta) + \cos^2(\theta) = 1$, the final simplified expression of the frequency-amplitude relationship is:

$$\frac{3969}{16384}\, a^{18}\varepsilon^2 - \frac{63}{64}\, a^{10}\varepsilon{\Omega_{\mathrm{r}}}^2 + \frac{63}{64}\, a^{10}\,\varepsilon + a^2{\Omega_{\mathrm{r}}}^4 - 2\, a^2\Omega_{\mathrm{r}}^2 + a^2 + \lambda^2 a^2{\Omega_{\mathrm{r}}}^2 = F_0\Gamma^2\Omega_{\mathrm{r}}^4. \tag{3.24}$$

This equation produces a polynomial of order 18 in a, that can be solved numerically for the roots that constitute the amplitude response level of the system for different forcing frequencies Ω_{r}. At each frequency point, the polynomial produces nine roots, which contain both real and imaginary values. From these, only the real roots are of relevance in the present analysis for constructing the frequency response curve.

3.2.4 Stability analysis

Floquet theory is used to evaluate the stability of the periodic solutions derived from the harmonic balance technique in Section 3.2.3. The periodic solution $\phi(t)$ is perturbed by a disturbance $\xi(t)$, such that ϕ_{h} becomes $\phi_{\mathrm{h}} + \xi(t)$ (subscript $()_h$

denotes 'harmonic'). Then, the system is expressed as a set of first order differential equations:

$$\begin{aligned} \ddot{\varphi}_1 &= \varphi_2 \\ \ddot{\varphi}_2 &= -\lambda\phi_2 - \varphi_1 - \varepsilon\varphi_1^9. \end{aligned} \tag{3.25}$$

Now, let's perturb the solutions to the system of Eq. (3.25) by a small perturbation ξ, such that:

$$\begin{aligned} \phi_1(t) &= \phi_{1,0} + \xi_1(t) \\ \phi_2(t) &= \phi_{2,0} + \xi_2(t), \end{aligned} \tag{3.26}$$

and noting that:

$$\begin{aligned} \phi_{1,0}(t) &= b\cos\Omega_{\mathrm{r}}t \\ \phi_{2,0}(t) &= \dot{u}_{1,0}(t) = -b\Omega_{\mathrm{r}}\sin\Omega_{\mathrm{r}}t. \end{aligned} \tag{3.27}$$

After replacing Eqs. (3.27) into Eqs. (3.26), a system of two first order differential equations with state variables $[\xi_1 \quad \xi_2]^\intercal$ is obtained. Then, rearranging and simplifying such that only first order terms of ξ_1, and ξ_2 are retained, the perturbed system can be expressed in state-space form as:

$$\begin{bmatrix} \dot{\xi}_1 \\ \dot{\xi}_2 \end{bmatrix} = \begin{bmatrix} 0 & 1 \\ -1 - 9\varepsilon u_{10}^8 & -\lambda \end{bmatrix} \begin{bmatrix} \xi_1 \\ \xi_2 \end{bmatrix}. \tag{3.28}$$

To assess the stability of the linearized equations, the monodromy matrix is obtained by integrating system (3.28) from $t = 0$ to $t = T = 2\pi/\Omega_{\mathrm{r}}$, i.e., a full period of the excitation. This is accomplished by determining two solution vectors:

$$\boldsymbol{\xi_1}(t) = \begin{bmatrix} \xi_{11}(t) \\ \xi_{12}(t) \end{bmatrix} \quad \text{and} \quad \boldsymbol{\xi_2}(t) = \begin{bmatrix} \xi_{21}(t) \\ \xi_{22}(t) \end{bmatrix} \tag{3.29}$$

which satisfy the following initial conditions:

$$\begin{bmatrix} \xi_{11}(0) \\ \xi_{12}(0) \end{bmatrix} = \begin{bmatrix} 1 \\ 0 \end{bmatrix} \quad \text{and} \quad \begin{bmatrix} \xi_{21}(0) \\ \xi_{22}(0) \end{bmatrix} = \begin{bmatrix} 0 \\ 1 \end{bmatrix}. \tag{3.30}$$

The identity matrix is used as initial condition. This allows the monodromy matrix to be:

$$\Phi = \begin{bmatrix} \xi_{11}(T) & \xi_{21}(T) \\ \xi_{12}(T) & \xi_{22}(T) \end{bmatrix}. \tag{3.31}$$

The eigenvalues of Φ, known as the Floquet or characteristic multipliers indicate whether the solution corresponding to the associated frequency is stable, according to the next criteria:

1. The Floquet multiplier leaves the unit circle through $\mathrm{Re} = +1$, resulting in a *transcritical* (TC), *symmetry breaking* (SB), and *cyclic fold* (CF) bifurcation.

2. The Floquet multiplier leaves the unit circle through $\mathrm{Re} = -1$, resulting in a *period doubling bifurcation* (PD).

3. The Floquet multiplier in the form of a pair of complex conjugates leave the unit circle away from the real axis resulting in a *secondary Hopf* or *Neimark-Sacker bifurcation* (Nayfeh and Balachandran, 2004; Krack and Gross, 2019)

It is expected that for the present case, the Floquet multipliers start occurring within the unit circle as pairs of complex conjugates, progressing towards $\mathrm{Re} + 1$ at which point they leave the unit circle the moment that the system bifurcates into two solutions. They remain outside of the unit circle while the system is unstable (in the folding region), and return inside the unit circle once the system again reaches stability. This will be apparent in the results section.

3.3 Numerical and experimental outcomes

The proposed dynamics of the ninth-order nonlinear spring, are numerically simulated using appropriate computational tools, and their response is examined both in the frequency and time domains. Then, an experimental verification of the strength of the model is provided.

3.3.1 Computational simulations

With the dynamic model constructed and its corresponding numerical constants and parameters properly determined, numerical simulations of the ninth-order spring corresponding to the two cases in hand ($n = 3$ and $n = 5$) are carried out using Simulink (The Mathworks Inc., 2018), with a Runge-Kutta (ode4) integrator, running at a variable time step within the `ode45.m` environment. Two numerically-generated sine dwell diagrams are run between the frequencies of interest: from 3.0 to 6 Hz, for both cases of surface order. Each run is conducted at amplitudes of 0.8 and 1.2 mm. To generate the frequency domain response numerically, the integration is performed in ascending order of frequencies (forward integration), with a simulation time to reach steady state estimated in 500 cycles of oscillation at each frequency point, using the last steady-state maximum amplitude as the initial condition for the next frequency point. The same procedure is followed in descending order of frequencies (backward integration). The reason to run simulations in ascending and descending orders is to capture the unstable regions of the plot. The obtained frequency responses are then correlated both with the approximate analytical solution obtained in Sec. 3.2.3, and with the experimental measurements to be explained in the next section.

3.3.2 Experimental measurements

To demonstrate the applicability of this dynamic model, a set of experiments is conducted in the Intelligent Infrastructure Systems Lab at Purdue University. First, a prototype device is designed and fabricated, sized properly to fit and use the existing facilities available in the lab. Next, a series of sine sweeps are applied as base excitation to the device. Then, data is collected for use in the process of model verification. This process is repeated for both the $n = 3$ and $n = 5$ cases described in Section 3.2.1. Data is collected using a VibPilot8 DAQ data acquisition box, manufactured by m+p International, with built-in anti-aliasing filtering and the capability to sample at frequencies up to 10 kHz. For these experiments, data is acquired at a sampling rate of

256 Hz to minimize large data set sizes. The acceleration transducers utilized for this test were two PCB Piezoelectric accelerometers model 333B40, adequate for frequencies in the range of [0.5 Hz to 10 kHz], with ICP® type excitation. Base displacement data is also collected along the acceleration records, and was measured with a built-in LVDT in the actuator of the shake table.

The nonlinear spring is designed in such a way that it can be mounted on any flat surface of appropriate dimensions. A mounting bracket is used to attach the device to any base structure with a flat face, on any configuration. This bracket also works as a mounting vise to fix the device to the rigid surfaces while applying pressure to the beam to maintain a tight cantilevered boundary condition. The device fabricated in a CNC machine at the Mechanical Engineering machine shop, at Purdue University, and is shown in Fig. 3.9.

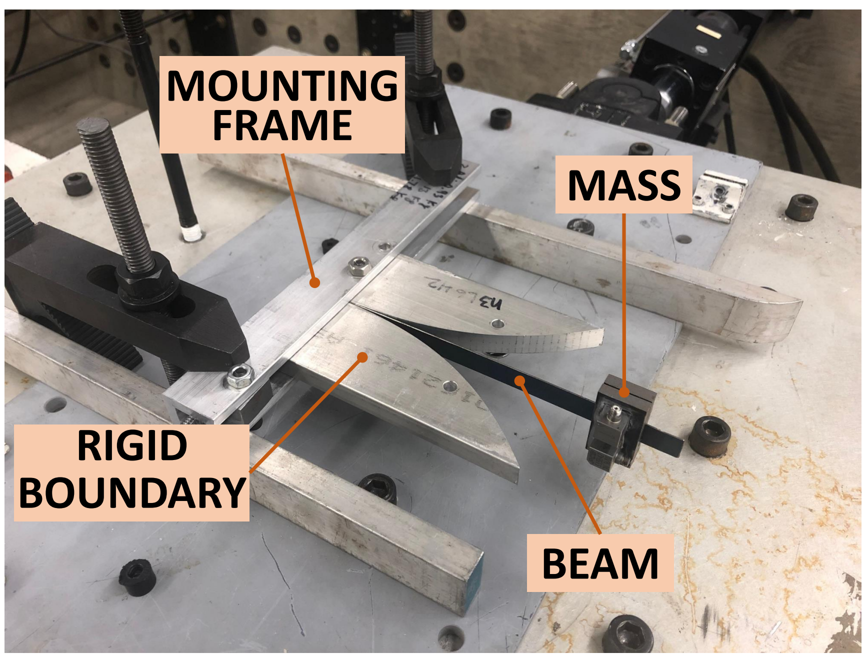

Figure 3.9. : Physical realization of the nonlinear device.

The spring assembly is mounted on a six-DOF servo hydraulic shake table manufactured by Shore Western Manufacturing, controlled by a SC-6000 PID-type servo controller at each DOF. The shake table dimensions are 760 × 760 mm, with a maximum payload capacity of 200 kg. The acceleration transducers are tightly glued to the mass at the tip of the beam, for recording the acceleration of the motion in both directions of the trajectory. Because the actual motion of the mass travels on a curved trajectory, and the transducers used are single direction, it is not possible to directly record measurements in the rectilinear directions (u and v), rather accelerations are recorded in normal and tangential coordinates, which are later corrected with the appropriate angle to horizontal and vertical components (Fig. 3.10). It should be mentioned that although only the horizontal component ($\ddot{x}$) is being compared in the present study, both components are collected for completeness.

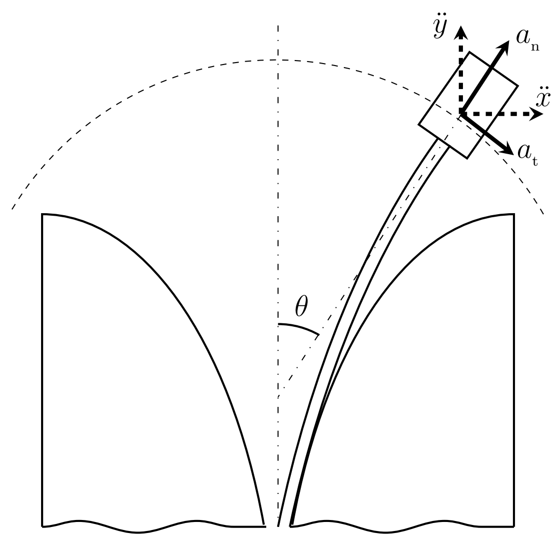

Figure 3.10. : Angle correction of the measured data to convert acceleration from normal-tangential to Euclidean.

Post processing of the collected data includes a step of two-way (ascending and descending direction of the data set) low-pass filtering to eliminate high frequency noise, and minimize phase shifts to the signals. The filter used is a Butterworth low-pass filter of order 8 and a cut off frequency of 12 Hz.

The rigid surface is interchangeable to different sets, depending on the case of interest. For the present experiment, following the numerical cases mentioned earlier, two sets of surfaces are fabricated: one for surface order $n = 3$, and one for surface order $n = 5$. The mass is attached as a separate insert, and can conveniently slide the beam in or out to accommodate the appropriate length, as the arc lengths of the boundaries are different, depending on the surface order. The fabricated pairs of boundaries are shown in Fig. 3.11.

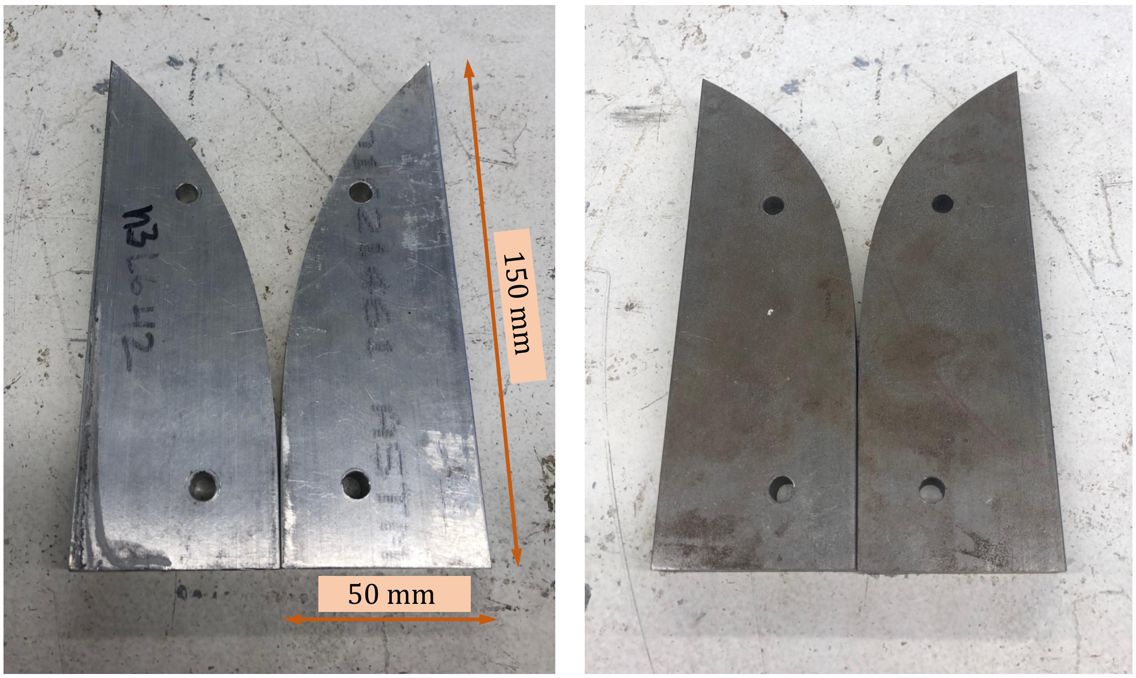

(a) $n = 3$ (b) $n = 5$

Figure 3.11. : Boundary surfaces.

The verification procedure starts by subjecting the specimen to sine dwells at very slow frequency rates, allowing the system to reach steady state and recording the amplitude before a frequency step is made. The excitation is imposed replicating the numerical simulations (i.e., from 3 to 6 Hz with increments of 0.1 Hz). The excitation time at each frequency point is set such that the device completes 250 to 400 cycles, depending on the level of transiency (approximately from 45 to 70 s).

The steady-state acceleration amplitudes measured during the experiments are correlated with those found in the numerical simulations, both in the forward and backward integration schemes, and then compared with the approximate analytical solution found from the method of harmonic balance. All of the quantities were corrected such that they could be depicted in the u direction, as the experimental measurements were made with linear directional accelerometers instead of angular. The responses of the tested cases corresponding to boundary surface order $n = 3$ are presented in Fig. 3.12, with the following clarifications: 1) each plot contains the numerical simulations both in forward and backward integration fashion, superimposed to the experimental measurements and the approximate solution, as indicated in the legends; 2) the top plot corresponds to the low amplitude case ($A = 0.8\,\mathrm{mm}$); and, 3) the bottom row corresponds to the high amplitude case ($A = 1.2\,\mathrm{mm}$).

The simulation results for $n = 3$ offer a reasonably close match between the approximate analytical solution of the harmonic balance method for all of the cases, both in frequency (peaking at approximately 4.3 Hz on all cases), and in amplitude, differing only at the end of the hardening peak, which is expected as the harmonic balance shows a trend in hardening towards higher frequencies. Moreover, the inverted pendulum model developed earlier and the analytical solution compare reasonably well both in frequency and amplitude. However, the measured response, does not agree as close to the analytical response as would be expected. Several possible causes can be attributed for this outcome, some of which include 1) unmodeled dynamics in the chosen modeling approach; 2) measurement errors and uncertainties in several parameters, such as the effective beam length, the actual mass, including the added dynamics produced by the transducer cables; 3) errors associated with reaching steady-state in the sine-dwell experiments; 4) frequency stepping up during the sine-dwell experiments, which includes a fast ramp to zero between frequency points; 5) possible inhomogeneity of the beam material properties; 6) differences between command and measured displacement in the shake table likely due to measurement noise introduced by the system in general, or by the hydraulic system in particular (both base displacement and acceleration are measured quantities) and; 7) the resolution of the experiment, which is not very high, and may cause the system to loose the continuity of amplitude at those locations. Higher resolution in these types of experiments is difficult to achieve due to the length needed for each sine dwell to reach steady-state. A trade-off between dwell time and resolution is always a challenge. The stability of these results is also checked by monitoring the evolution of the Floquet multipliers, in a unit circle diagram where they are traced as the frequency of excitation is increased. This can be observed in Fig. 3.12(c), where the leaving and reentry of the multipliers from the unit circle occurs at 4.2 and 4.4 Hz, respectively, which is consistent with the simulated, experimental and analytical results.

Similarly, the simulation results for case $n = 5$, presented in the pair of plots in Fig. 3.13 show a close correlation between the solution from harmonic balance with the results of the simulations, both in ascending and descending integration order. The resonant peak occurs at around 4.9 Hz with a slight divergence towards higher amplitudes, returning to its stable branch at around 5.2 Hz. This result is also confirmed by looking at the evolution of the Floquet multipliers (see Fig. 3.13(c), where the occurrence of the values leaving and reentering the unit circle happens at exactly the same frequencies listed above. Another interesting observation that can be derived from the results presented in Figs. 3.12 and 3.12 is that the model is able to capture the energy threshold in a similar way as the device behaves in reality. Though the system is essentially nonlinear, as at every amplitude of vibration the beam is oscillating at a different frequency within the frequencies of study, it is expected that at low amplitudes, the device would behave more closely to a linear cantilever. Nevertheless, for the two cases presented here, the nonlinearity appears clearly both in the modeled as well as in the measured responses.

3.3.3 Summary

The application of a nonlinear spring, based on a cantilever beam with a concentrated mass at the tip, whose transverse vibration is constrained by a specially-shaped rigid boundary is proposed here as a possible option for vibration attenuation applications. A semi-analytical dynamic model is developed based on the equations of plane kinematics of rigid bodies. First, a static analysis is performed to determine that the nonlinearity can be described as a ninth order spring, due to the pronounced F-D behavior; and second, equations of motion are derived inserting this F-D characteristic. Numerical simulations demonstrate that the model captures the amplitudes and frequencies of oscillation reasonably well when the device is subjected to different amplitudes of excitation, if compared to the approximate analytical solution obtained from the harmonic balance approximation. However, these results compare in less degree with the experimental measurements due to various possible reasons, some of which include unmodeled dynamics and uncertainties in the experimental setup. The broadband capacity of the nonlinear spring is studied, with the aid of wavelet transform spectra plots, and it is further verified for various amplitudes of excitation for both surface orders. Finally, a series of laboratory experiments are also conducted for selected cases of physical realizations of the proposed device. The observed results compared with the simulations as well as with the analytical solution show a fairly approximate match in amplitude though a bit better in frequency. These results suggest that this class of spring behaves as a nonlinear element with great potential for vibration absorption applications. From the experimental studies, it became apparent that as the surface order of the limiting boundary grows, the nonlinear behavior of the spring also increases (behavior hardens), which in turn demonstrate the intrinsic amplitude-dependency of most nonlinear systems of this class.

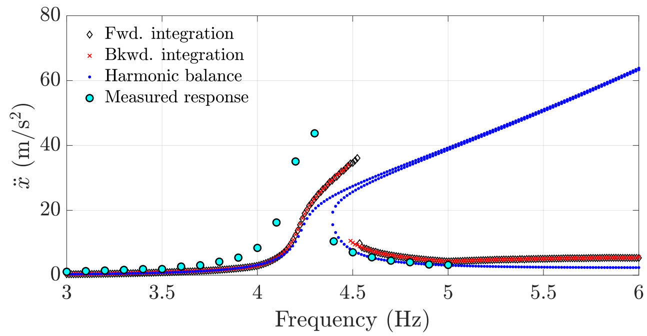

(a) Amplitude 0.8 mm

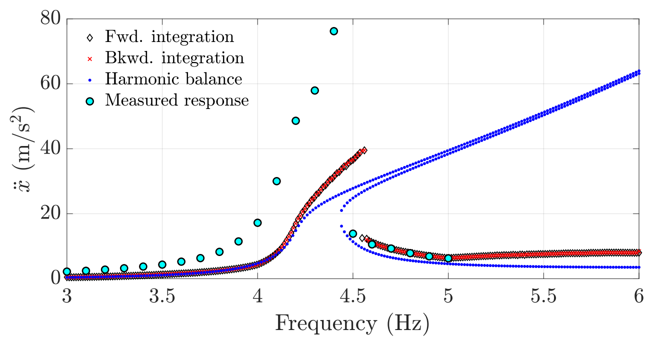

(b) Amplitude 0.8 mm

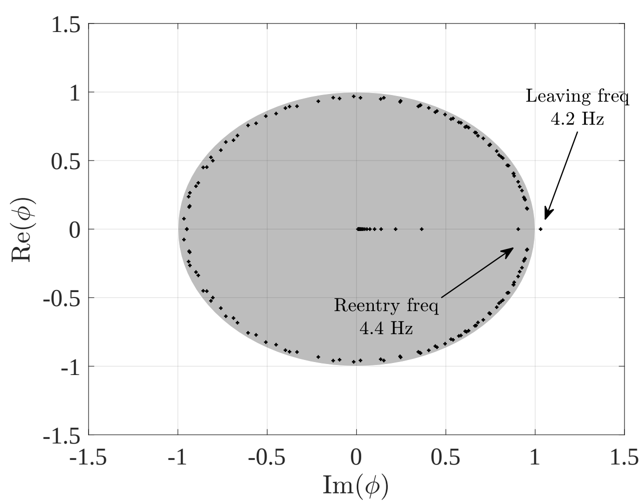

(c) Evolution of stability

Figure 3.12. : Approximate analytical, simulated and experimental responses of the dynamic nonlinear spring system, $n = 3$.

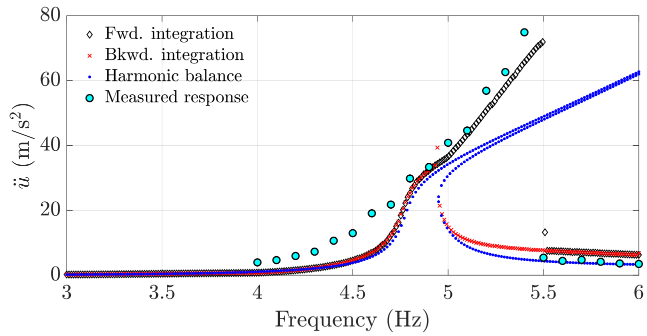

(a) Amplitude 0.8 mm

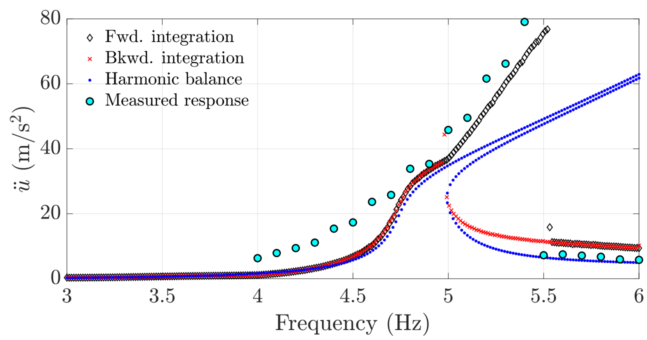

(b) Amplitude 0.8 mm

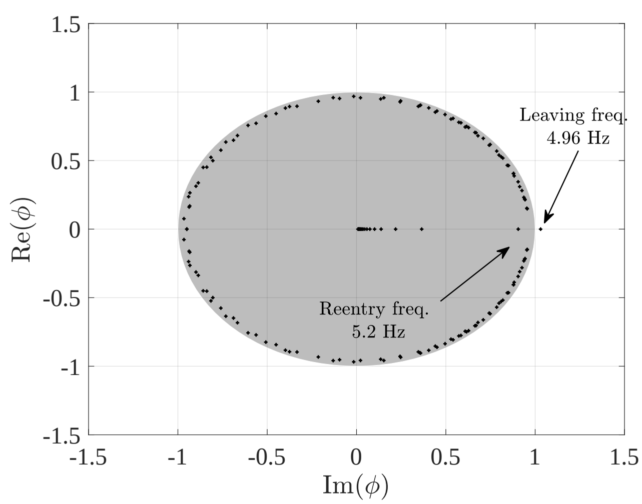

(c) Evolution of stability

Figure 3.13. : Approximate analytical, simulated and experimental responses of the dynamic nonlinear spring system, $n = 5$.

4. NUMERICAL AND EXPERIMENTAL INVESTIGATION OF PROPOSED NES PERFORMANCE, USING A SMALL-SCALE BASE STRUCTURE

Chapters 2 and 3 were devoted to examining possible ways to reduce backflow in an NES by means of using the power information, and to modeling the dynamics of a nonlinear spring for its potential application in a new type of NES. Though Chapter 2 is more focused on the introduction of a visualization technique that allows optimizing parameters of the device for achieving a superior performance, it presents a small experimental validation section, using a primary oscillatory system comprised of a two-DOF mass-spring-damper structure, as described in Section 2.3.

For the case of the novel dynamic design of nonlinear spring presented and mathematically analyzed in Chapter 3, a series of numerical simulations and verification experiments are conducted in the present chapter using a lab specimen comprised of the NES coupled to the PO, and altogether mounted on a shake table so it can be subjected to ground motion. This chapter contains the numerical and experimental outcomes presented in a systematic way for different levels of impulsive excitations. Comparisons of the system with the NES locked and unlocked cases, are also presented within each impulsive load case.

4.1 Primary structure model

To numerically demonstrate the effectiveness of the proposed spring as a vibration attenuator, a physics-based model of a two-DOF base structure is considered as PO, based on the small-scale structure introduced in Chapter 2, and reported in Silva et al. (2019). The mass and stiffness matrices for this model are given by:

$$\mathbf{M} = \begin{bmatrix} m_1 & 0 \\ 0 & m_2 \end{bmatrix} = \begin{bmatrix} 23 & 0 \\ 0 & 24.0 \end{bmatrix} \text{kg}; \quad \mathbf{Z} = \begin{bmatrix} k_1 + k_2 & -k_2 \\ -k_2 & k_2 \end{bmatrix} = \begin{bmatrix} 58 & -29 \\ -29 & 29 \end{bmatrix} \text{kN/m}.$$

The higher mass on the second DOF accounts for the NES mounting bracket. After solving the eigenvalue problem, the natural frequencies of the system are found to be 3.4 and 9.2 Hz, and mode shapes are given by vectors $[0.66 \quad 1]^\intercal$, and $[1 \quad -0.56]^\intercal$, for the first and second mode, respectively. The transfer function from base acceleration to each DOF acceleration is shown in Fig. 4.1.

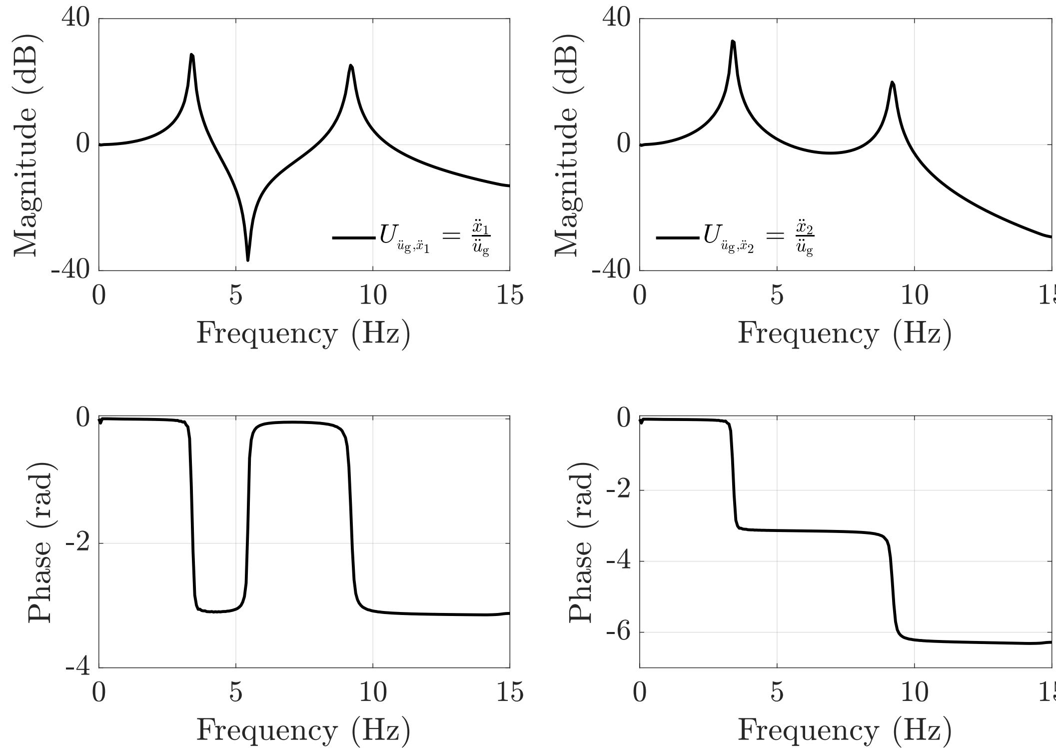

Figure 4.1. : Transfer functions from base acceleration to i-DOF acceleration.

4.2 Model of the beam-NES coupled to the primary system

The proposed nonlinear spring, which will be referred hereafter simply as beam NES is now treated as an NES attached to the second mass of a linear system as schematically shown in Fig. 4.2.

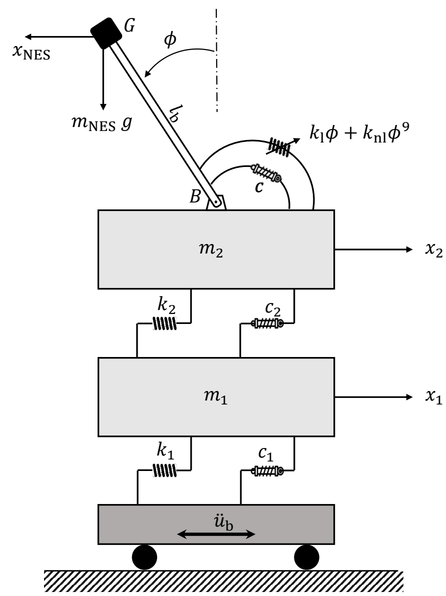

Figure 4.2. : Schematic of the beam-NES attached to a two-DOF primary oscillator.

The equations of motion of this system are derived using Lagrangian mechanics. The first step is to establish the position and velocity of the mass at the tip of the beam-NES (point G), with respect to the coupling point at the second DOF (point B). From kinematics of rigid bodies:

$$\mathbf{x}_{\text{G/B}} = \mathbf{x}_{\text{NES}} = -l_{\text{b}} \sin(\phi)\mathbf{i} + l_{\text{b}} \cos\phi \mathbf{j} + X_2 \mathbf{i}, \tag{4.1}$$

where X_2 is equivalent to the velocity of point B in the diagram, and, after taking the first derivative with respect with time, the velocity of B is given by:

$$\dot{\mathbf{x}}_{\text{NES}} = [\dot{X}_2 - \dot{\phi} l_{\text{b}} \cos(\phi)]\mathbf{i} - \dot{\phi} l_{\text{b}} \sin\phi \mathbf{j}. \tag{4.2}$$

To construct the Lagrangian, the energy quantities of the system need to be obtained, the total kinetic energy of the system is:

$$T = \tfrac{1}{2} m_1 \dot{X}_1^2 + \tfrac{1}{2} m_2 \dot{X}_2^2 + \tfrac{1}{2} m_{\text{NES}} |\dot{\mathbf{x}}_{\text{NES}}|^2 + \tfrac{1}{2} I_G \dot{\phi}^2, \tag{4.3}$$

where I_G is the rotational moment of inertia of the mass of the beam-NES with respect to the connecting point B, and the magnitude of the velocity vector of the NES is given by:

$$|\dot{\mathbf{x}}_{\text{NES}}|^2 = \dot{X}_2^2 + l_\text{b}^2\dot{\phi}^2 + 2\dot{X}_2 l_\text{b}\dot{\phi}\cos\phi, \tag{4.4}$$

and the remaining quantities are defined in Fig. 4.2. The potential energy is given by:

$$V = \tfrac{1}{2}k_1(X_1 - u_\text{b})^2 + \tfrac{1}{2}k_2(X_2 - X_1)^2 + m_{\text{NES}} g l_\text{b}\cos\phi + \tfrac{1}{2}k_\text{l} l_\text{b}^2\phi^2 + \tfrac{1}{10}k_\text{nl}^{10}\phi^{10}. \tag{4.5}$$

Here, the power of ϕ in the last term of the equation comes from the device model presented and explained in Section 3.1.1. Finally, the third element of Lagrange's formulation is to determine the non-conservative forces. The Rayleigh dissipation function is given by:

$$D = \tfrac{1}{2}c_1\dot{x}_1^2 + \tfrac{1}{2}c_2(\dot{X}_2 - \dot{X}_1)^2 + \tfrac{1}{2}c l_\text{b}^2\dot{\phi}^2. \tag{4.6}$$

The Lagrangian of the system is then $\mathcal{L} = T - V$. Applying Lagrange's equations, given by:

$$\frac{\mathrm{d}}{\mathrm{d}t}\left(\frac{\partial\mathcal{L}}{\partial\dot{X}_1}\right) - \frac{\partial\mathcal{L}}{\partial X_1} + \frac{\partial D}{\partial\dot{X}_1} = 0 \tag{4.7a}$$

$$\frac{\mathrm{d}}{\mathrm{d}t}\left(\frac{\partial\mathcal{L}}{\partial\dot{X}_2}\right) - \frac{\partial\mathcal{L}}{\partial X_2} + \frac{\partial D}{\partial\dot{X}_2} = 0 \tag{4.7b}$$

$$\frac{\mathrm{d}}{\mathrm{d}t}\left(\frac{\partial\mathcal{L}}{\partial\dot{\phi}}\right) - \frac{\partial\mathcal{L}}{\partial\phi} + \frac{\partial D}{\partial\dot{\phi}} = 0, \tag{4.7c}$$

produces the system of equations of motion of the entire 3-DOF system. Considering that the acceleration produced by taking the time-derivative of the velocities is absolute (i.e.: $\ddot{X}_1 = \ddot{x}_1 + \ddot{u}_\text{b}$, $\ddot{X}_2 = \ddot{x}_2 + \ddot{u}_\text{b}$, and so forth), the resulting EOMs of the system are given by:

$$m_1\ddot{x}_1 + c_1\dot{x}_1 + c_2(\dot{x}_1 - \dot{y}_2) + k_1 x_1 + k_2(x_1 - x_2) = -m_1\ddot{u}_\text{b} \tag{4.8a}$$

$$(m_2 + m_{\text{NES}})\ddot{x}_2 + c_2(\dot{x}_2 - \dot{y}_1) + k_2(x_2 - x_1) - m_{\text{NES}} l_\text{b}\ddot{\phi} + m_{\text{NES}} l_\text{b} x_2\dot{x}_2^2 = -(m_2 + m_{\text{NES}})\ddot{u}_\text{b} \tag{4.8b}$$

$$(I_G + m_{\text{NES}})\ddot{\phi} - m_{\text{NES}} l_\text{b}\ddot{x}_2 + c l_\text{b}^2\dot{\phi} + (k_\text{l} l_\text{b}^2 - m_{\text{NES}} g l_\text{b})\phi + k_\text{nl}^{10}\phi^9 = +m_{\text{NES}} l\ddot{u}_b. \tag{4.8c}$$

This constitutes the model of a two-DOF linear oscillator with masses m_1 and m_2, stiffness coefficients k_1 and k_2, and damping coefficients c_1 and c_2, coupled to a beam-NES of mass m_{NES}, damping coefficient c, linear component of stiffness k_{l}, and non-linear component of stiffness k_{nl}, which is of order 9.

Some interesting observations are worth mentioning here: 1) the equations of motion of the PO have the form of a classical two-DOF oscillator with mass, damping and stiffness matrices; 2) The second mass has a coupling term added to it which contains both a component related to the angular acceleration $\ddot{\phi}$, and another related with the product $x_2\dot{x}_2$, both multiplied by the length of the beam, as these quantities are generated from the beam NES moment equation of motion; 3) the equation of motion of the beam NES has a buckling term, function of the gravitational acceleration, which can produce a negative stiffness if the mass is increased excessively, turning the beam into a bi-stable element, and the coupling term with the second floor is also a function of the acceleration of such floor, completing the coupled equations of motion.

To properly analyze this system numerically, by evaluating the relative contribution of terms in Eqns. (4.8), it is convenient to express them in nondimensional form. Choosing the inverse of the first linear natural frequency $\omega_1 = \sqrt{\frac{k_1}{m_1}}$ and the length of the beam l_{b} as time and length scales, such that $\tau = \omega_1 t$, and $x_i = z_i l_{\text{b}}$, $i = 1, 2$, the resulting nondimensional equations of motion are given by:

$$z_1'' + 2\lambda_1 z_1' + \lambda_2(z_1' - z_2') + z_1 + \eta_1(z_1 - z_2) = -\frac{m_1}{k_1 l_{\text{b}}} z_{\text{b}}''(\tau) \tag{4.9a}$$

$$\mu_2 z_2'' + 2\lambda_2(z_2' - z_1') + \eta_1(z_2 - z_1) - \mu_{\text{n}} l_{\text{b}} \varphi'' + \mu_{\text{n}} l_{\text{b}}^3 \varphi(\varphi')^2 = -\frac{\mu_2}{m_1 k_1 l_{\text{b}}} u_{\text{b}}'' \tag{4.9b}$$

$$\mu_\varphi \varphi'' - \mu_{\text{n}} l_{\text{b}} z_2'' + 2\lambda_{\text{n}} l_{\text{b}}^2 \varphi' + \mu_{\text{b}} \varphi + \eta_{\text{nl}} l_{\text{b}}^{18} \varphi^9 = +\frac{m_{\text{NES}}}{k_1} u_{\text{b}}''. \tag{4.9c}$$

Here, z is the nonlinear displacement, given by where the new parameters are given by:

$$\lambda_i = \frac{c_i}{2\sqrt{m_1 k_1}}, (i = 1, 2, N) \qquad \eta_1 = \frac{k_2}{k_1}, \qquad \eta_{\mathrm{nl}} = \frac{k_{\mathrm{nl}}}{k_1},$$
$$\mu_2 = \frac{m_2 + m_{\mathrm{NES}}}{m_1}, \qquad \mu_\varphi = \frac{I_G + m_{\mathrm{NES}} l_{\mathrm{b}}^2}{m_1}, \qquad \mu_{\mathrm{buck}} = \frac{l_{\mathrm{b}}^2 k_1 - m_{\mathrm{NES}} g l_{\mathrm{b}}}{k_1},$$
$$\mu_{\mathrm{n}} = \frac{m_{\mathrm{NES}}}{m_1}.$$

Quantities λ_i are the nondimensional damping coefficients, η_i, the mass ratio from each DOF mass to the first mass, and η_i, stiffness ratios. It should be mentioned that the quantity μ_{buck} represents a buckling coupling term that introduces negative stiffness if the gravity effects dominate the motion.

4.3 Numerical simulations for impulsive initial conditions

The comprehensive procedure undertaken to execute numerical simulations of the full system are covered in this Section. A brief explanation of the selection and design of the ground excitation used to simulate impulse excitation is first provided, followed by the results.

4.3.1 Base motion selection

The system is assumed initially at rest, and is excited with an experimentally-obtained base excitation signal that produces an effect similar to an impulse excitation to the structure. The development of the technique to carry out blast simulations (equivalent to initial velocity impulses to the structure), using ground motions such as those produced by shake tables was reported by Wierschem (2014). Here, the base excitation is dependent of several parameters that need to be designed. The basic idea is that the base acceleration should generate a bounded displacement response. A sample of the shape of the ground motion that produces a valid impulse excitation to a structure is shown in Fig. 4.3. It can be observed that the signal starts at zero, then increases with a constant slope of E_{acc}, until it reaches a peak amplitude of $a_{\max}$, after which there is a short hold time of t^{+}_{hold}. Next, a linearly decreasing ramp at a slope equal in magnitude to the increasing case but with negative sign occurs until the signal reaches a minimum amplitude of $a_{\min}$, followed by a longer hold time of t^{-}_{hold}, then finally to return to zero at the same rate as before (E_{acc}).

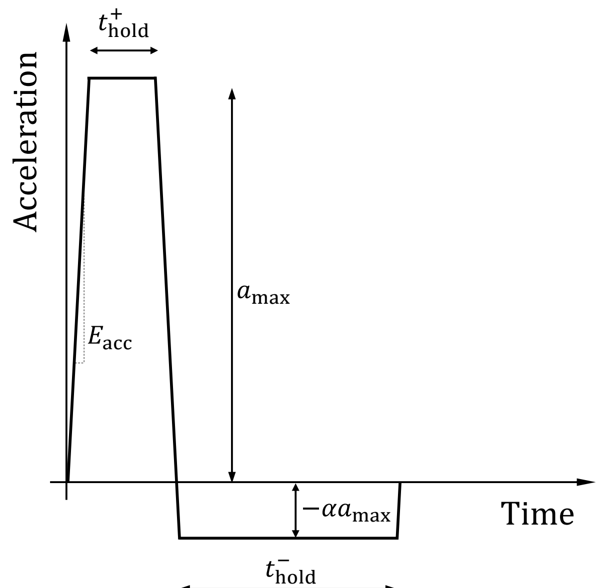

Figure 4.3. : Impulse excitation ground acceleration signal.

The designed signal is given by:

$$t^{+}_{\mathrm{hold}} = \frac{1}{\alpha E_{\mathrm{acc}}}(E_{\mathrm{acc}} t^{+}_{\mathrm{hold}} + a_{\max} - a_{\max}\alpha^{2}), \tag{4.10}$$

which in turn produces a bounded displacement, similar to a Haversine ramp with time $t^{+}_{\mathrm{hold}} + t^{-}_{\mathrm{hold}}$. An example signal with its acceleration, velocity and displacement states is shown in Fig. 4.4.

A comparison of two simulated responses of the second mass of the previously described structure, one using the synthetic base motion generated impulse, and the other using an actual initial velocity impulse, is presented in Fig. 4.5, both for acceleration and displacement. It is clear that the followed approach of using a specially

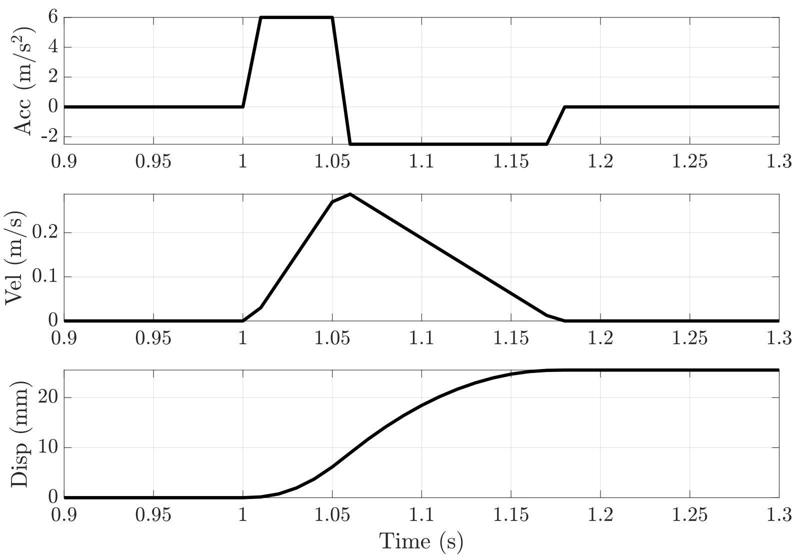

Figure 4.4. : Impulse simulation base displacement, velocity and acceleration.

designed signal in the shake table as input excitation produces similar response between the measured and the synthetic excitations.

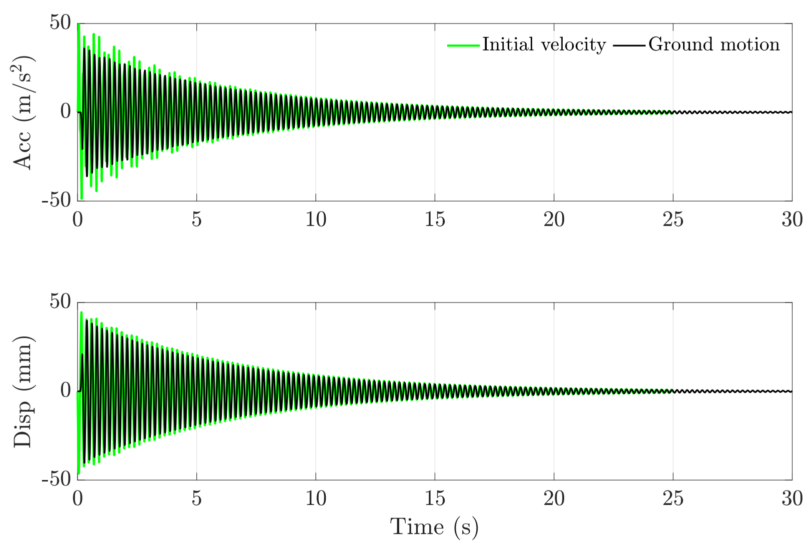

Figure 4.5. : A comparison of the acceleration and displacement responses of the second DOF of the PO, subjected to initial velocity vs. ground motion.

4.3.2 Metrics of evaluation

To study the efficacy of the NES to passively absorb and locally dissipate impulsive energy from the PO, a similar procedure as that taken in Sec. 2.2.1 is followed here. The system is simulated for the selected impulse excitations. Then, the percentage of energy dissipated in the NES is calculated, and comparisons of mechanical energy of the system with and without the NES active are shown. Lastly, the power per unit mass is calculated and plotted to verify that indeed the direction of the flow is in its majority towards the NES, and how much backflow is present.

The evaluation of the performance of the NES is done using the same metrics as those utilized in Section 2.2.1, specifically:

1. the total percentage of input energy absorbed and dissipated in the NES (quantity $\mathcal{E}_{\text{NES},\%}$ in Eq. (2.12), modified accordingly for the damping term in the proposed NES model) given by:
$$\mathcal{E}'_{\text{NES},\%} = \frac{c l_{\text{b}}^2 \int_0^{t_{\text{f}}} [\dot{\phi}(\tau)]^2 dt}{\int_0^{t_{\text{f}}} \dot{\mathbf{u}}(\tau)^{\intercal} \mathbf{M}\, \iota\, \ddot{u}_{\text{b}}(\tau) dt}; \tag{4.11}$$
2. the proportion of total mechanical energy stored in the NES during the response [quantity $\mathcal{D}(t)$ in Eq. (2.13)], also modified accordingly to take into account the 9th order model of restoring force) given by:
$$\mathcal{D}'_{\text{NES}}(t) = \frac{T'_{\text{NES}} + U'_{\text{NES}}}{T'_{\text{PO}} + U'_{\text{PO}} + T'_{\text{NES}} + U'_{\text{NES}}}, \tag{4.12}$$
where primed quantities indicate the system with the beam-NES attachment. The kinetic and potential energies of the NES are:
$$\begin{aligned} T'_{\text{NES}}(t) &= \tfrac{1}{2}[m_{\text{NES}} \dot{x}_2^2 - 2 l_{\text{b}} m_{\text{NES}} \dot{x}_2 \phi \dot{\phi} + (I_G + l_{\text{b}}^2 m_{\text{NES}}) \dot{\phi}^2] \\ U_{\text{NES}}(t) &= \tfrac{1}{2} k_{\text{L}} l_{\text{b}}^2 \phi^2 + \tfrac{1}{10} k_{\text{NL}} l_{\text{b}}^{10} \theta^{10}; \end{aligned} \tag{4.13}$$
3. the power per unit mass of the system for determining the level of backflow introduced into the damping effect produced by the NES [quantity $\mathcal{P}'(t)/m_{\text{tot}}$ in Eq. (2.15)], also modified accordingly for the case of a 9th order restoring force). Notice the prime symbol added to the variables to differentiate them from the wire NES case.

4.3.3 Numerical setup preliminaries

The model was constructed using Simulink within the MATLAB environment. Three input/output blocks, corresponding to each DOF were generated, such that the coupling terms interconnect accordingly. A representative block diagram of the model is shown in Fig. 4.6. Inside each block, the corresponding EOM is integrated and interconnected to the other DOFs, forming a single subsystem, and outside this subsystem, the main block is interconnected with the input excitation block and the simulation results block. The Simulink block diagram as well as the MATLAB code are included in the Appendix Section.

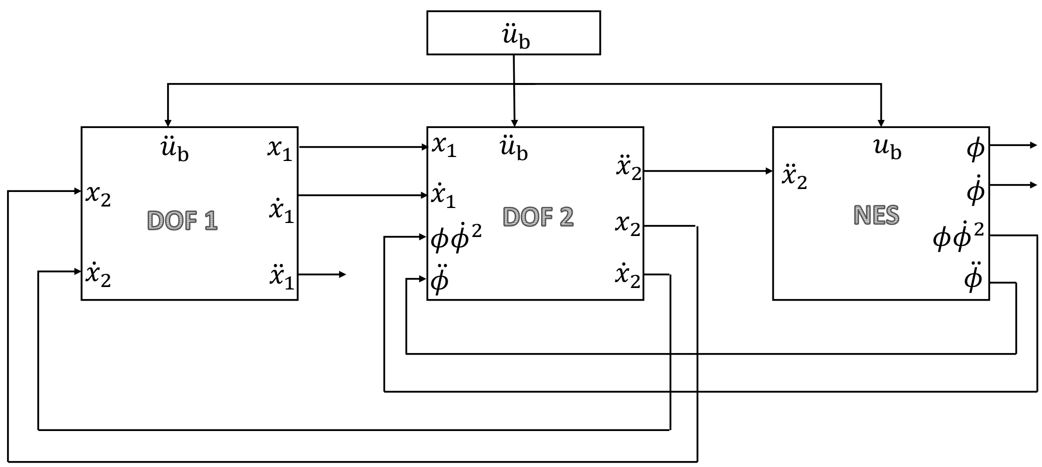

Figure 4.6. : I/O diagram of the Simulink model blocks for the system.

The parameters selected for running this series of simulations were chosen from several sources, as the simulations include a comprehensive model of the PO, coupled to the NES at its second DOF.

1. Physical parameters of the PO. These were already defined in Section. 4.1.

2. Physical parameters of the NES. Some of the physical parameters of the beam-NES were already defined in Section 3.2.1, for both surface degrees: $n = 3$, and

$n = 5$. However, to demonstrate the self-tuning capacity of the device, and for it to work properly with a structure of the characteristics of the PO, some changes to the NES parameters are introduced: i) the mass has been increased to 0.4 kg, to have a mass ratio of approximately 1 % of the total structural mass, which is common in these types of devices; ii) the damping of the device has also been significantly increased, as it is a necessary characteristic for the device to passively absorb and locally dissipate the energy transferred from the PO. If the damping in the NES is too low, the energy gets redirected to the PO due to the high reciprocity of the NES. This increment in damping is implemented experimentally by adding a layer of a high damping polymer film between two thinner beams to obtain an equivalent-thickness beam with higher damping characteristics than the original (see Fig. 4.7)

3. Simulation parameters. The simulations are carried out in Simulink, with the following configuration and constants: a fixed time step size reciprocal to 1024 Hz, with a Runge-Kutta ODE4-type solver, suitable for general cases, simulation times of 45 s, for the case of impulsive excitations, and an unconstrained periodic sample time. Unit delay blocks were placed accordingly throughout the model to avoid algebraic loops.

4.3.4 Experimental setup preliminaries

Experimental implementation of the designed NES is applied as a validation step of the NES as an attenuation device for a linear base structure, following the numerical results presented in the previous Section. A series of experiments with the full base + NES system are conducted in the Intelligent Infrastructure Systems Lab at Purdue University, using a hydraulic shake table and comparing the two responses of the PO (i.e., with and without NES).

The experimental setup is a 2DOF system with the NES attached on the top floor as shown in Figs. 4.8. To perform this experiment, a six-DOF hydraulic shake

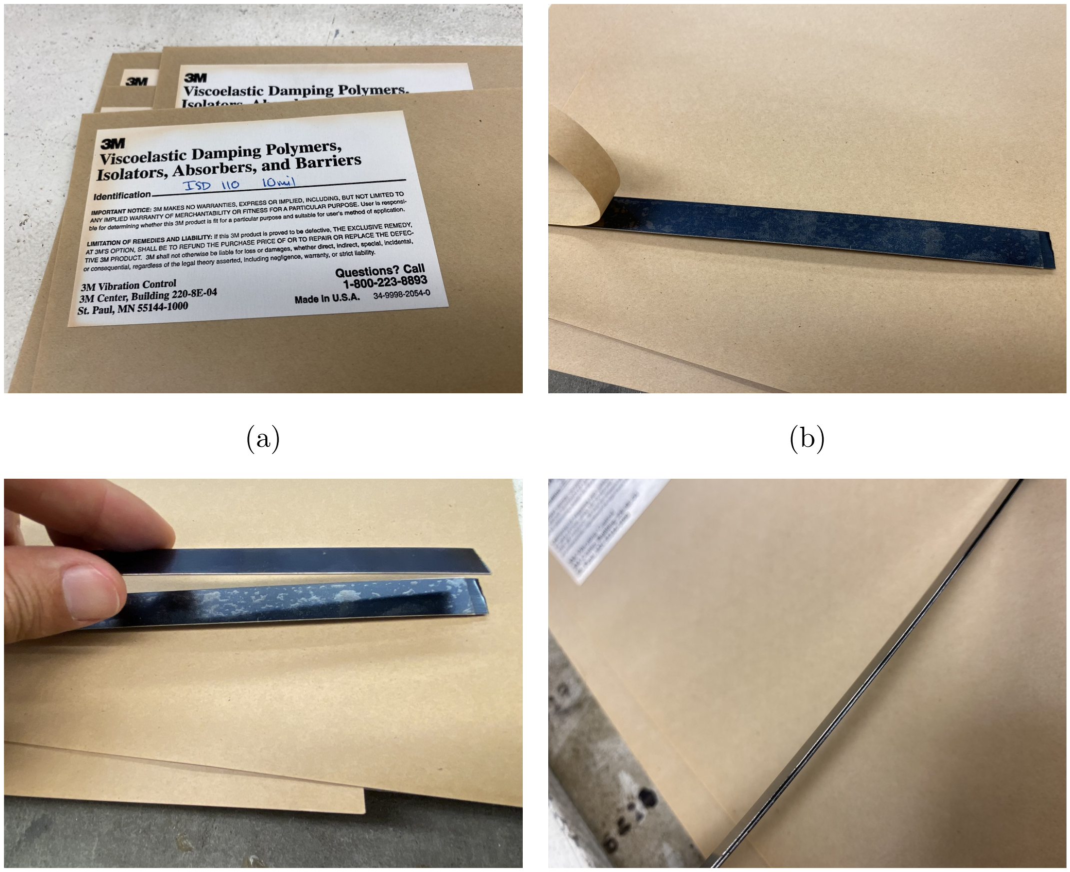

(a) (b)

(c) (d)

Figure 4.7. : Experimental procedure for increasing the damping in the beam NES a) cutting damping film to beam dimension; b) sticking material in base beam; 3) pressing two beams together with film in between; 4) resulting composite damped beam.

table with an internal PID hydraulic controller, model SC6000, manufactured by Shore Western is used. Four ceramic capacitive accelerometers, model 333B40, manufactured by PCB are used for measuring the accelerations of the system, with a frequency range of 0.5 - 3000 Hz, measurement range of $\pm$ 98 $\mathrm{m/s^2}$, and a broadband resolution of 0.0005 $\mathrm{m/s^2}$, using ICP® excitation. Each accelerometer is fixed to each DOF with a magnetic base (including one on the shake table), except in the case of the NES mass, where this accelerometer is glued due to the small area of the mass. The base displacement generated by the shake table is measured using a linear variable differential transformer (LVDT) located internally in the hydraulic actuator. A built-in function generator in the shake table controller provides the capacity to generate custom excitation signals. Data is acquired using an analog, eight-channel input, 18-bit precision data acquisition box, model VibPilot-8 manufactured by m+p International, with built-in anti-aliasing filter and sampling time capacity of up to 204 kHz (for this experiment, data is sampled at 256 Hz).

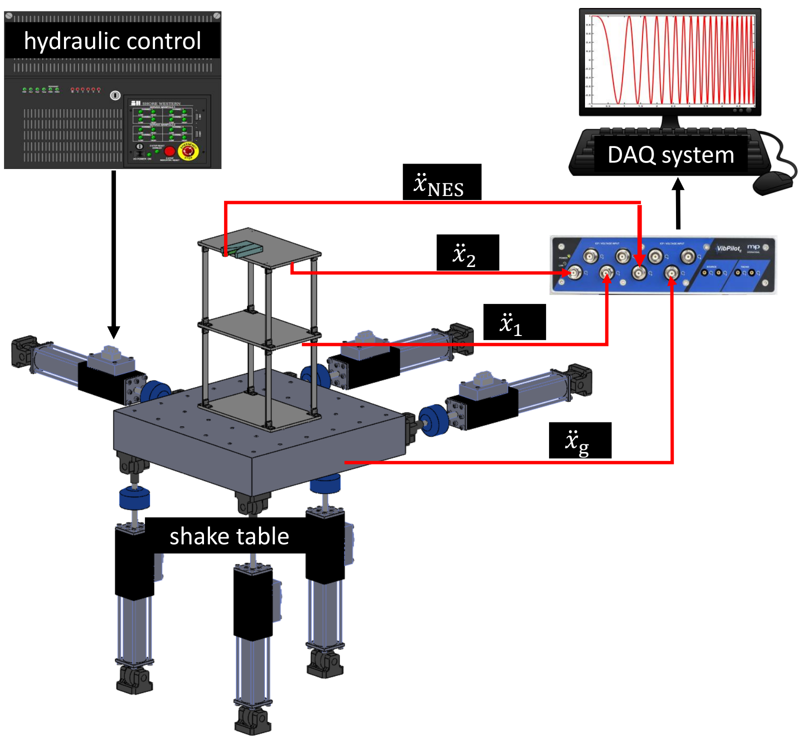

Figure 4.8. : Experimental setup for model verification and response comparison.

The selected cases of study, corresponding to low, moderate and high levels of excitation after the NES activation threshold has been surpassed, are detailed in Table. 4.1. Here, the displacement column refers to the physical displacement that the shake table imposes to the structure at the base, t_{hold} is the duration of the ramp, and equivalent v_0 corresponds to the initial velocity, if the system were excited with an impulse of equal magnitude on both masses.

Table 4.1. : Numerical and experimental cases of study.

Case number	**Displacement** (mm)	t_{hold} (s)	**Equivalent** v_0 (m/s)	**Curvature order**
1	30	0.3	0.21	3
2	40	0.3	0.28	3
3	50	0.3	0.33	3
4	30	0.3	0.21	5
5	40	0.3	0.28	5
6	50	0.3	0.33	5

4.4 Simulated and experimental results

The results and discussion of the computational simulations and further experimental observations are presented in this Section, first with the cases corresponding to boundary surface order 3, and then with those of surface order 5.

4.4.1 Case 1

Figure 4.9 contains the acceleration time histories of the NES (top plot, red line), and of both DOFs of the PO (middle: 2nd DOF; bottom: 1st DOF), when the NES is locked (green thick line) and unlocked (black thin line). Here, Fig. 4.9(a) corresponds

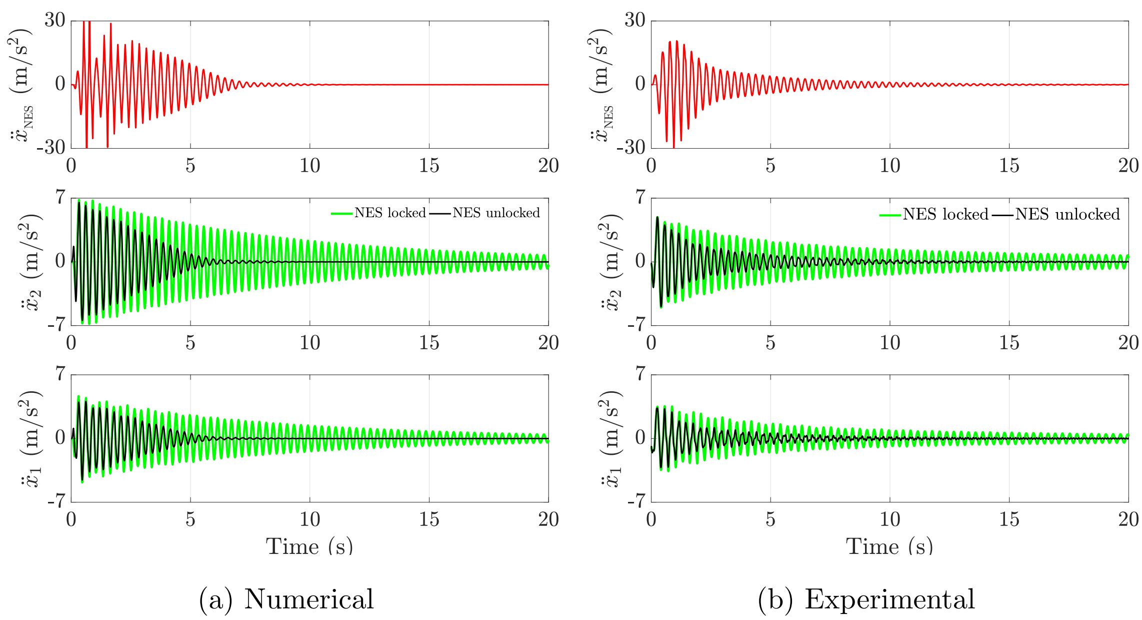

Figure 4.9. : Acceleration time responses of all of the DOFs (Case 1).

to the case of the numerical simulation, and Fig. 4.9(b), to the case of the experimental measurement. Acceptable agreement is observed between numerical simulations and experiments, both in the case of the NES and that of the PO. A significant reduction in response of the two DOFs of the PO is also observed, the response decay to near to near zero, when the NES is active, occurs before 5 s in the simulated case and at approximately 8 s in the experimental case.

Despite the low excitation level it is observed that the NES engages in resonance capture fairly quickly, contributing to a response reduction of the whole structure. Another interesting observation is that both DOFs of the structure experience response reduction due to the effect of the NES, suggesting that high energetic activity occurs on both modes of vibration. These results show that though the excitation level is in the low range, the NES is very effective at passively extracting and locally dissipating energy from the PO as a result of its nonlinear characteristics.

Further demonstration of the capacity of the NES in engaging in energy transfer with the PO are presented in a series of plots shown in Fig. 4.10. The top-left plot represents the instantaneous percentage of energy dissipated by the beam-NES in proportion to the total initial energy. The device engages in TET with the PO becoming an active NES at the beginning of the oscillatory response, reaching a peak of maximum dissipation at about 8 s, where the NES dissipates nearly 100 % of the total impulsive energy for a short time, and decaying afterwards as the response has reached to near zero levels. The top-right plot represents the total mechanical energy of the PO for both NES active, and NES inactive cases. A significant reduction in energy is observed for the case when the NES is unlocked and active with respect to the original configuration. The third plot (bottom) shows a comparison of the instantaneous power per unit mass of the system for the same two scenarios (NES locked and unlocked). Interestingly, most of the activity when the NES is active is dissipative, as very little backflow of energy can be observed after the initial impulse (at around 1 s, where the NES acts as an ideal passive damper).

The dynamic interactions of the NES and PO in regards to their instantaneous frequency bandwidths are analyzed next through the wavelet spectra representations. Only the experimental wavelet spectra plots are presented here, as the simulation plots are rather similar. The wavelet spectra comparisons corresponding to the PO with the NES locked, and unlocked are shown in Fig. 4.11, where Fig.4.11(a), shows the

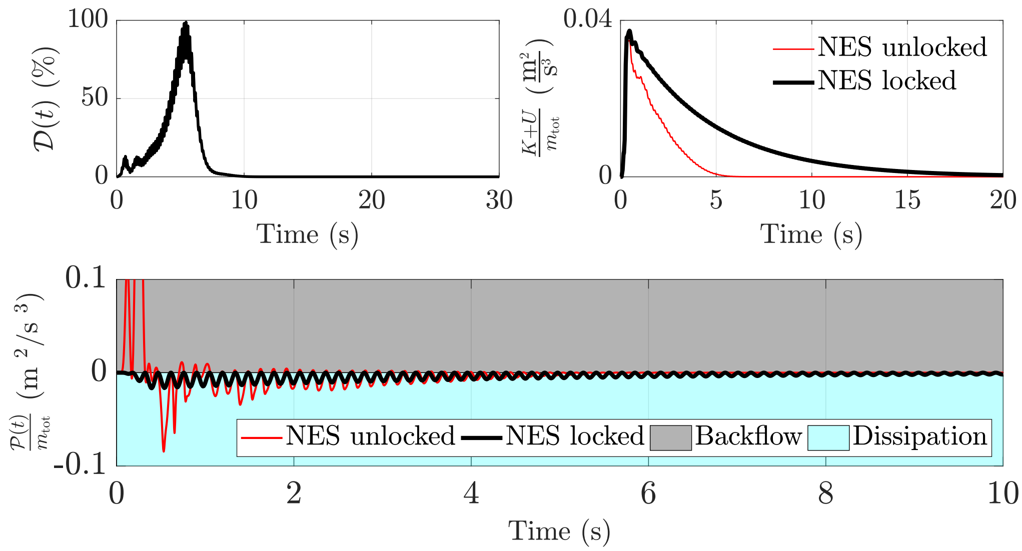

Figure 4.10. : Energy and power flow comparisons (Case1).

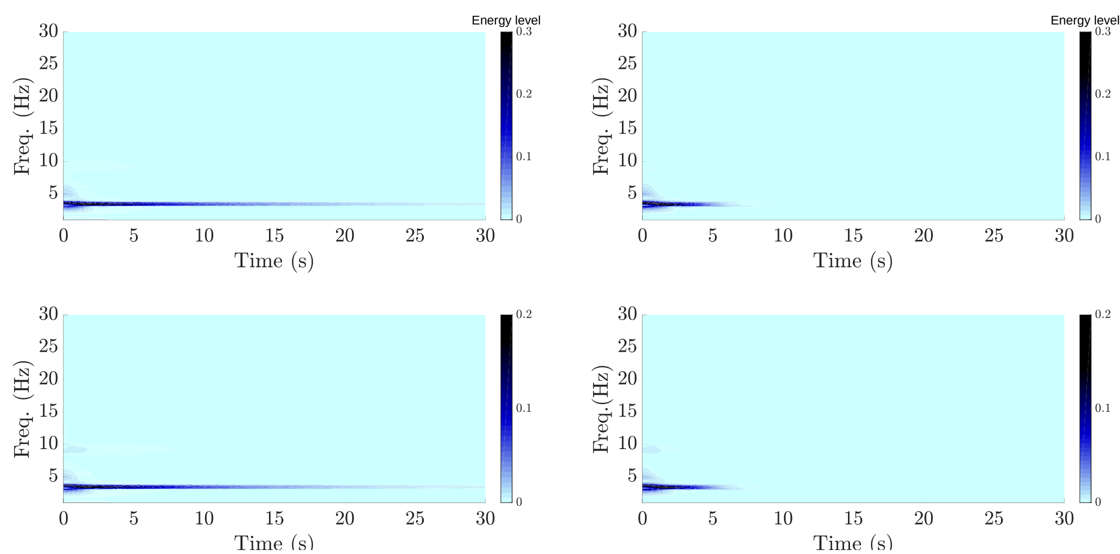

Figure 4.11. : Wavelet spectra of the PO velocity (Case 1). (a) PO with NES locked (bottom: 1st DOF, top: 2nd DOF); (b) PO with NES unlocked.

frequency content of the structure when the NES is inactive (locked), and Fig. 4.11(b) shows the frequency content when the NES is active (unlocked). A clear reduction in the energy of the system is apparent by looking at the frequency line reducing its occurrence from 20 s to around 10 s.

At the same time, high frequency activity can be noticed in the NES wavelet spectra shown in Fig 4.12. Here, a small region of bandwidth starts to appear from 4 to 12 Hz. This suggests, as expected, that the NES has the nonlinear characteristics that allow it to engage in TET through resonance capture with the host structure. Moreover, it can also be observed that the frequency bandwidth of the device is not concentrated around a single frequency, but dispersed from low to high frequency values, though the energy levels for the higher frequencies is low, this behavior is consistent with the modeled and experimental results of the NES characterization presented in Chapter 2.

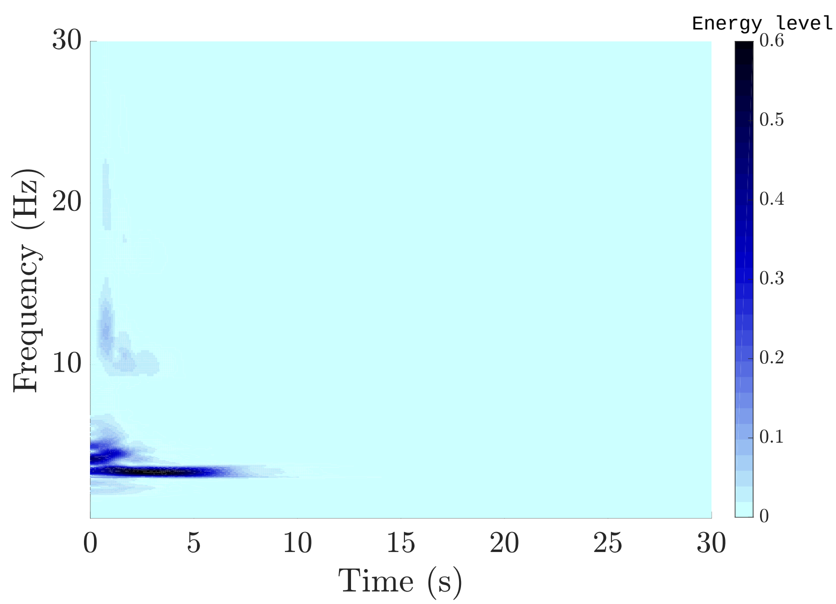

Figure 4.12. : Wavelet spectra of NES velocity (Case 1).

4.4.2 Case 2

The second case in the first series of computational simulations and experimental measurements, for the lower surface surface order, is associated with a moderate level of impulsive energy (Case 2 in Table 4.1), which produces the time responses shown in Fig. 4.13(a), for simulations, and Fig. 4.13(b), for experimental measurements.

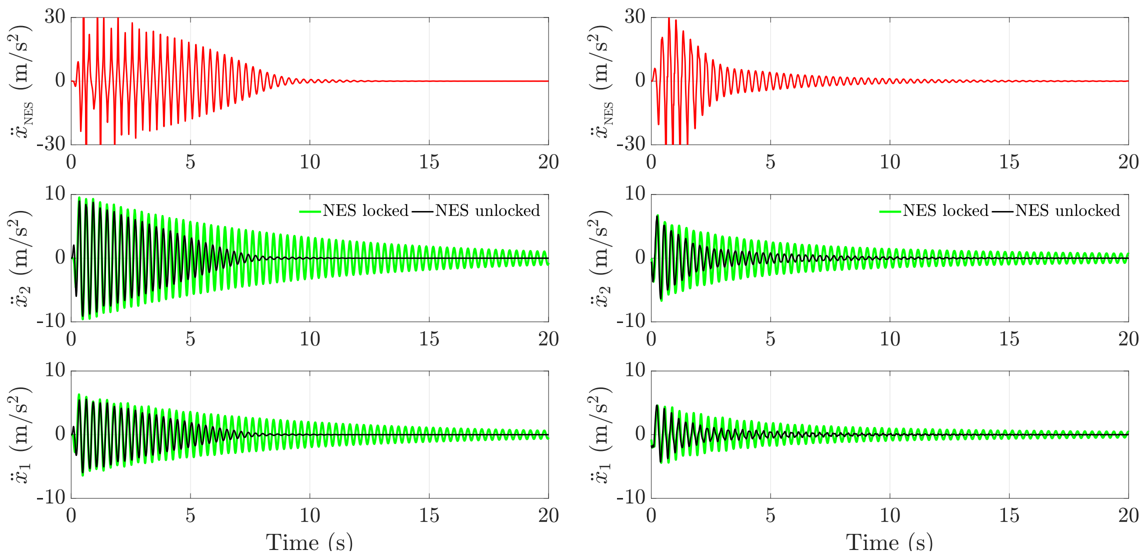

(a) Numerical (b) Experimental

Figure 4.13. : Acceleration time responses of all of the DOFs (Case 2).

A slight difference in decay response between the experimental and numerical cases can be observed. This may be likely caused by differences in the damping values used in the simulations versus the real damping present in the experiments, but also due to the unmodeled dynamics mentioned earlier. The acceleration responses agree reasonably well, both in amplitude and energy reduction behavior. In this case, the decay is slightly longer than the previous, but starting from a higher initial amplitude, therefore, maintaining the NES special damping characteristics for a larger amplitude of excitation.

The power and energy comparisons are shown in Fig. 4.14. The percentage of dissipative energy plot (top left) shows a small shift in the occurrence of the maximum dissipation peak to around 8 s. The results are very similar to those presented in Case 1, with a logical increment in the maximum values of total energy per unit mass with a slower decay in energy content. The device remains an essentially dissipative unit contributing to the reduction of oscillatory motion from the host structure, as can be seen in the power per unit mass diagram (bottom) where the backflow is still low, with some small amount at the beginning of the response after the initial impulse.

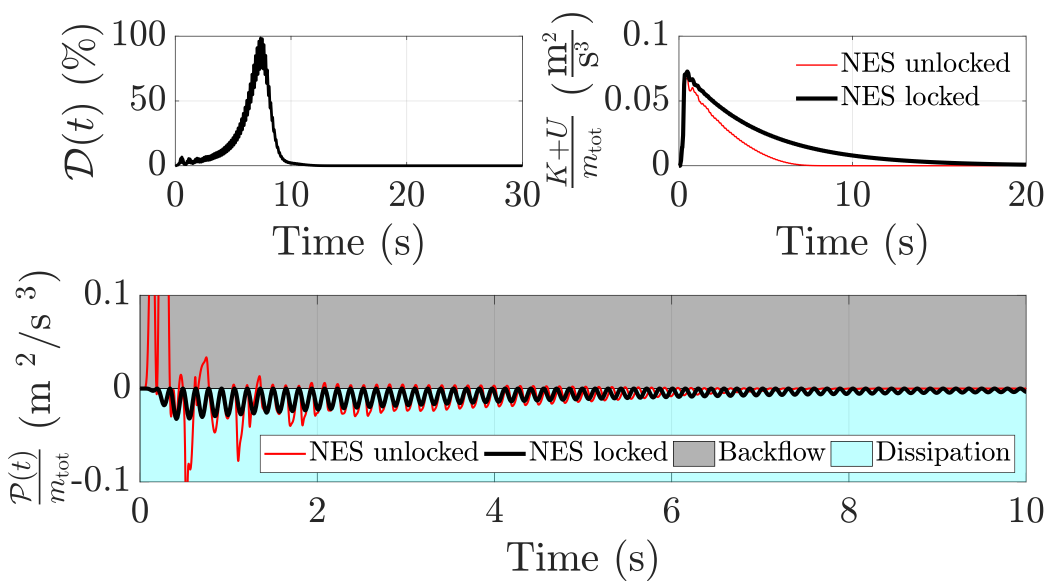

Figure 4.14. : Energy and power flow comparisons (Case 2).

For this second case, the wavelet spectra of the velocity histories of the PO, for the instances where the NES is unlocked and locked, are shown in Fig. 4.15(a) and Fig. 4.15(b), respectively. The reduction of energy from the first and second DOFs is faster than in Case 1, because the overall energy content in this case is higher, as can be observed by looking at the energy level bars of both cases. Here, the energy level reduces from approximately 0.15 to 0, occurring at nearly 10 s, and fading afterwards, in comparison to the similar case in Fig. 4.11(b), where at the same instant in time, the energy level reduction occurs from from approximately 0.1 to 0, which constitutes a decay of higher levels of energy in the same time (i.e.: faster reduction).

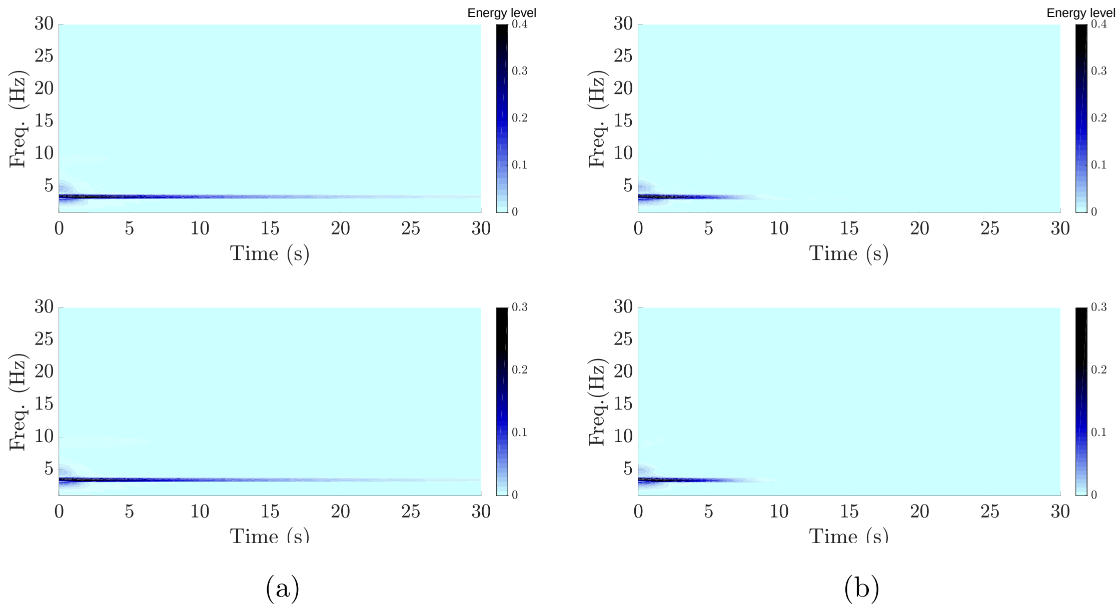

Figure 4.15. : Wavelet spectra of the PO velocity (Case 2). (a) PO with NES locked (bottom: 1st DOF, top: 2nd DOF); (b) PO with NES unlocked.

The wavelet spectra of the NES, is shown in Fig.4.16. The expected increment in broadband is evident from Case 1, as more regions of high-frequency activity, in the form of shaded stripes appear in the diagram, with frequency contents up to 30 Hz. This demonstrates the amplitude dependence and frequency broadband characteristics of this class of NES.

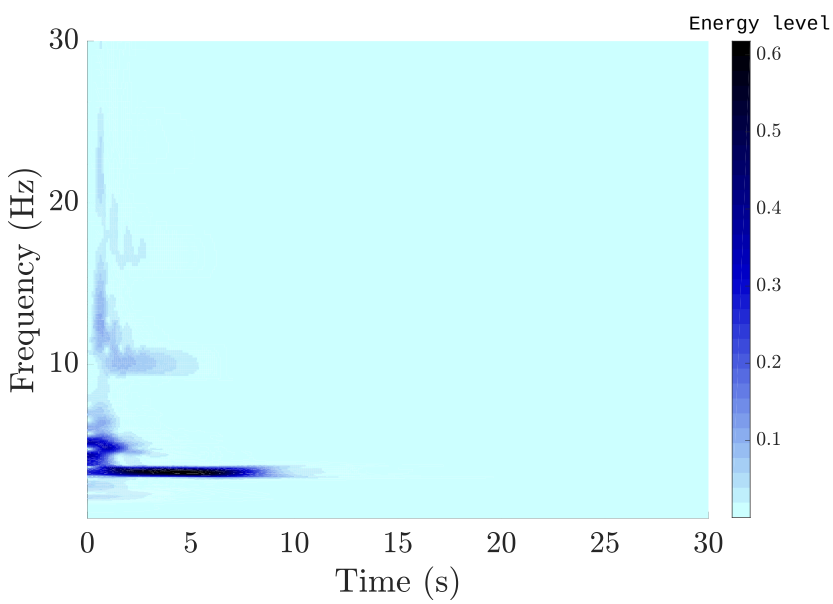

Figure 4.16. : Wavelet spectra of NES velocity (Case 2).

4.4.3 Case 3.

The final case corresponding to an amplitude of excitation associated to a high level of impulsive energy (Case 3 in Table 4.1), for surface order 3 is now analyzed. The acceleration time histories of this case are shown in Fig. 4.9(a), for the numerical simulation case, and in Fig. 4.9(b), for the measured response case.

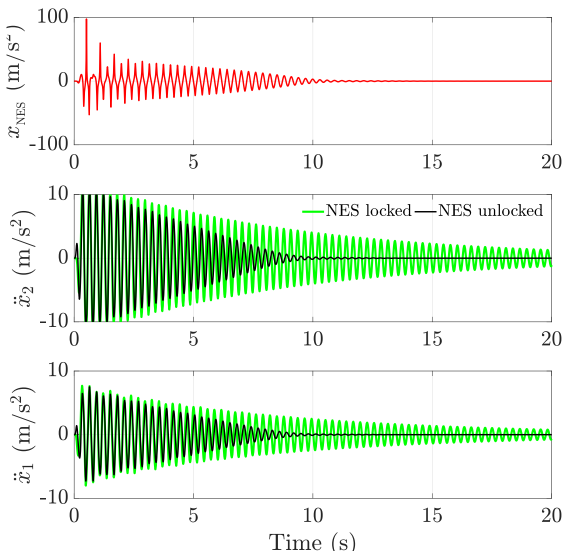

(a) Numerical

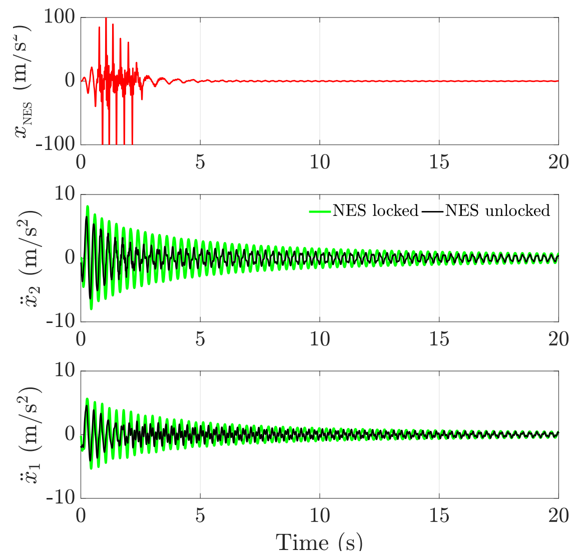

(b) Experimental

Figure 4.17. : Acceleration time responses of all of the DOFs (Case 3).

This is an extreme case of impulsive excitation. The NES acceleration history show very high peak amplitudes of acceleration. The acceleration of the beam-NES can be exacerbated by the fact that the mass tends to impact the edges of the boundaries at high amplitudes of oscillation. The responses of the 1st and 2nd DOFs of the PO show a decay rate comparable with the previous case (Case 2), reaching a near-zero response after about 9 s, only a second later than the previous case, but here with a higher amplitude of impulsive excitation. The characteristic hardening behavior of the spring can be clearly noticed in Fig. 4.17(a) (top plot).

The percentage of dissipative energy, shown in Fig. 4.18 shows an even longer shift of peak occurrence to almost 10 s, where the percentage of energy dissipated reaches its maximum. Higher initial amplitude in the mechanical energy of the system is observed (top right), as expected as this is a higher impulsive excitation case. Moreover, despite the higher initial energy content, the device manages to maintain its dissipative characteristics throughout the oscillatory motion. Very small regions of backflow are observed, again at the beginning of the excitation. The high damping material introduced to the system contributes to keep the energy within the NES and locally dissipate it more efficiently.

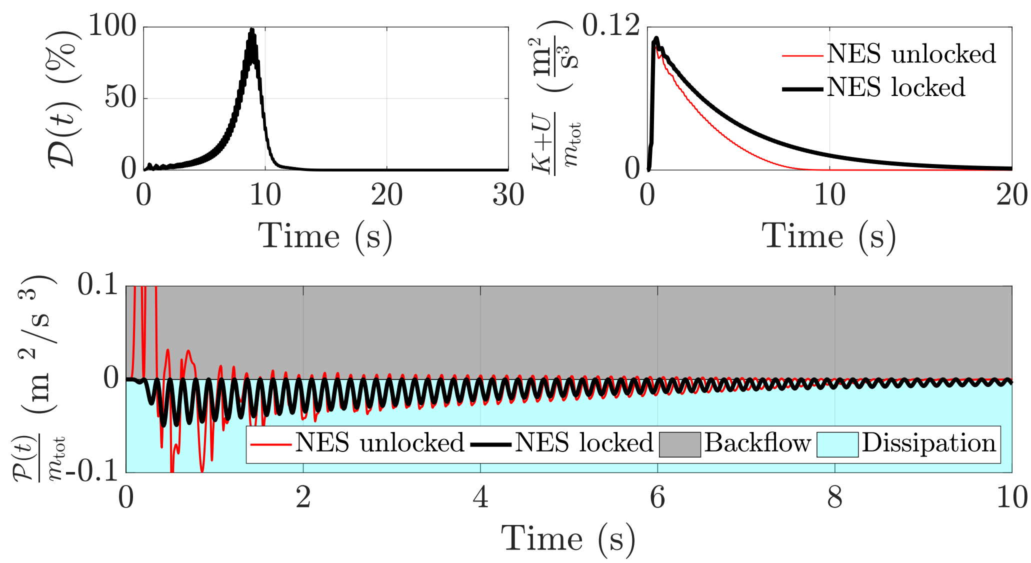

Figure 4.18. : Energy and power flow comparisons (Case 3).

The wavelet spectra of the PO corresponding to this case are presented in Fig. 4.19, and show some interest insights: the decay in acceleration response coincides with the reduction in frequency content when comparing the PO with the NES locked and unlocked cases (Fig. 4.19(a) and Fig. 4.19(b)). A significant reduction in modal response can be seen in the NES unlocked spectra plot, with the addition of increased activity in the second mode (9 Hz), which suggests that the NES effectively modified the frequency content of the PO to contribute towards nonlinear energy dissipation.

Additionally, a comparable rate of energy decay, with respect to Case 2 can be observed at instant $t = 10\,\mathrm{s}$ where the energy level reduced from approximately 0.15 to 0. However, since the overall energy content of this case is higher, the logical explanation is that this case is slightly faster in energy reduction rate than that of Case 2.

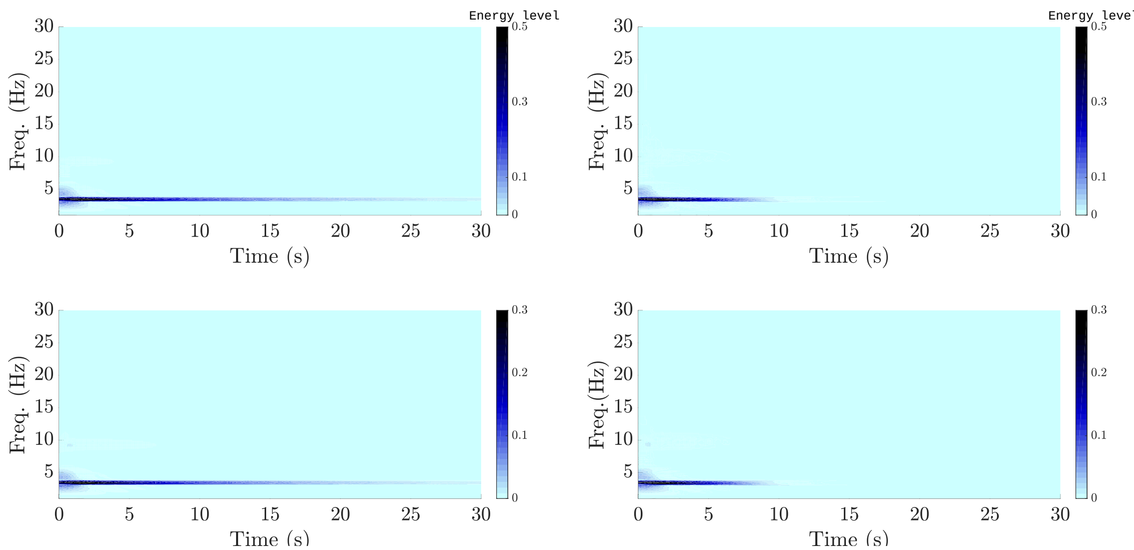

(a) (b)

Figure 4.19. : Wavelet spectra of the PO velocity (Case 3). (a) PO with NES locked (bottom: 1st DOF, top: 2nd DOF); (b) PO with NES unlocked.

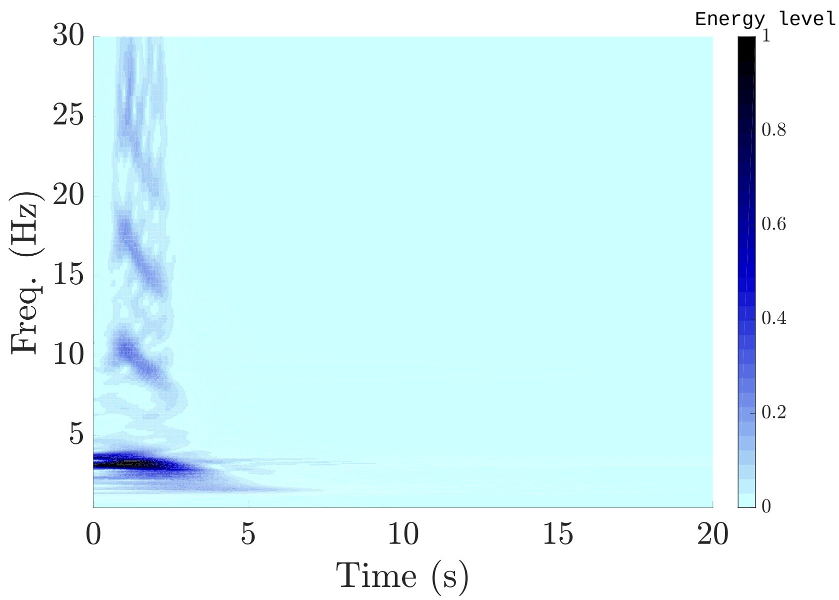

Figure 4.20. : Wavelet spectra of NES velocity (Case 3).

Furthermore, the wavelet spectra of the NES alone is shown in Fig. 4.20. The broadband energetic activity of the device is shown as dark-shaded regions of frequency exchange from lower to higher frequencies, reaching up and beyond 30 Hz, and the linear natural frequency of the device appearing very dispersed without a clear constant value, consistent with the behavior of a hardening nonlinear spring, acting as an NES.

4.4.4 Case 4.

A similar approach as that taken for the surface order 3 case is taken at this juncture. Three different levels of impulsive energy are simulated and experimentally tested, and the results are presented and commented upon accordingly. For the low energy case, the acceleration time histories of both DOFs and the NES are shown in Fig. 4.21(a) and Fig. 4.21(b). Here, the peak acceleration reached by the NES is significantly larger than the case surface order $n = 3$, but at the same time, the decay rate is faster, occurring nearly 2 s earlier than in the comparable Case 1. Thus, suggesting that a higher surface surface order offers faster damping capabilities.

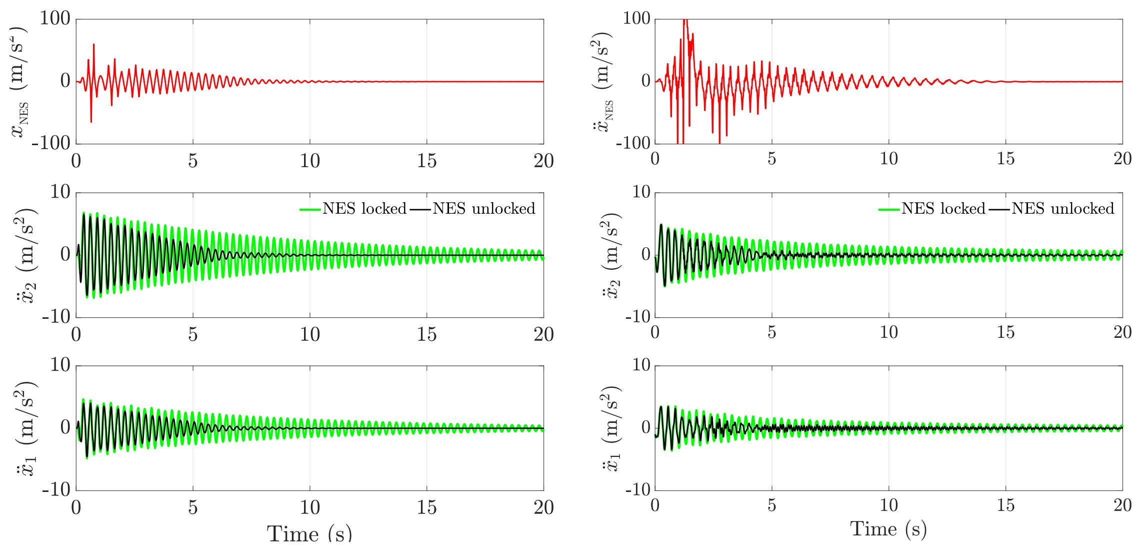

(a) Numerical (b) Experimental

Figure 4.21. : Acceleration time responses of all of the DOFs (Case 4).

The NES engages in resonance capture with the PO at early stages of the response, reaching a peak in efficiency at around 8 s, as can be seen in Fig. 4.22 (top-left). The decay in energy content per unit mass of the structure is comparable to that of Case 1 as well. The power per unit mass content of the system shows some backflow throughout the response, particularly between 2 and 4 s, when compared to the $n = 3$

case. These results confirm that different surface order cases offer unique dissipation characteristics, and that a trade off between several parameters need to be carefully designed to achieve an optimal dissipation device. Nonetheless, these results are reasonably acceptable for a passive damper.

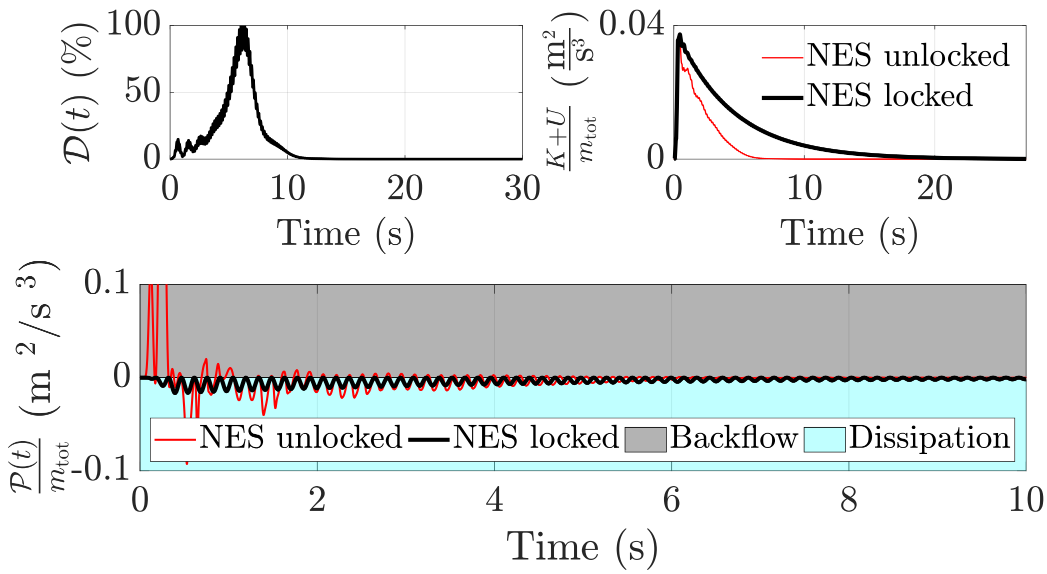

Figure 4.22. : Energy and power flow comparisons (Case 4).

The non stationary frequency evolution present in this system, can be viewed in the wavelet spectra plots, presented in Fig.4.23. Let's focus on the one corresponding to the NES (Fig. 4.24). When compared to the same amplitude in the previous surface order case, it can be observed that this case has much more energetic activity, as stripes of frequency bandwidth appear much wider in the time and higher in frequency axes, with a higher level of maximum energy present as indicated by the colorbar placed to the right of the plot. This is consistent with the theory developed in Chapter 2 that a higher surface order offers a higher hardening nonlinear spring.

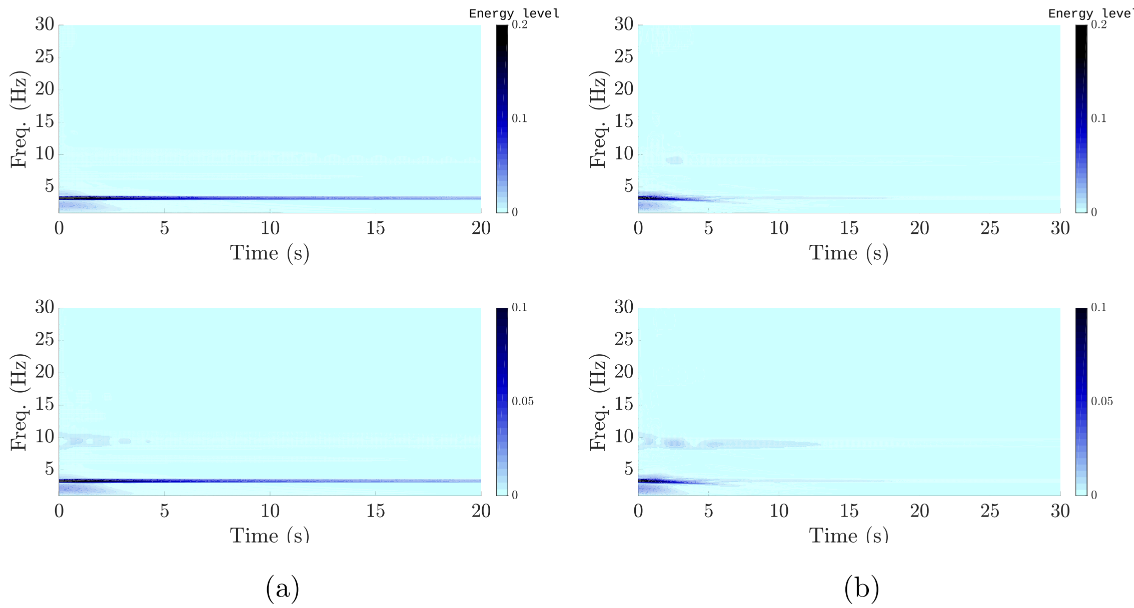

Figure 4.23. : Wavelet spectra plots (Case 4). (a) PO with NES locked (bottom: 1st DOF, top: 2nd DOF); (b) PO with NES unlocked.

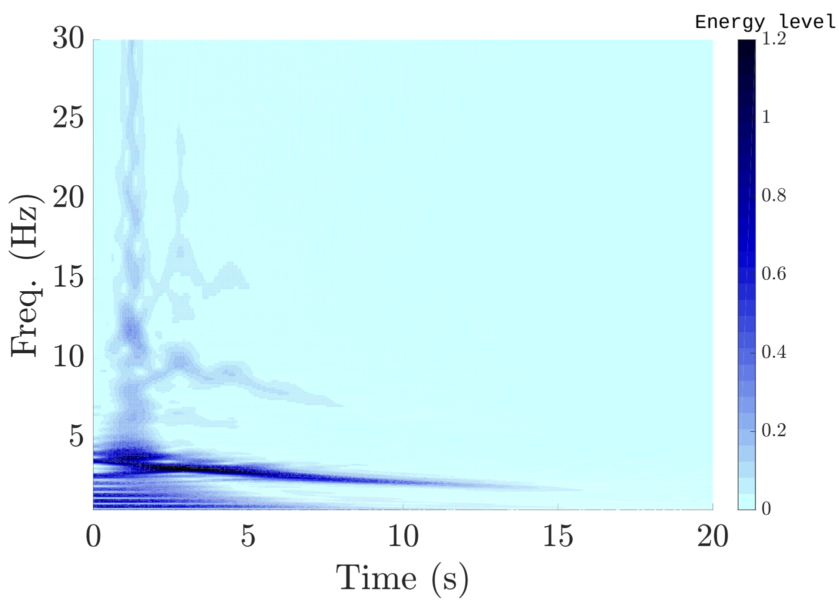

Figure 4.24. : Wavelet spectra of NES velocity (Case 4).

4.4.5 Case 5

The second set of result plots for surface order 5, corresponding to a moderate impulsive energy level (Case 5 in Table 4.1) is presented here. The acceleration time histories of the DOFs of the system are shown in Fig. 4.25(a), and Fig. 4.25(b), for the numerical and experimental cases, respectively.

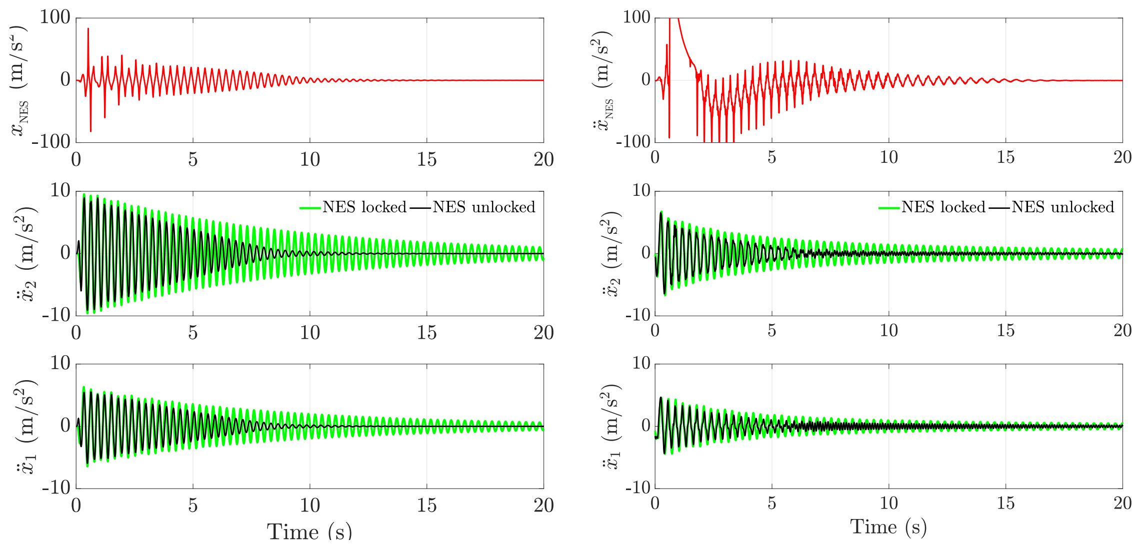

(a) Numerical (b) Experimental

Figure 4.25. : Acceleration time responses of all of the DOFs (Case 5).

The shape of the acceleration on the measured response saturated during the experiments as the mass impacts the edge of the surface. Nonetheless, after this impact occurrence, the response shows agreement with that of the numerical simulations. The decay in response observed is slower than Case 4, reaching a near-zero oscillation level at about 9 s. It should be reiterated that this case corresponds to a higher impulsive excitation level, thus the difference in decay rate.

Following a similar trend as in Cases 1-3, the percentage of dissipative energy present in the NES shown in Fig. 4.26 (top left) has shifted its maximum peak occurrence to around 9 Hz, achieving full dissipation afterwards, which is consistent with

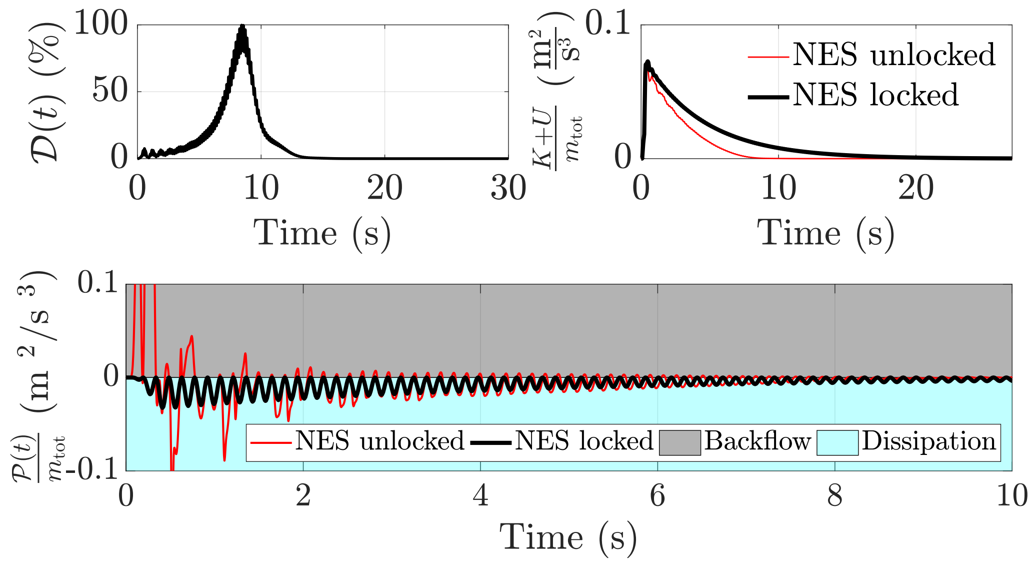

Figure 4.26. : Energy and power flow comparisons (Case 5).

the slower decay rate. The instantaneous energy and power per unit mass (top right and bottom plots) show larger levels of instantaneous dissipation and backflow, as expected for a larger amplitude of excitation case.

The experimental wavelet transform spectra of the velocity of the PO, shown in Fig. 4.27, presents an interesting observation: the significant decay in response reflected in the spectra of the PO with the NES unlocked (Fig. 4.27(b)) with increasing activity in the second mode, suggesting a transfer of energy from lower to higher modes of the structure, as expected to happen when a NES is in use.

Additionally, the NES spectra plot presented in Fig. 4.28 shows prolonged high frequency dark stripes throughout the main portion of the response duration in the NES spectra. This demonstrates the capacity of the NES to engage in harmonic resonance capture and to effectively transfer the energy of the host structure from its lower to its higher modes, thus reducing excessive vibratory motion. Moreover, much higher NES activity in its broadband frequency can be concluded by looking at the energy level in the colorbar located to the right of the plot, when compared with the $n = 3$ counterpart case.

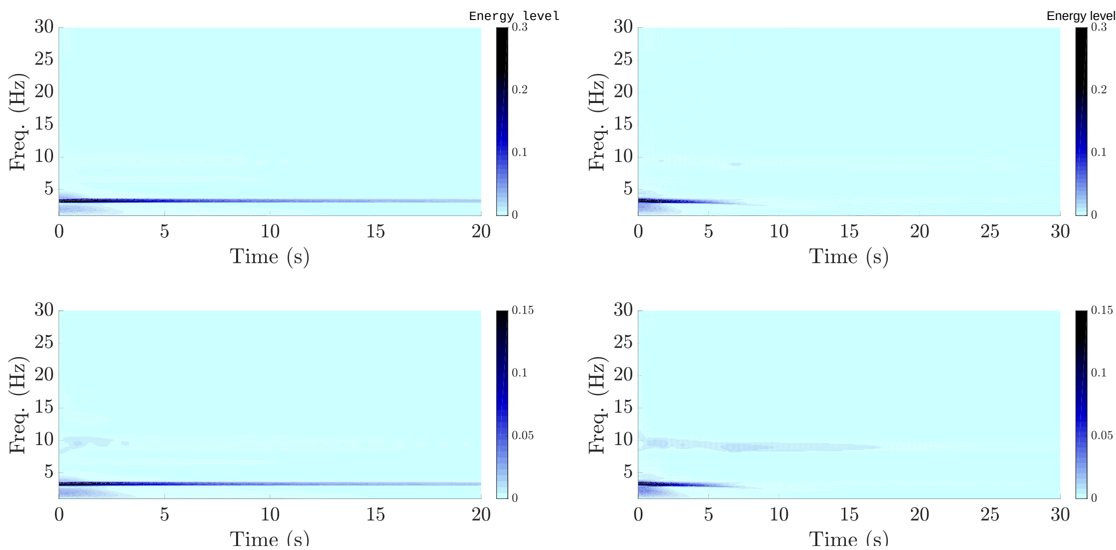

(a) (b)

Figure 4.27. : Wavelet spectra plots (Case 5). (a) PO with NES locked (bottom: 1st DOF, top: 2nd DOF); (b) PO with NES unlocked.

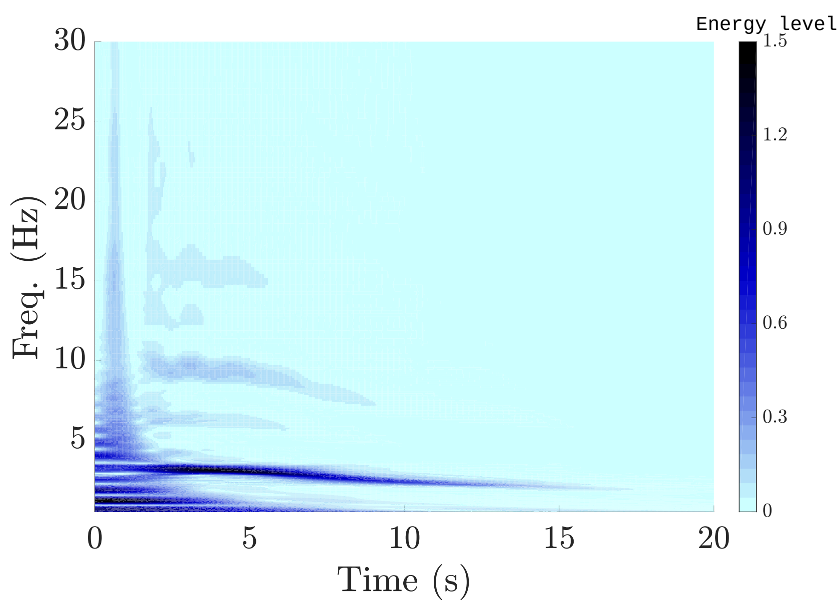

Figure 4.28. : Wavelet spectra of NES velocity (Case 5).

4.4.6 Case 6

The final result in these series of results corresponds to the case of high impulsive energy. The time responses of the accelerations are shown in Fig. 4.29.

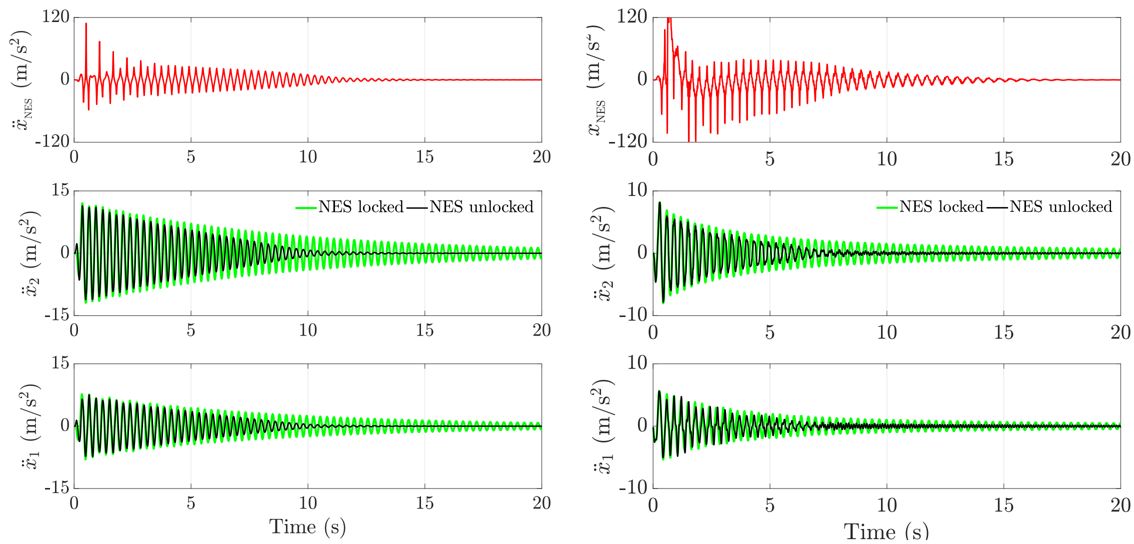

(a) Numerical (b) Experimental

Figure 4.29. : Acceleration time responses of all of the DOFs (Case 6).

In the plots corresponding to the NES responses, both representations show reasonable agreement in amplitude, and length of resonance capture activity, despite the impact peak present in the experimental plot (Fig. 4.29(b)). The decay responses of the structure with the NES unlocked also agree in length and occurrence of near-zero response, at about 10 s, for both cases. The model and experiments show a remarkable agreement which confirms the correct approach followed when developing the inverted pendulum model to predict the behavior of the beam NES. The energy and power interactions of this impulsive case are presented in Fig. 4.30. The trend of the percentage of dissipative energy of the NES shifting to the right for higher amplitudes is maintained here, as the peak occurs at 10 s, after which the near-zero response is achieved. The bottom plot of power per unit structural mass shows a

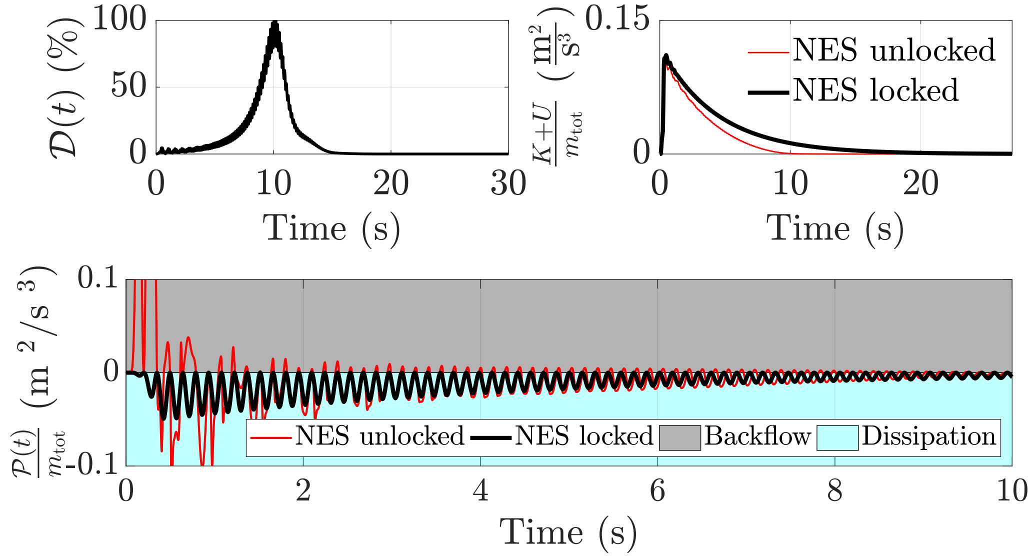

Figure 4.30. : Energy and power flow comparisons (Case 6).

much higher amplitude instantaneous power response, with its majority occurring in the dissipation region with very small backflow regions after the initial impulse. The combination of mass and damping chosen for this series of simulations/experiments have provided an effective NES.

The wavelet spectra representations of the PO velocity, presented in Fig. 4.31 a reduction of energy content in lower modes of the PO after the activation of the NES (Fig. 4.31(b)). A total decay in energetic activity at 7 s can also be observed.

The wavelet spectra of the NES alone, presented in Fig. 4.32 shows a continuing broadband of frequency content extending for longer periods of time with the main frequency being nonlinear in nature, as a slope from its linear to lower values can be slightly observed after 7 s.

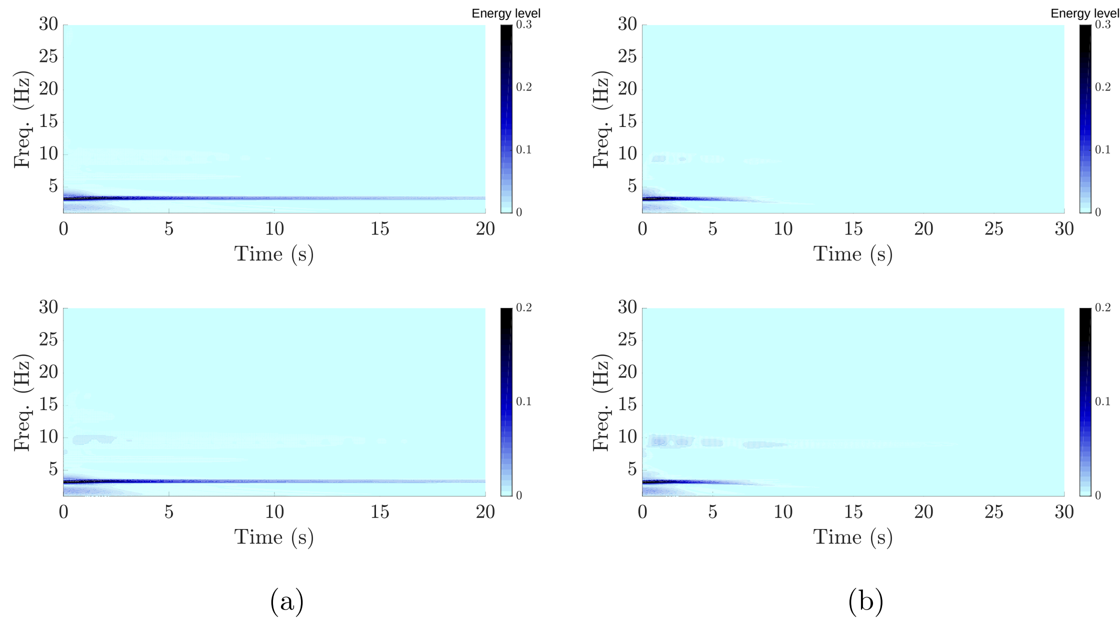

Figure 4.31. : Wavelet spectra plots of Case 6. (a) PO with NES locked (bottom: 1st DOF, top: 2nd DOF); (b) PO with NES unlocked.

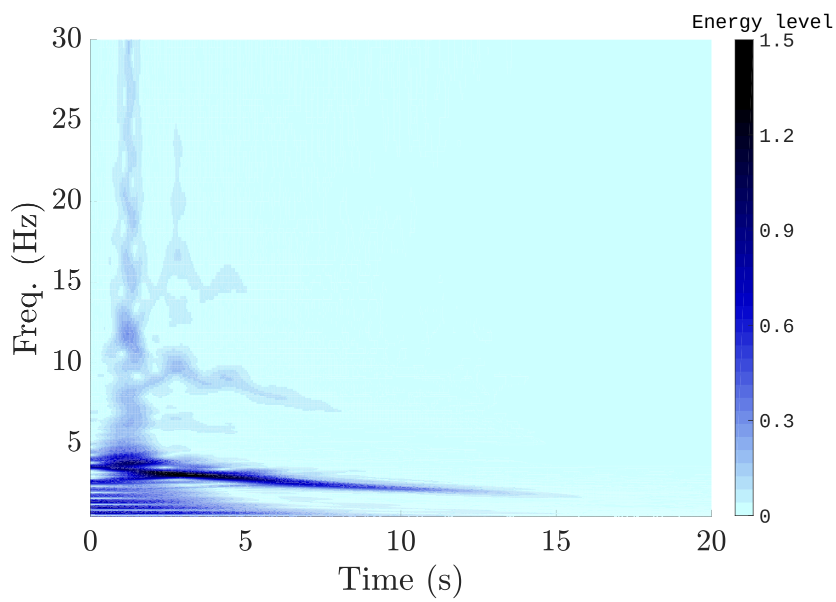

Figure 4.32. : Wavelet spectra of NES velocity (Case 6).

5. SUMMARY AND CONCLUSIONS

Nonlinear energy sinks are powerful, yet not fully developed alternatives for vibration attenuation of linear structures. There has been a tremendous amount of research investigating the theoretical and experimental behavior of several types of these devices, with varied results, most of which agree on the potential and versatility of NES as fully passive vibration absorbers: some properties that make them an interesting option in addition to linear tuned mass dampers are their frequency broadband and their remarkable dissipation and energy transfer capabilities. However, these devices are not free from limitations, and one of the most visible is their implementation complexity. Some of the most studied NES configurations are based on complex experimental setups that serve great for experimental demonstration purposes, but not for service implementation in actual structures. Due to this limitation, the potential for new and improved devices with nonlinear energy transfer capability is rather large and open. As a consequence of this gap that is still yet to be filled, this dissertation sought to investigate a new type of NES device, based on a simple configuration of a cantilevered beam, whose lateral vibrations are constrained by a pair of specially-shaped rigid boundaries that produce an effect of variable length on the beam, thus eliminating its linear vibratory characteristic in favor of a nonlinear one.

The investigation presented in this dissertation involved three main contributions: 1) the study and evaluation of the power per unit mass of a vibratory system, comprised of a linear primary oscillator, attached to a nonlinear energy sink, as a means to further visualize and understand the energy interactions between these two subsystems (PO and NES); 2) the development of a refined, physics-based model for the proposed NES configuration that predicts its behavior and energy absorption capacity with reasonable accuracy; and, 3) the experimental verification of the model, and the nonlinear energy absorption properties of the beam NES device when attached to a scaled lab structure. In addition to these three main directions, preliminary chapters of this dissertation examine the literature related to NES, targeted energy transfer and nonlinear springs for vibration-related applications, then, a short background section, where some of the mathematical tools utilized in the treatment of the analysis presented in this dissertation are briefly explained.

The first contribution to this work includes the development of a technique for analyzing and evaluating the direction in which energy is traveling within a primary oscillator – nonlinear energy sink system. Past numerical results and experimental observations demonstrate the occurrence of energy backflow between a nonlinear energy sink and the primary system to which it is attached. The causes for this phenomenon are not yet fully understood. However, the presence of linear components of stiffness in experimental and applied scenarios are thought to be responsible for a good portion of it. The introduction of the quantity power per unit mass of the primary oscillator is presented as a practical and straightforward methodology for evaluating the direction of the energy in targeted energy transfer systems, with the quantity being in the negative region when the structure acts in pure dissipation (energy leaving), and in the positive region when the structure acts in pure oscillation (energy returning). This methodology aims to build upon existing techniques for energy evaluation of nonlinear energy sinks and the energy activity between these and the primary structures to which they are attached. Results obtained from simulations and experiments demonstrate that it may be a powerful method in addition to the already available energy measures of percentage of instantaneous energy dissipated in the NES and energy per unit mass of the primary system. The developed models also constitute powerful tools for analyzing different types of responses of a two-DOF primary system with an NES mounted on the second mass.

A controlled increment in the damping of the dissipation device was used to lower the effects of energy backflow. To achieve this, two mechanical alternatives were explored: 1) the increment of viscous damping in the NES (experimentally through variable force air dashpots), and, 2) the addition of a very simple steady-state aerodynamic quadratic damping term from a drag source (experimentally achieved through the attachment of a "sail" to the NES). A series of computational simulations of defined damping cases were performed, and the responses of the NES-retrofitted systems show a significant decrease of oscillating response (energy interchange between primary system and the NES). Some undesirable effects may appear due to many sources of error, particularly because of the presence of measurement noise amplification, and integration errors. Further investigation extending this methodology may include state-estimation techniques such as the use of nonlinear state estimators to obtain a better set of state responses.

The investigation of a new type of nonlinear energy sink based on a cantilevered beam with bounded lateral vibration is the second contribution of this dissertation, and it is performed in two stages: 1) the development of the model; and 2) the experimental verification of the validity of the model and the behavior of the physical device. The application of a nonlinear spring, based on a cantilever beam with a concentrated mass on the tip, having a constraint about its lateral displacement caused by a specially shaped rigid boundary is proposed here as a possible option for vibration attenuation applications. A semi-analytical dynamic model was developed based on the equations of plane kinematics of rigid bodies, with the assumption that the device behaves as a pendulum with a concentrated mass on its tip. First, a static analysis was performed to determine that the nonlinearity can be described as a ninth-order spring, due to the pronounced F-D behavior; and second, equations of motion were mathematically derived using Lagrangian mechanics. Numerical simulations demonstrate that the model captures the amplitudes and frequencies of oscillation reasonably well when the device is subjected to different amplitudes of excitation. Moreover, these simulations agree reasonably well with the approximated analytical solution. A series of laboratory experiments were also conducted for selected cases of physical realizations of the proposed device. The observed results compared with the simulations, as well as with the analytical solution, show less agreement both in frequency and amplitude. Some of the possible reasons for this lack of close agreement may include unmodeled dynamics, experimental uncertainties like the shape of the excitation function, and measurement errors. Nonetheless, the results suggest that this class of spring behaves as a nonlinear element with potential for vibration absorption applications. From the experimental studies, it became apparent that as the degree of curvature of the limiting boundary grows, the nonlinear behavior of the spring also increases (hardening behavior). Finally, the intrinsic amplitude-dependency of most nonlinear systems was also demonstrated in this device.

The third contribution of this dissertation included the numerical and experimental verification of the NES as a valid vibration reduction device, when attached to a scale lab structure subjected to shake table base excitation. The numerical model was coupled to a linear two-DOF mass-spring-damper model that was simulated using state-of-the-art computational tools. These results were then compared to those obtained from the measured acceleration responses of the two DOFs of the linear structure, as well as of the tip of the beam NES. These series of computational simulations and experiments have consistently demonstrated the capacity of the beam-based nonlinear spring proposed in this dissertation, to absorb and dissipate vibratory energy of the host structure. From low to moderate to high energy levels of excitation the device showed high dissipation properties associated with adequate design of physical characteristics, such as beam material and dimensions, NES damping, and tip mass. It should be emphasized that a careful trade off between these parameters is required to achieve an optimal realization of NES that would eventually succeed in extracting vibratory energy from a linear base oscillating system.

5.1 Future directions of research

Most of the NES studies presented by researchers, including this dissertation, focus on the theoretical and experimental treatment of the NES for applications in the field of structural dynamics. The applicability of these types of systems in different problems in engineering is immense and further studies are needed not only to help close the gap between theory and implementation, but also to develop more types of NES based on geometric nonlinearities. There is still a need for implementations in vertical direction and spacial motion (3D).

The model presented in this dissertation, though valid and powerful, still is approximated, based on several assumptions that may be improved. A further study of the model of the cantilevered beam-NES could bring about the development of a fully analytical model that does not rely on a previous static analysis, but in an integral manner. Moreover, a series of systematic studies involving varying damping, mass and beam shapes shall be of great use in the development of the beam NES as a powerful device for future use in engineering applications.

Bibliography

Al-Shudeifat, M. A. (2014). Highly efficient nonlinear energy sink. *Nonlinear Dynamics*, 76(4):1905–1920.

Al-Shudeifat, M. A., Wierschem, N. E., Bergman, L. A., and Vakakis, A. F. (2017). Numerical and experimental investigations of a rotating nonlinear energy sink. *Meccanica*, 52(4-5):763–779.

Alexander, N. A. and Schilder, F. (2009). Exploring the performance of a nonlinear tuned mass damper. *Journal of Sound and Vibration*, 319(1-2):445–462.

Bab, S., Khadem, S. E., and Shahgholi, M. (2014). Lateral vibration attenuation of a rotor under mass eccentricity force using non-linear energy sink. *International Journal of Non-Linear Mechanics*, 67(1):251–266.

Bernard, B. P. and Mann, B. P. (2018). Increasing viability of nonlinear energy harvesters by adding an excited dynamic magnifier. *Journal of Intelligent Material Systems and Structures*, 29(6):1196–1205.

Blackwell, R. J. (1986). *Christiaan Huygens' The Pendulum Clock, or, Geometrical Demonstrations Concerning the Motion of Pendula as Applied to Clocks*. Iowa State University Press, Ames, IA, 1st edition.

Borowski, V. J., Denman, H. H., Cronin, D. L., Shaw, S. W., Hanisko, J. P., Brooks, L. T., Mikulec, D. A., Crum, W. B., and Anderson, M. P. (1991). Reducing vibration of reciprocating engines with crankshaft pendulum vibration absorbers. *SAE Transactions*, 100(2):376–382.

Caruntu, D. I. (2009). Dynamic modal characteristics of transverse vibrations of cantilevers of parabolic thickness. *Mechanics Research Communications*, 36(3):391–404.

Chopra, A. K. (2012). *Dynamics of Structures*. Prentice Hall, Upper Saddle River, 4th edition.

Den Hartog, J. (1985). *Mechanical Vibrations*. Dover Publications.

Desalvo, R. (2007). Passive, nonlinear, mechanical structures for seismic attenuation. *Journal of Computational and Nonlinear Dynamics*, 2(4):290–298.

Elias, S. and Matsagar, V. (2017). Research developments in vibration control of structures using passive tuned mass dampers. *Journal of Vibration and Acoustics*, 44(1):129–156.

Gendelman, O. and Alloni, A. (2015). Dynamics of forced system with vibro-impact energy sink. *Journal of Sound and Vibration*, 358(1):301–314.

Gendelman, O., Sapsis, T., Vakakis, A., and Bergman, L. (2011). Enhanced passive targeted energy transfer in strongly nonlinear mechanical oscillators. *Journal of Sound and Vibration*, 330(1):1–8.

Gendelman, O. V., Manevitch, L. I., Vakakis, A. F., and M'closkey, R. (2001). Energy pumping in nonlinear mechanical oscillators: part I—dynamics of the underlying Hamiltonian systems. *Journal of Applied Mechanics*, 68(1):34.

Gendelman, O. V., Sigalov, G., Manevitch, L. I., Mane, M., Vakakis, A. F., and Bergman, L. A. (2012). Dynamics of an eccentric rotational nonlinear energy sink. *Journal of Applied Mechanics*, 79(1):1–9.

Gourc, E., Michon, G., Seguy, S., and Berlioz, A. (2015). Targeted energy transfer under harmonic forcing with a vibro-impact nonlinear energy sink: analytical and experimental developments. *Journal of Vibration and Acoustics*, 137(3):031008.

Gourdon, E., Alexander, N., Taylor, C., Lamarque, C., and Pernot, S. (2007a). Nonlinear energy pumping under transient forcing with strongly nonlinear coupling: Theoretical and experimental results. *Journal of Sound and Vibration*, 300(3-5):522–551.

Gourdon, E., Lamarque, C. H., and Pernot, S. (2007b). Contribution to efficiency of irreversible passive energy pumping with a strong nonlinear attachment. *Nonlinear Dynamics*, 50(4):793–808.

Goyal, S. and Whalen, T. M. (2005). Design and application of a nonlinear energy sink to mitigate vibrations of an air spring-supported slab. In *ASME 2005 International Design Engineering Technical Conferences & Computers and Information in Engineering Conference*, pages 2331–2339.

Haddow, A. G. and Shaw, S. W. (2003). Centrifugal Pendulum Vibration Absorbers: An Experimental and Theoretical Investigation. *Nonlinear Dynamics*, 34(3/4):293–307.

Hubbard, S. A., Copeland, T. J., Michael, D., Farland, M. C., Bergman, L. A., and Vakakis, A. F. (2012). Characterization of a strongly nonlinear vibration absorber for aerospace applications. In *Topics in Nonlinear Dynamics*, pages 199–207. Springer Science & Business Media.

Hubbard, S. A., Mcfarland, D. M., Bergman, L. A., and Vakakis, A. F. (2010). Targeted energy transfer between a model flexible wing and nonlinear energy sink. *Journal of Aircraft*, 47(6):1918–1931.

Izzi, M., Caracoglia, L., and Noè, S. (2016). Investigating the use of targeted energy transfer devices for stay-cable vibration mitigation. *Structural Control and Health Monitoring*, 23(2):315–332.

Kani, M., Khadem, S. E., Pashaei, M. H., and Dardel, M. (2016). Design and performance analysis of a nonlinear energy sink attached to a beam with different support conditions. *Proceedings of the Institution of Mechanical Engineers, Part C: Journal of Mechanical Engineering Science*, 230(4):527–542.

Keer, L. and Silva, M. (1970). Bending of a cantilever brought gradually into contact with a cylindrical supporting surface. *International Journal of Mechanical Sciences*, 12(9):751–760.

Kerschen, G., Kowtko, J. J., Mcfarland, D. M., Bergman, L. A., and Vakakis, A. F. (2007a). Theoretical and experimental study of multimodal targeted energy transfer in a system of coupled oscillators. *Nonlinear Dynamics*, 47(1-3):285–309.

Kerschen, G., Lee, Y. S., Vakakis, A. F., McFarland, D. M., and Bergman, L. A. (2005). Irreversible passive energy transfer in coupled oscillators with essential nonlinearity. *SIAM Journal on Applied Mathematics*, 66(2):648–679.

Kerschen, G., Mcfarland, D. M., Kowtko, J. J., Lee, Y. S., Bergman, L. A., and Vakakis, A. F. (2007b). Experimental demonstration of transient resonance capture in a system of two coupled oscillators with essential stiffness nonlinearity. *Journal of Sound and Vibration*, 299(4-5):822–838.

Kerschen, G., Worden, K., Vakakis, A. F., and Golinval, J.-C. (2006). Past, present and future of nonlinear system identification in structural dynamics. *Mechanical Systems and Signal Processing*, 20(3):505–592.

Kluger, J. M., Sapsis, T. P., and Slocum, A. H. (2015). Robust energy harvesting from walking vibrations by means of nonlinear cantilever beams. *Journal of Sound and Vibration*, 341(April 14):174–194.

Kluger, J. M., Slocum, A. H., Hardt, D. E., and Kluger, J. M. (2014). *Nonlinear Beam-Based Vibration Energy Harvesters and Load Cells*. PhD thesis, MIT.

Krack, M. and Gross, J. (2019). *Harmonic Balance for Nonlinear Vibration Problems*. Springer Nature Switzerland, Cham, Switzerland.

Kremer, D. and Liu, K. (2014). A nonlinear energy sink with an energy harvester: Transient responses. *Journal of Sound and Vibration*, 333(20):4859–4880.

Lamarque, C.-H., Gendelman, O. V., Ture Savadkoohi, A., and Etcheverria, E. (2011). Targeted energy transfer in mechanical systems by means of non-smooth nonlinear energy sink. *Acta Mech*, 221(September):175–200.

Liu, W., Liu, C., Li, X., Zhu, Q., and Hu, G. (2018). Comparative study about the cantilever generators with different curve fixtures. *Journal of Intelligent Material Systems and Structures*, 29(9):1884–1899.

Lu, X., Liu, Z., and Lu, Z. (2017). Optimization design and experimental verification of track nonlinear energy sink for vibration control under seismic excitation. *Structural Control and Health Monitoring*, 24(12):e2033.

Lu, Z., Wang, Z., Zhou, Y., and Lu, X. (2018). Nonlinear dissipative devices in structural vibration control: A review. *Journal of Sound and Vibration*, 423(June 9):18–49.

Luo, J., Wierschem, N. E., Hubbard, S. A., Fahnestock, L. A., Dane Quinn, D., Michael McFarland, D., Spencer, B. F., Vakakis, A. F., and Bergman, L. A. (2014). Large-scale experimental evaluation and numerical simulation of a system of nonlinear energy sinks for seismic mitigation. *Engineering Structures*, 77(October 15):34–48.

McFarland, D. M., Bergman, L. A., and Vakakis, A. F. (2004). Experimental study of nonlinear energy pumping. In *XXI ICTAM*, pages 1–2, Warsaw.

Mcfarland, D. M., Bergman, L. A., and Vakakis, A. F. (2005). Experimental study of non-linear energy pumping occurring at a single fast frequency. *International Journal of Non-Linear Mechanics*, 40(6):891–899.

McFarland, D. M., Kerschen, G., Kowtko, J. J., Lee, Y. S., Bergman, L. A., and Vakakis, A. F. (2005). Experimental investigation of targeted energy transfers in strongly and nonlinearly coupled oscillators. *The Journal of the Acoustical Society of America*, 118(2):791–799.

Nayfeh, A. H. and Balachandran, B. (2004). *Applied Nonlinear Dynamics*. Wiley-VCH, Weinheim, 2nd edition.

Nucera, F., Lo Iacono, F., McFarland, D. M., Bergman, L. A., and Vakakis, A. F. (2008). Application of broadband nonlinear targeted energy transfers for seismic mitigation of a shear frame: Experimental results. *Journal of Sound and Vibration*, 313(2008):57–76.

Nucera, F., McFarland, D. M., Bergman, L. A., Vakakis, A. F., and Lo Iacono, F. (2010). Application of broadband nonlinear targeted energy transfers for seismic mitigation of a shear frame: Computational results. *Journal of Sound and Vibration*, 329(15):2973–2994.

Ormondroyd, J. and Den Hartog, J. (1928). Theory ofthe dynamic vibration absorber. *Transactions of the American Society of Mechanical Engineers*, 50:9–22.

Ramsey, J. and Wierschem, N. (2017). Passive control of the vibration of flooring systems using a gravity compensated non-linear energy sink. In *Proceedings of the 13th International Workshop on Advanced Smart Materials and Smart Structures Technology*, page 8, Tokyo. The University of Tokyo.

Rivlin, B. (2012). *Micromecanical flexures : non-linear springs for enhancing the functionality of electrostatic transducers*. PhD thesis, TECHNION.

Rivlin, B. and Elata, D. (2012). Design of nonlinear springs for attaining a linear response in gap-closing electrostatic actuators. *International Journal of Solids and Structures*, 49(26):3816–3822.

Rowell, D. (2003). 2.151: Energy and Power Flow in State Determined Systems 1. Chapter 2 notes. Retrieved from https://stuff.mit.edu/afs/athena/course/2/2.151/www/Handouts/EnPwrFlow.pdf.

Sharif-Bakhtiar, M. and Shaw, S. (1988). The dynamic response of a centrifugal pendulum vibration absorber with motion-limiting stops. *Journal of Sound and Vibration*, 126(2):221–235.

Shaw, S. W. (1985a). The Dynamics of a Harmonically Excited System Having Rigid Amplitude Constraints, Part 1: Subharmonic Motions and Local Bifurcations. *Journal of Applied Mechanics*, 52(2):453–458.

Shaw, S. W. (1985b). The Dynamics of a Harmonically Excited System Having Rigid Amplitude Constraints, Part 2: Chaotic Motions and Global Bifurcations. *Journal of Applied Mechanics*, 52(2):459–464.

Shaw, S. W. and Wiggins, S. (1988). Chaotic Motions of a Torsional Vibration Absorber. *Journal of Applied Mechanics*, 55(4):952–958.

Shmulevich, S., Joffe, A., Grinberg, I. H., and Elata, D. (2015). On the notion of a mechanical battery. *Journal of Microelectromechanical Systems*, 24(4):1085–1091.

Shmulevich, S., Rivlin, B., Hotzen, I., and Elata, D. (2013). A gap-closing electrostatic actuator with a linear extended range. *Journal of Microelectromechanical Systems*, 22(5):582–585.

Sigalov, G., Gendelman, O. V., AL-Shudeifat, M. A., Manevitch, L. I., Vakakis, A. F., and Bergman, L. A. (2012a). Resonance captures and targeted energy transfers in an inertially-coupled rotational nonlinear energy sink. *Nonlinear Dynamics*, 69(4):1693–1704.

Sigalov, G. G., Gendelman, O. V., AL-Shudeifat, M. A., Manevitch, L. I., Vakakis, A. F., and Bergman, L. A. (2012b). Alternation of regular and chaotic dynamics in a simple two-degree-of-freedom system with nonlinear inertial coupling. *Chaos*, 22(1):013118.

Silva, C. E., Maghareh, A., Tao, H., Dyke, S. J., and Gibert, J. (2019). Evaluation of energy and power flow in a nonlinear energy sink attached to a linear primary oscillator. *Journal of Vibration and Acoustics*, 141(6):061012.

Spreemann, D., Folkmer, B., and Manoli, Y. (2011). Realization of nonlinear springs with predefined chracteristic for vibration transducer based on beam structures. In *Mikro System Tecknik Kongress*, pages 371–374, Darmstadt, Deutschland.

Starosvetsky, Y. and Gendelman, O. (2010). Interaction of nonlinear energy sink with a two degrees of freedom linear system: Internal resonance. *Journal of Sound and Vibration*, 329(10):1836–1852.

Starosvetsky, Y. and Gendelman, O. V. (2009). Vibration absorption in systems with a nonlinear energy sink: Nonlinear damping. *Journal of Sound and Vibration*, 324(3-5):916–939.

Tang, L. and Yang, Y. (2012). A multiple-degree-of-freedom piezoelectric energy harvesting model. *Journal of Intelligent Material Systems and Structures*, 23(14):1631–1647.

Tao, H. and Gibert, J. (2019). Periodic orbits of a conservative 2-DOF vibro-impact system by piecewise continuation: bifurcations and fractals. *Nonlinear Dynamics*, 95(4):2963–2993.

The Mathworks Inc. (2018). MATLAB.

Timoshenko, S. (1940). *Strength of Materials Part II.* D. Van Nostrand Company, Inc., New York, NY, second edition.

Tripathi, A., Grover, P., and Kalmár-Nagy, T. (2017). On optimal performance of nonlinear energy sinks in multiple-degree-of-freedom systems. *Journal of Sound and Vibration*, 388(February 3):272–297.

Uang, C.-m. and Bertero, V. V. (1990). Evaluation of seismic energy in structures. *Earthquake Engineering and Structural Dynamics*, 19(1):77–90.

Vakakis, A. F. and Gendelman, O. (2001). Energy pumping in nonlinear mechanical oscillators, part II: Resonance capture. *Journal of Applied Mechanics*, 68(1):42–48.

Vakakis, A. F., Gendelman, O., Bergman, L. A., McFarland, D. M., Kerschen, G., and Lee, Y. S. (2008). *Nonlinear Targeted Energy Transfer in Mechanical and Structural Systems*. Springer Science & Business Media.

Vakakis, A. F., McFarland, D. M., Bergman, L., Manevitch, L. I., and Gendelman, O. (2004). Isolated resonance captures and resonance capture cascades leading to single or multi-mode passive energy pumping in damped coupled oscillators. *Journal of Vibration and Acoustics*, 126(2):235–244.

Wang, C., Zhang, Q., Wang, W., and Feng, J. (2018). A low-frequency, wide-band quad-stable energy harvester using combined nonlinearity and frequency up-conversion by cantilever-surface contact. *Mechanical Systems and Signal Processing*, 112(11):305–318.

Wang, J., Wierschem, N., Spencer, B. F., and Lu, X. (2015a). Experimental study of track nonlinear energy sinks for dynamic response reduction. *Engineering Structures*, 94(July 1):9–15.

Wang, J., Wierschem, N. E., Spencer, B. F., and Lu, X. (2015b). Track nonlinear energy sink for rapid response reduction in building structures. *Journal of Engineering Mechanics*, 141(1):04014104.

Wierschem, N. E. (2014). *Targeted energy transfer using nonlinear energy sinks for the attenuation of transient loads on building structures*. PhD thesis, University of Illinois at Urbana-Champaign.

Wierschem, N. E., Hubbard, S. A., Luo, J., Fahnestock, L. A., Spencer, B. F., McFarland, D. M., Quinn, D. D., Vakakis, A. F., and Bergman, L. A. (2017). Response attenuation in a large-scale structure subjected to blast excitation utilizing a system of essentially nonlinear vibration absorbers. *Journal of Sound and Vibration*, 389(February 17):52–72.

Wierschem, N. E., Luo, J., Hubbard, S., Fahnestock, L. A., Spencer, B. F., Vakakis, A. F., Bergman, L. A., Grafton, W., and Wilkins, L. B. (2013). Experimental testing of a large 9-story structure equipped with multiple nonlinear energy sinks subjected to an impulsive loading. In *ASCE Structures Congress*, Reston, VA. American Society of Civil Engineers.

Yamaguchi, H. and Harnpornchai, N. (1993). Fundamental characteristics of multiple tuned mass dampers for suppressing harmonically forced oscillations. *Earthquake Engineering & Structural Dynamics*, 22(1):51–62.

Zahrah, T. F. and Hall, W. J. (1984). Earthquake Energy Absorption in SDOF Structures. *Journal of Structural Engineering*, 110(8):1757–1772.

Zhang, Y., Tang, L., and Liu, K. (2017). Piezoelectric energy harvesting with a nonlinear energy sink. *Journal of Intelligent Material Systems and Structures*, 28(3):307–322.

APPENDICES

A. APPENDIX A. HARMONIC BALANCE DERIVATION

Maple sheet for computing the systems of nonlinear algebraic equations that determine the forced response curves and modal backbones of a nonlinear spring with nonlinear characteristic of 9th order, by applying the **harmonic balance method.**

Single degree of freedom case:

Equation of the one degree of freedom oscillator (residual equation):

restart;

$$eom := \frac{d^2}{d\,tau^2}\,\text{theta}(\text{tau}) + \text{lambda}\cdot\frac{d}{d\,tau}\,\text{theta}(\text{tau}) + \text{theta}(\text{tau}) + \varepsilon\cdot\text{theta}(\text{tau})^9 + \text{Gamma}\cdot\omega^2\cdot F_0\cdot\cos(\text{Omega}\cdot\text{tau})$$

$$eom := \frac{d^2}{d\tau^2}\,\theta(\tau) + \lambda\left(\frac{d}{d\tau}\,\theta(\tau)\right) + \theta(\tau) + \varepsilon\,\theta(\tau)^9 + \Gamma\,\omega^2 F_0 \cos(\Omega\,\tau) \tag{1}$$

Substitute a solution with one single fundamental harmonic [one-term expansion x(t) = Acos(ωt) + Bsin(ω)]:

$$esol := subs(\text{theta}(\text{tau}) = A\cdot\cos(\text{Omega}\cdot\text{tau}) + B\cdot\sin(\text{Omega}\cdot\text{tau}), eom)$$

$$esol := \frac{\partial^2}{\partial\tau^2}\,(A\cos(\Omega\,\tau) + B\sin(\Omega\,\tau)) + \lambda\left(\frac{\partial}{\partial\tau}\,(A\cos(\Omega\,\tau) + B\sin(\Omega\,\tau))\right) + A\cos(\Omega\,\tau) + B\sin(\Omega\,\tau) + \varepsilon\,(A\cos(\Omega\,\tau) + B\sin(\Omega\,\tau))^9 + \Gamma\,\omega^2 F_0\cos(\Omega\,\tau) \tag{2}$$

Expanding and simplifying:

$$eq := expand(esol)$$

$$\begin{aligned} eq :=& -A\,\Omega^2\cos(\Omega\,\tau) - B\,\Omega^2\sin(\Omega\,\tau) - \lambda A\,\Omega\sin(\Omega\,\tau) + \lambda B\,\Omega\cos(\Omega\,\tau) + A\cos(\Omega\,\tau) \\ &+ B\sin(\Omega\,\tau) + \varepsilon A^9\cos(\Omega\,\tau)^9 + 9\,\varepsilon A^8\cos(\Omega\,\tau)^8 B\sin(\Omega\,\tau) \\ &+ 36\,\varepsilon A^7\cos(\Omega\,\tau)^7 B^2\sin(\Omega\,\tau)^2 + 84\,\varepsilon A^6\cos(\Omega\,\tau)^6 B^3\sin(\Omega\,\tau)^3 \\ &+ 126\,\varepsilon A^5\cos(\Omega\,\tau)^5 B^4\sin(\Omega\,\tau)^4 + 126\,\varepsilon A^4\cos(\Omega\,\tau)^4 B^5\sin(\Omega\,\tau)^5 \\ &+ 84\,\varepsilon A^3\cos(\Omega\,\tau)^3 B^6\sin(\Omega\,\tau)^6 + 36\,\varepsilon A^2\cos(\Omega\,\tau)^2 B^7\sin(\Omega\,\tau)^7 \\ &+ 9\,\varepsilon A\cos(\Omega\,\tau)\,B^8\sin(\Omega\,\tau)^8 + \varepsilon B^9\sin(\Omega\,\tau)^9 + \Gamma\,\omega^2 F_0\cos(\Omega\,\tau) \end{aligned} \tag{3}$$

Substitute terms of sin(ωt)^n and cos(ωt)^n with multiple angle trig terms

$$eq1 := combine(eq, trig)$$

$$eq1 := -B\,\Omega^2 \sin(\Omega\,\tau) + \frac{45\,A^2\,B^7 \sin(7\,\Omega\,\tau)\,\varepsilon}{64} - \frac{9\,A^2\,B^7 \sin(5\,\Omega\,\tau)\,\varepsilon}{8} \tag{4}$$

$$+ \frac{63\,A^2\,B^7 \sin(\Omega\,\tau)\,\varepsilon}{32} - \frac{9\,\varepsilon\,A^2\,B^7 \sin(9\,\Omega\,\tau)}{64} + \Gamma\,\omega^2\,F_0 \cos(\Omega\,\tau)$$

$$+ \frac{63\,\varepsilon\,A \cos(\Omega\,\tau)\,B^8}{128} - \frac{63\,\varepsilon\,A\,B^8 \cos(7\,\Omega\,\tau)}{256} + \frac{9\,\varepsilon\,A\,B^8 \cos(9\,\Omega\,\tau)}{256}$$

$$+ \frac{45\,\varepsilon\,A\,B^8 \cos(5\,\Omega\,\tau)}{64} - \frac{63\,\varepsilon\,A\,B^8 \cos(3\,\Omega\,\tau)}{64} - A\,\Omega^2 \cos(\Omega\,\tau) - \lambda\,A\,\Omega \sin(\Omega\,\tau)$$

$$+ \lambda\,B\,\Omega \cos(\Omega\,\tau) + \frac{63\,\varepsilon\,A^8\,B \sin(\Omega\,\tau)}{128} + \frac{9\,\varepsilon\,A^8\,B \sin(9\,\Omega\,\tau)}{256} + \frac{63\,\varepsilon\,A^8\,B \sin(7\,\Omega\,\tau)}{256}$$

$$+ \frac{45\,\varepsilon\,A^8\,B \sin(5\,\Omega\,\tau)}{64} + \frac{63\,\varepsilon\,A^8\,B \sin(3\,\Omega\,\tau)}{64} - \frac{45\,A^7\,B^2 \cos(7\,\Omega\,\tau)\,\varepsilon}{64}$$

$$- \frac{9\,A^7\,B^2 \cos(5\,\Omega\,\tau)\,\varepsilon}{8} + \frac{63\,A^7\,B^2 \cos(\Omega\,\tau)\,\varepsilon}{32} - \frac{9\,\varepsilon\,A^7\,B^2 \cos(9\,\Omega\,\tau)}{64}$$

$$+ \frac{21\,A^6\,B^3 \sin(3\,\Omega\,\tau)\,\varepsilon}{8} + \frac{63\,A^6\,B^3 \sin(\Omega\,\tau)\,\varepsilon}{32} - \frac{21\,\varepsilon\,A^6\,B^3 \sin(9\,\Omega\,\tau)}{64}$$

$$- \frac{63\,\varepsilon\,A^6\,B^3 \sin(7\,\Omega\,\tau)}{64} - \frac{63\,A^5\,B^4 \cos(5\,\Omega\,\tau)\,\varepsilon}{32} - \frac{63\,A^5\,B^4 \cos(3\,\Omega\,\tau)\,\varepsilon}{32}$$

$$+ \frac{189\,A^5\,B^4 \cos(\Omega\,\tau)\,\varepsilon}{64} + \frac{63\,\varepsilon\,A^5\,B^4 \cos(9\,\Omega\,\tau)}{128} + \frac{63\,\varepsilon\,A^5\,B^4 \cos(7\,\Omega\,\tau)}{128}$$

$$+ \frac{63\,A^4\,B^5 \sin(3\,\Omega\,\tau)\,\varepsilon}{32} - \frac{63\,A^4\,B^5 \sin(5\,\Omega\,\tau)\,\varepsilon}{32} + \frac{189\,A^4\,B^5 \sin(\Omega\,\tau)\,\varepsilon}{64}$$

$$- \frac{63\,\varepsilon\,A^4\,B^5 \sin(7\,\Omega\,\tau)}{128} + \frac{63\,\varepsilon\,A^4\,B^5 \sin(9\,\Omega\,\tau)}{128} - \frac{21\,A^3\,B^6 \cos(3\,\Omega\,\tau)\,\varepsilon}{8}$$

$$+ \frac{63\,A^3\,B^6 \cos(\Omega\,\tau)\,\varepsilon}{32} - \frac{21\,\varepsilon\,A^3\,B^6 \cos(9\,\Omega\,\tau)}{64} + \frac{63\,\varepsilon\,A^3\,B^6 \cos(7\,\Omega\,\tau)}{64}$$

$$+ \frac{\varepsilon\,A^9 \cos(9\,\Omega\,\tau)}{256} + \frac{9\,\varepsilon\,A^9 \cos(7\,\Omega\,\tau)}{256} + \frac{9\,\varepsilon\,A^9 \cos(5\,\Omega\,\tau)}{64} + \frac{21\,\varepsilon\,A^9 \cos(3\,\Omega\,\tau)}{64}$$

$$+ \frac{63\,\varepsilon\,A^9 \cos(\Omega\,\tau)}{128} - \frac{21\,\varepsilon\,B^9 \sin(3\,\Omega\,\tau)}{64} + \frac{\varepsilon\,B^9 \sin(9\,\Omega\,\tau)}{256} - \frac{9\,\varepsilon\,B^9 \sin(7\,\Omega\,\tau)}{256}$$

$$+ \frac{9\,\varepsilon\,B^9 \sin(5\,\Omega\,\tau)}{64} + \frac{63\,\varepsilon\,B^9 \sin(\Omega\,\tau)}{128} + A \cos(\Omega\,\tau) + B \sin(\Omega\,\tau)$$

```
Replace trig terms with poly terms: cos(ωt) = y; cos(2ωt) =
y^2; cos(3ωt) = y^3; sin(ωt) = z; sin(2ωt) = z^2, cos(3ωt)
= y^3
```

$$eqsub1 := subs\big(\{\cos(\text{Omega tau}) = y, \cos(2\ \text{Omega tau}) = y^2, \cos(3\ \text{Omega tau}) = y^3, \sin(\text{Omega tau}) = z, \sin(2\ \text{Omega tau}) = z^2, \sin(3\ \text{Omega tau}) = z^3\}, eq1\big)$$

$$eqsub1 := \frac{45\,A^2\,B^7\sin(7\,\Omega\,\tau)\,\varepsilon}{64} - \frac{9\,A^2\,B^7\sin(5\,\Omega\,\tau)\,\varepsilon}{8} - \frac{9\,\varepsilon\,A^2\,B^7\sin(9\,\Omega\,\tau)}{64} - \frac{63\,\varepsilon\,A\,B^8\cos(7\,\Omega\,\tau)}{256} + \frac{9\,\varepsilon\,A\,B^8\cos(9\,\Omega\,\tau)}{256} + \frac{45\,\varepsilon\,A\,B^8\cos(5\,\Omega\,\tau)}{64} + \frac{9\,\varepsilon\,A^8\,B\sin(9\,\Omega\,\tau)}{256} + \frac{63\,\varepsilon\,A^8\,B\sin(7\,\Omega\,\tau)}{256} + \frac{45\,\varepsilon\,A^8\,B\sin(5\,\Omega\,\tau)}{64} - \frac{45\,A^7\,B^2\cos(7\,\Omega\,\tau)\,\varepsilon}{64} - \frac{9\,A^7\,B^2\cos(5\,\Omega\,\tau)\,\varepsilon}{8} - \frac{9\,\varepsilon\,A^7\,B^2\cos(9\,\Omega\,\tau)}{64} - \frac{21\,\varepsilon\,A^6\,B^3\sin(9\,\Omega\,\tau)}{64} - \frac{63\,\varepsilon\,A^6\,B^3\sin(7\,\Omega\,\tau)}{64} - \frac{63\,A^5\,B^4\cos(5\,\Omega\,\tau)\,\varepsilon}{32} + \frac{63\,\varepsilon\,A^5\,B^4\cos(9\,\Omega\,\tau)}{128} + \frac{63\,\varepsilon\,A^5\,B^4\cos(7\,\Omega\,\tau)}{128} - \frac{63\,A^4\,B^5\sin(5\,\Omega\,\tau)\,\varepsilon}{32} - \frac{63\,\varepsilon\,A^4\,B^5\sin(7\,\Omega\,\tau)}{128} + \frac{63\,\varepsilon\,A^4\,B^5\sin(9\,\Omega\,\tau)}{128} - \frac{21\,\varepsilon\,A^3\,B^6\cos(9\,\Omega\,\tau)}{64} + \frac{63\,\varepsilon\,A^3\,B^6\cos(7\,\Omega\,\tau)}{64} + \frac{\varepsilon\,A^9\cos(9\,\Omega\,\tau)}{256} + \frac{9\,\varepsilon\,A^9\cos(7\,\Omega\,\tau)}{256} + \frac{9\,\varepsilon\,A^9\cos(5\,\Omega\,\tau)}{64} + \frac{\varepsilon\,B^9\sin(9\,\Omega\,\tau)}{256} - \frac{9\,\varepsilon\,B^9\sin(7\,\Omega\,\tau)}{256} + \frac{9\,\varepsilon\,B^9\sin(5\,\Omega\,\tau)}{64} + \frac{63\,\varepsilon\,B^9\,z}{128} - A\,\Omega^2\,y + \frac{21\,\varepsilon\,A^9\,y^3}{64} + \frac{63\,\varepsilon\,A^9\,y}{128} - \frac{21\,\varepsilon\,B^9\,z^3}{64} - B\,\Omega^2\,z + A\,y + B\,z + \Gamma\,\omega^2\,F_0\,y + \frac{63\,\varepsilon\,A\,y\,B^8}{128} - \frac{63\,\varepsilon\,A\,B^8\,y^3}{64} - \lambda\,A\,\Omega\,z + \lambda\,B\,\Omega\,y + \frac{63\,\varepsilon\,A^8\,B\,z}{128} + \frac{63\,\varepsilon\,A^8\,B\,z^3}{64} + \frac{63\,A^7\,B^2\,y\,\varepsilon}{32} + \frac{21\,A^6\,B^3\,z^3\,\varepsilon}{8} + \frac{63\,A^6\,B^3\,z\,\varepsilon}{32} - \frac{63\,A^5\,B^4\,y^3\,\varepsilon}{32} + \frac{189\,A^5\,B^4\,y\,\varepsilon}{64} + \frac{63\,A^4\,B^5\,z^3\,\varepsilon}{32} + \frac{189\,A^4\,B^5\,z\,\varepsilon}{64} - \frac{21\,A^3\,B^6\,y^3\,\varepsilon}{8} + \frac{63\,A^3\,B^6\,y\,\varepsilon}{32} + \frac{63\,A^2\,B^7\,z\,\varepsilon}{32} \tag{5}$$

```
Extract coefficients of y=1 and z=1. This generates two
equations: one for y (4) and one for z (5)
```

$coeffy := coeff(eqsub1, y)$

$$coeffy := -A\,\Omega^2 + \frac{63}{128}\,\varepsilon\,A^9 + A + \Gamma\,\omega^2\,F_0 + \frac{63}{128}\,\varepsilon\,A\,B^8 + \lambda\,B\,\Omega + \frac{63}{32}\,\varepsilon\,A^7\,B^2 + \frac{189}{64}\,\varepsilon\,A^5\,B^4 + \frac{63}{32}\,\varepsilon\,A^3\,B^6 \tag{6}$$

$coeffz := coeff(eqsub1, z)$

$$coeffz := \frac{63}{128}\,\varepsilon\,B^9 - B\,\Omega^2 + B - \lambda\,A\,\Omega + \frac{63}{128}\,\varepsilon\,A^8\,B + \frac{63}{32}\,\varepsilon\,A^6\,B^3 + \frac{189}{64}\,\varepsilon\,A^4\,B^5 + \frac{63}{32}\,\varepsilon\,A^2\,B^7 \tag{7}$$

```
Polar substitution: A=acos(θ); B=asin(θ)
```

y-equation:

$eqyP := subs(\{A = a\cos(\text{theta}), B = a\sin(\text{theta})\}, coeffy)$

$$eqyP := -a\cos(\theta)\,\Omega^2 + \frac{63\,\varepsilon\,a^9\cos(\theta)^9}{128} + a\cos(\theta) + \Gamma\,\omega^2 F_0 + \frac{63\,\varepsilon\,a^9\cos(\theta)\sin(\theta)^8}{128} + \lambda\,a\sin(\theta)\,\Omega + \frac{63\,\varepsilon\,a^9\cos(\theta)^7\sin(\theta)^2}{32} + \frac{189\,\varepsilon\,a^9\cos(\theta)^5\sin(\theta)^4}{64} + \frac{63\,\varepsilon\,a^9\cos(\theta)^3\sin(\theta)^6}{32} \tag{8}$$

z-equation:

$eqzP := subs(\{A = a\cos(\text{theta}), B = a\sin(\text{theta})\}, coeffz)$

$$eqzP := \frac{63\,\varepsilon\,a^9\sin(\theta)^9}{128} - a\sin(\theta)\,\Omega^2 + a\sin(\theta) - \lambda\,a\cos(\theta)\,\Omega + \frac{63\,\varepsilon\,a^9\cos(\theta)^8\sin(\theta)}{128} + \frac{63\,\varepsilon\,a^9\cos(\theta)^6\sin(\theta)^3}{32} + \frac{189\,\varepsilon\,a^9\cos(\theta)^4\sin(\theta)^5}{64} + \frac{63\,\varepsilon\,a^9\cos(\theta)^2\sin(\theta)^7}{32} \tag{9}$$

multiply y-equation (8) by cos(θ). This generates h_1:

$h1 := expand(eqyP\cdot\cos(\text{theta}))$

$$h1 := -a\cos(\theta)^2\,\Omega^2 + \frac{63\,\varepsilon\,a^9\cos(\theta)^{10}}{128} + a\cos(\theta)^2 + \cos(\theta)\,\Gamma\,\omega^2 F_0 + \frac{63\,\varepsilon\,a^9\cos(\theta)^2\sin(\theta)^8}{128} + \cos(\theta)\,\lambda\,a\sin(\theta)\,\Omega + \frac{63\,\varepsilon\,a^9\cos(\theta)^8\sin(\theta)^2}{32} + \frac{189\,\varepsilon\,a^9\cos(\theta)^6\sin(\theta)^4}{64} + \frac{63\,\varepsilon\,a^9\cos(\theta)^4\sin(\theta)^6}{32} \tag{10}$$

multiply y-equation (8) by sin(θ). This generates h_2:

$h2 := expand(eqzP\sin(\text{theta}))$

$$h2 := \frac{63\,\varepsilon\,a^9\sin(\theta)^{10}}{128} - a\sin(\theta)^2\,\Omega^2 + a\sin(\theta)^2 - \cos(\theta)\,\lambda\,a\sin(\theta)\,\Omega + \frac{63\,\varepsilon\,a^9\cos(\theta)^8\sin(\theta)^2}{128} + \frac{63\,\varepsilon\,a^9\cos(\theta)^6\sin(\theta)^4}{32} + \frac{189\,\varepsilon\,a^9\cos(\theta)^4\sin(\theta)^6}{64} + \frac{63\,\varepsilon\,a^9\cos(\theta)^2\sin(\theta)^8}{32} \tag{11}$$

multiply y-equation (9) by sin(θ). This generates f_1:

$f1 := expand(eqyP\sin(\text{theta}))$

$$f1 := -\sin(\theta)\, a \cos(\theta)\, \Omega^2 + \frac{63 \sin(\theta)\, \varepsilon\, a^9 \cos(\theta)^9}{128} + \sin(\theta)\, a \cos(\theta) + \sin(\theta)\, \Gamma\, \omega^2 F_0 + \frac{63\, \varepsilon\, a^9 \cos(\theta) \sin(\theta)^9}{128} + \lambda\, a \sin(\theta)^2\, \Omega + \frac{63\, \varepsilon\, a^9 \cos(\theta)^7 \sin(\theta)^3}{32} + \frac{189\, \varepsilon\, a^9 \cos(\theta)^5 \sin(\theta)^5}{64} + \frac{63\, \varepsilon\, a^9 \cos(\theta)^3 \sin(\theta)^7}{32} \tag{12}$$

multiply y-equation (8) by cos(θ). This generates f_2:

$f2 := expand(eqzP \cos(\text{theta}))$

$$f2 := \frac{63\, \varepsilon\, a^9 \cos(\theta) \sin(\theta)^9}{128} - \sin(\theta)\, a \cos(\theta)\, \Omega^2 + \sin(\theta)\, a \cos(\theta) - \lambda\, a \cos(\theta)^2\, \Omega + \frac{63 \sin(\theta)\, \varepsilon\, a^9 \cos(\theta)^9}{128} + \frac{63\, \varepsilon\, a^9 \cos(\theta)^7 \sin(\theta)^3}{32} + \frac{189\, \varepsilon\, a^9 \cos(\theta)^5 \sin(\theta)^5}{64} + \frac{63\, \varepsilon\, a^9 \cos(\theta)^3 \sin(\theta)^7}{32} \tag{13}$$

Combine and trig-reduce h1+h2: a-PHASE EQUATION 1

$freq1 := combine(h1 + h2, trig)$

$$freq1 := a + \frac{63\, \varepsilon\, a^9}{128} - a\, \Omega^2 + \cos(\theta)\, \Gamma\, \omega^2 F_0 \tag{14}$$

Combine and trig-reduce f1-f2: a-PHASE EQUATION 2

$freq2 := combine(f1 - f2, trig)$

$$freq2 := \sin(\theta)\, \Gamma\, \omega^2 F_0 + \lambda\, a\, \Omega \tag{15}$$

Combining (14) and (15), and trig reducing: AMPLITUDE EQUATION

$FreqExp := combine\Big(\big(freq1 - \omega^2 \cdot F_0 \cdot \text{Gamma} \cdot \cos(\text{theta})\big)^2 + \big(freq2 - \omega^2 F_0 \cdot \text{Gamma} \cdot \sin(\text{theta})\big)^2 = \big(\omega^2 \cdot \text{Gamma} \cdot F_0 \sin(\text{theta})\big)^2 + \big(\omega^2 \cdot \text{Gamma} \cdot F_0 \cos(\text{theta})\big)^2, trig\Big)$

$$FreqExp := \frac{3969}{16384} a^{18} \varepsilon^2 - \frac{63}{64} \Omega^2 a^{10} \varepsilon + \frac{63}{64} a^{10} \varepsilon + \Omega^4 a^2 - 2\, \Omega^2 a^2 + a^2 + \lambda^2 a^2 \Omega^2 = F_0^2\, \Gamma^2\, \omega^4 \tag{16}$$

Substitute terms with numeric parameters:

$Amplitude := expand(FreqExp)$

$$Amplitude := \frac{3969}{16384} a^{18} \varepsilon^2 - \frac{63}{64} \Omega^2 a^{10} \varepsilon + \frac{63}{64} a^{10} \varepsilon + \Omega^4 a^2 - 2\, \Omega^2 a^2 + a^2 + \lambda^2 a^2 \Omega^2 = F_0^2\, \omega^4 \tag{17}$$

B. APPENDIX B. SIMULINK DYNAMIC MODEL OF THE BEAM NES COUPLED TO A TWO-DOF STRUCTURE

x_PhiModel3dof

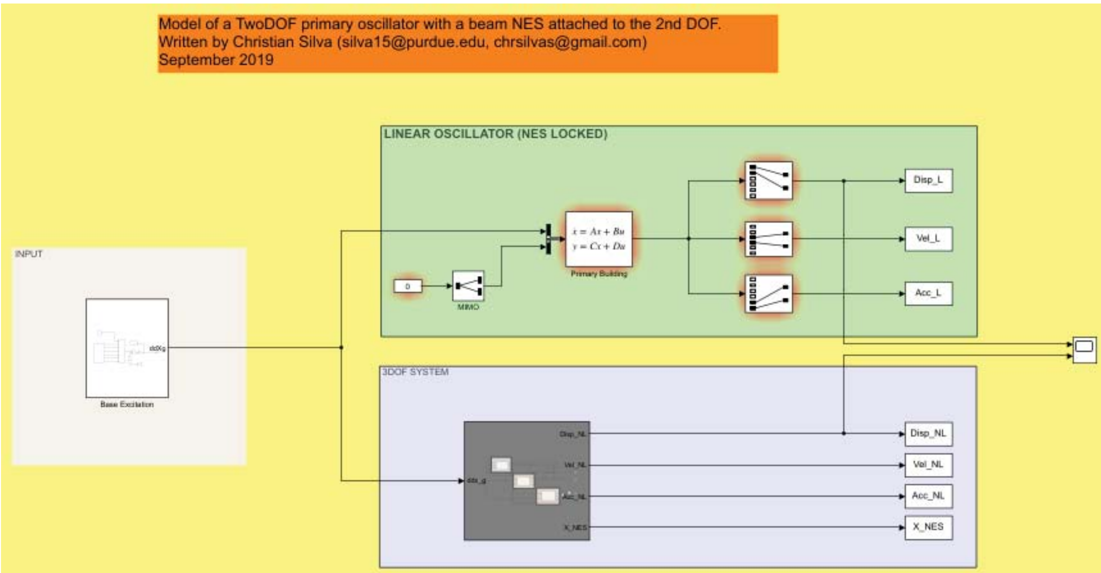

chrsi

23-Sep-2019 22:54:35

Table of Contents

List of Tables

Model - x_PhiModel3dof

Table of Contents

Full Model Hierarchy

1. x_PhiModel3dof
   1. Base Excitation
      1. BASE INPUT
   2. Subsystem
      1. DOF1
      2. DOF2
      3. Subsystem

Simulation Parameter	Value
Solver	ode4
RelTol	1e-3
Refine	1
MaxOrder	5
FixedStep	dt
ZeroCross	on

[more info]

Machine - x_PhiModel3dof

Machine	x_PhiModel3dof
Creation Date	20-Sep-2019 12:05:37

[more info]

System - x_PhiModel3dof

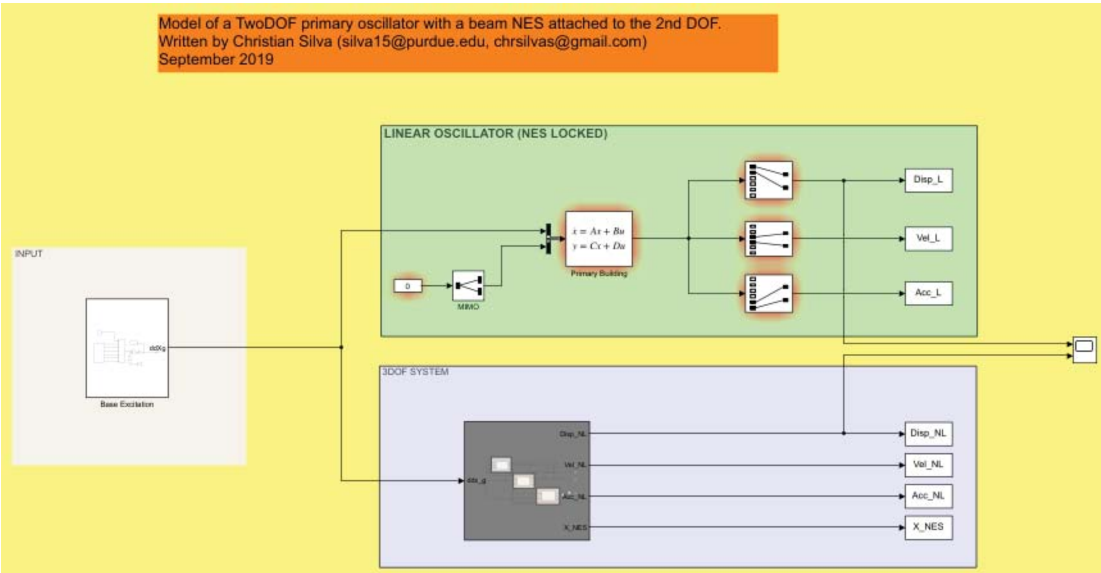

Table 1. BusCreator Block Properties

Name	Inputs	Display Option	Non Virtual Bus	Inherit From Inputs
Bus Creator	2	bar	off	on

Table 2. Constant Block Properties

Name	Value	Out Data Type Str	Lock Scale	Sample Time	Frame Period
Constant	0	Inherit: Inherit from 'Constant value'	off	dt	inf

Table 3. Selector Block Properties

Name	Number Of Dimensions	Index Mode	Index Option Array	Index Param Array	Output Size Array	Input Port Width	Index Options	Indices	Output Sizes
MIMO	1	One-based	Index vector (dialog)	[ones(1,N)]	1	1	Index vector (dialog)	[ones(1,N)]	1
Selector1	1	One-based	Index vector (dialog)	[1:N]	1	3*N	Index vector (dialog)	[1:N]	1
Selector2	1	One-based	Index vector (dialog)	[N+1:2*N]	1	3*N	Index vector (dialog)	[N+1:2*N]	1
Selector3	1	One-based	Index vector (dialog)	[2*N+1:3*N]	1	3*N	Index vector (dialog)	[2*N+1:3*N]	1

Table 4. StateSpace Block Properties

Name	A	B	C	D	Initial Condition	Absolute Tolerance	Continuous State Attributes
Primary Building	AAnl	BBnl	CCnl	DDnl	IC	auto	''

Table 5. ToWorkspace Block Properties

Name	Variable Name	Max Data Points	Decimation	Save Format	Save 2DSignal	Fixpt As Fi
Displacements	Disp_L	inf	1	Array	2-D array (concatenate along first dimension)	on
Displacements1	Vel_L	inf	1	Array	2-D array (concatenate along first dimension)	on

Displacements2	Acc_L	inf	1	Array	2-D array (concatenate along first dimension)	on
To Workspace	Disp_NL	inf	1	Array	2-D array (concatenate along first dimension)	on
To Workspace1	Vel_NL	inf	1	Array	2-D array (concatenate along first dimension)	on
To Workspace2	X_NES	inf	1	Array	2-D array (concatenate along first dimension)	on
To Workspace3	Acc_NL	inf	1	Array	2-D array (concatenate along first dimension)	on

System - x_PhiModel3dof/Base Excitation

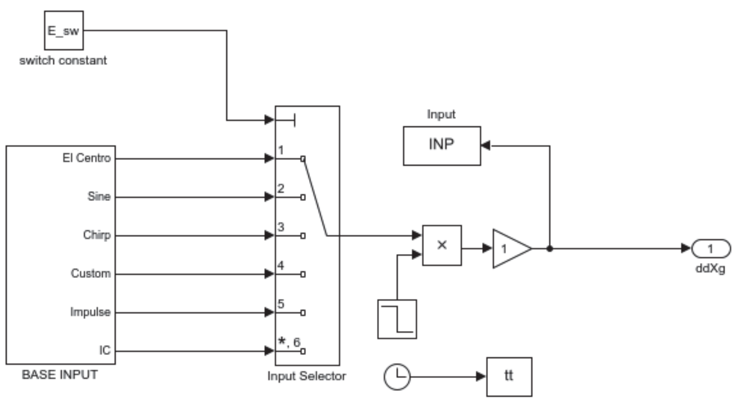

Table 6. Clock Block Properties

Name	Display Time	Decimation
Clock	off	10

Table 7. Constant Block Properties

Name	Value	Out Data Type Str	Lock Scale	Sample Time	Frame Period
switch constant	E_sw	Inherit: Inherit from 'Constant value'	off	dt	inf

Table 8. Gain Block Properties

Name	Gain	Multiplication	Param Data Type Str	Out Data Type Str	Lock Scale	Rnd Meth	Saturate On Integer Overflow
Gain	1	Element-wise(K.*u)	Inherit: Inherit via internal rule	Inherit: Inherit via internal rule	off	Floor	off

Table 9. MultiPortSwitch Block Properties

Name	Data Port Order	Inputs	Data Port Indices	Data Port For Default	Diagnostic For Default	Input Same DT	Out Data Type Str	Lock Scale	Rnd Meth	Saturate On Integer Overflow	Allow Diff Input Sizes
Input Selector	One-based contiguous	6	{1,2,3}	Last data port	Error	off	Inherit: Inherit via internal rule	off	Floor	off	off

Table 10. Outport Block Properties

								Ensure	Source		Must		Output	Vector	

Name	Port	Storage Class	Icon Display	Lock Scale	Unit	Var Size Sig	Signal Type	Outport Is Virtual	Of Initial Output Value	Output When Disabled	Resolve To Signal Object	Output When Un Connected	When Unconnected Value	Params As 1DFor Out When Unconnected	Used By Blk
ddXg	1	Auto	Port number	off	inherit	Inherit	auto	off	Dialog	held	off	off	0	off	mnl/Ig , Sum, Sum1, Primary Building, Input

Table 11. Product Block Properties

Name	Inputs	Multiplication	Collapse Mode	Collapse Dim	Input Same DT	Out Data Type Str	Lock Scale	Rnd Meth	Saturate On Integer Overflow
Product	2	Element-wise(.*)	All dimensions	1	off	Inherit: Inherit via internal rule	off	Floor	off

Table 12. Step Block Properties

Name	Time	Before	After	Sample Time	Zero Cross
Step	Tf	1	0	dt	on

Table 13. ToWorkspace Block Properties

Name	Variable Name	Max Data Points	Decimation	Save Format	Save 2DSignal	Fixpt As Fi
Input	INP	inf	1	Array	2-D array (concatenate along first dimension)	on
time	tt	inf	1	Array	2-D array (concatenate along first dimension)	on

System - x_PhiModel3dof/Base Excitation/BASE INPUT

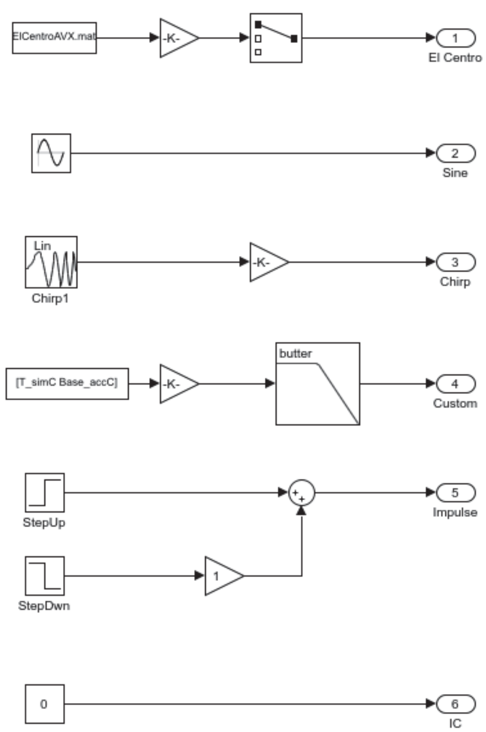

Table 14. Analog Filter Design Block Properties

Name	Method	Filttype	N	Wlo
Analog Filter Design	Butterworth	Lowpass	8	12*2*pi

Table 15. Chirp Block Properties

Name	Sweep	Mode	F0	F1	T1	Tsweep	Phase	Ts	Spf	Datatype
Chirp1	Linear	Unidirectional	f0_chirp	ff_chirp	Tf	Tf	pi/2	1/Fs	1	Double

Table 16. Constant Block Properties

Name	Value	Out Data Type Str	Lock Scale	Sample Time	Frame Period
Constant	0	Inherit: Inherit from 'Constant value'	off	inf	inf

Table 17. FromFile Block Properties

Name	File Name	Sample Time	Extrapolation Before First Data Point	Interpolation Within Time Range	Extrapolation After Last Data Point	Zero Cross
From File1	ElCentroAVX.mat	0	Linear extrapolation	Linear interpolation	Linear extrapolation	off

Table 18. FromWorkspace Block Properties

Name	Variable Name	Sample Time	Interpolate	Zero Cross	Output After Final Value
From Workspace	[T_simC Base_accC]	0	on	on	Extrapolation

Table 19. Gain Block Properties

Name	Gain	Multiplication	Param Data Type Str	Out Data Type Str	Lock Scale	Rnd Meth	Saturate On Integer Overflow
Gain1	gain_chirp	Element-wise(K.*u)	Inherit: Inherit via internal rule	Inherit: Inherit via internal rule	off	Floor	off
Gain3	gain_elcentro	Element-wise(K.*u)	Inherit: Inherit via internal rule	Inherit: Inherit via internal rule	off	Floor	off
Gain4	1	Element-wise(K.*u)	Inherit: Inherit via internal rule	Inherit: Inherit via internal rule	off	Floor	off
Gain5	gain_custom	Element-wise(K.*u)	Inherit: Inherit via internal rule	Inherit: Inherit via internal rule	off	Floor	off

Table 20. Outport Block Properties

Name	Port	Storage Class	Icon Display	Lock Scale	Unit	Var Size Sig	Signal Type	Ensure Outport Is Virtual	Source Of Initial Output Value	Output When Disabled	Must Resolve To Signal Object	Output When Un Connected	Output When Unconnected Value	Vector Params As 1DFor Out When Unconnected	Used By Blk
Chirp	3	Auto	Port number	off	inherit	Inherit	auto	off	Dialog	held	off	off	0	off	Input Selector
Custom	4	Auto	Port number	off	inherit	Inherit	auto	off	Dialog	held	off	off	0	off	Input Selector
El Centro	1	Auto	Port number	off	inherit	Inherit	auto	off	Dialog	held	off	off	0	off	Input Selector
IC	6	Auto	Port number	off	inherit	Inherit	auto	off	Dialog	held	off	off	0	off	Input Selector
Impulse	5	Auto	Port number	off	inherit	Inherit	auto	off	Dialog	held	off	off	0	off	Input Selector
Sine	2	Auto	Port number	off	inherit	Inherit	auto	off	Dialog	held	off	off	0	off	Input Selector

Table 21. Selector Block Properties

Name	Number Of Dimensions	Index Mode	Index Option Array	Index Param Array	Output Size Array	Input Port Width	Index Options	Indices	Output Sizes
[illegible]	[illegible]	[illegible]	Index vector	[illegible]	[illegible]	[illegible]	Index vector	[illegible]	[illegible]

Selector	1	One-based	(dialog)	1	1	3	(dialog)	1	1

Table 22. Sin Block Properties

Name	Sine Type	Time Source	Amplitude	Bias	Frequency	Phase	Samples	Offset	Sample Time
Sine Wave	Time based	Use simulation time	amp_sine	0	w_sine	pi/2	10	0	0

Table 23. Step Block Properties

Name	Time	Before	After	Sample Time	Zero Cross
StepDwn	t0_step+n_delta*dt	0	-amp_step	dt	on
StepUp	t0_step	0	amp_step	dt	on

Table 24. Sum Block Properties

Name	Icon Shape	Inputs	Collapse Mode	Collapse Dim	Input Same DT	Accum Data Type Str	Out Data Type Str	Lock Scale	Rnd Meth	Saturate On Integer Overflow
Sum	round	|++	All dimensions	1	off	Inherit: Inherit via internal rule	Inherit: Inherit via internal rule	off	Floor	off

System - x_PhiModel3dof/Subsystem

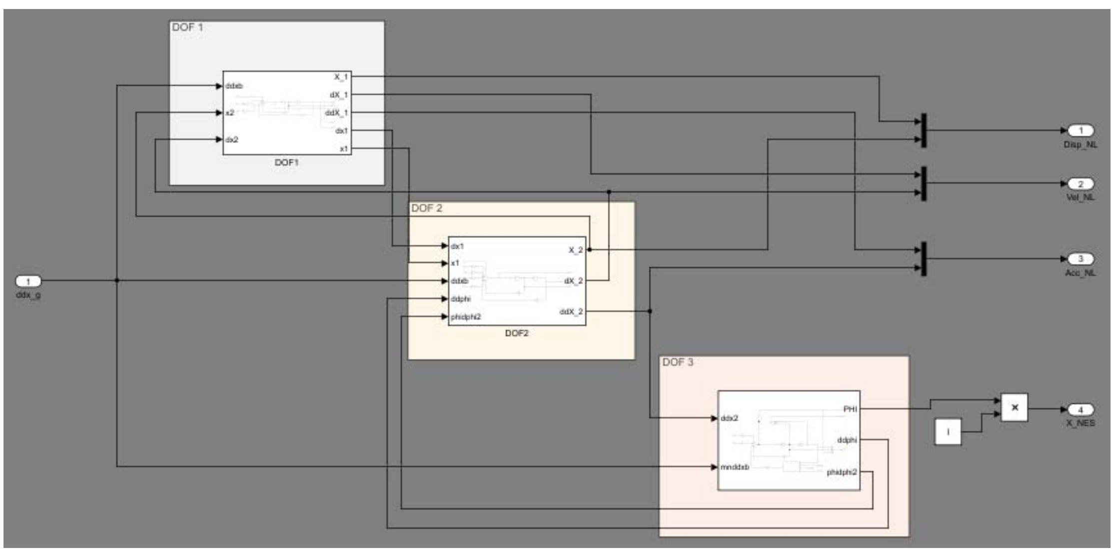

Table 25. Constant Block Properties

Name	Value	Out Data Type Str	Lock Scale	Sample Time	Frame Period
Constant	1	Inherit: Inherit from 'Constant value'	off	inf	inf

Table 26. Inport Block Properties

Name	Port	Defined In Blk
ddx_g	1	Gain

Table 27. Mux Block Properties

Name	Inputs	Display Option
Mux	2	bar
Mux1	2	bar
Mux2	2	bar

Table 28. Outport Block Properties

Name	Port	Storage Class	Icon Display	Lock Scale	Unit	Var Size Sig	Signal Type	Ensure Outport Is Virtual	Source Of Initial Output Value	Output When Disabled	Must Resolve To Signal Object	Output When Un Connected	Output When Unconnected Value	Vector Params As 1DFor Out When Unconnected	Used By Blk
Acc_NL	3	Auto	Port number	off	inherit	Inherit	auto	off	Dialog	held	off	off	0	off	To Workspace3
Disp_NL	1	Auto	Port number	off	inherit	Inherit	auto	off	Dialog	held	off	off	0	off	To Workspace, Scope
Vel_NL	2	Auto	Port number	off	inherit	Inherit	auto	off	Dialog	held	off	off	0	off	To Workspace1
X_NES	4	Auto	Port number	off	inherit	Inherit	auto	off	Dialog	held	off	off	0	off	To Workspace2

Table 29. Product Block Properties

Name	Inputs	Multiplication	Collapse Mode	Collapse Dim	Input Same DT	Out Data Type Str	Lock Scale	Rnd Meth	Saturate On Integer Overflow
Multiply	2	Element-wise(.*)	All dimensions	1	off	Inherit: Inherit via internal rule	off	Floor	off

System - x_PhiModel3dof/Subsystem/DOF1

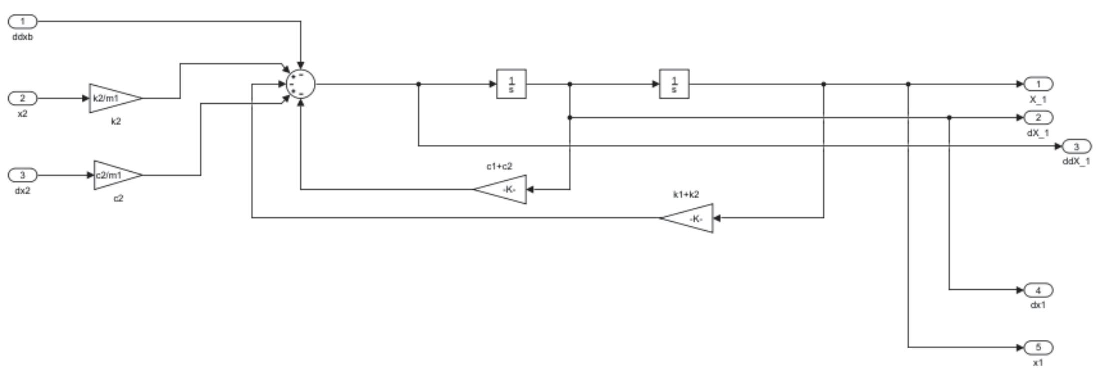

Table 30. Gain Block Properties

Name	Gain	Multiplication	Param Data Type Str	Out Data Type Str	Lock Scale	Rnd Meth	Saturate On Integer Overflow
c1+c2	(c1+c2)/m1	Element-wise(K.*u)	Inherit: Inherit via internal rule	Inherit: Inherit via internal rule	off	Floor	off
c2	c2/m1	Element-wise(K.*u)	Inherit: Inherit via internal rule	Inherit: Inherit via internal rule	off	Floor	off
k1+k2	(k1+k2)/m1	Element-wise(K.*u)	Inherit: Inherit via internal rule	Inherit: Inherit via internal rule	off	Floor	off
k2	k2/m1	Element-wise(K.*u)	Inherit: Inherit via internal rule	Inherit: Inherit via internal rule	off	Floor	off

Table 31. Inport Block Properties

Name	Port	Defined In Blk
ddxb	1	Gain
dx2	3	Integrator2
x2	2	Integrator3

Table 32. Integrator Block Properties

Name	External Reset	Initial Condition Source	Initial Condition	Wrap State	Wrapped State Upper Value	Wrapped State Lower Value	Absolute Tolerance	Zero Cross	Continuous State Attributes
Integrator	none	internal	IC(3)	off	pi	-pi	auto	on	''
Integrator1	none	internal	IC(1)	off	pi	-pi	auto	on	''

Table 33. Outport Block Properties

Name	Port	Storage Class	Icon Display	Lock Scale	Unit	Var Size Sig	Signal Type	Ensure Outport Is Virtual	Source Of Initial Output Value	Output When Disabled	Must Resolve To Signal Object	Output When Un Connected	Output When Unconnected Value	Vector Params As 1DFor Out When Unconnected	Used By Blk
ddX_1	3	Auto	Port number	off	inherit	Inherit	auto	off	Dialog	held	off	off	0	off	To Workspace3, Integrator
dx1	4	Auto	Port number	off	inherit	Inherit	auto	off	Dialog	held	off	off	0	off	To Workspace1, c2/M2, Integrator1, c1+c2
dX_1	2	Auto	Port number	off	inherit	Inherit	auto	off	Dialog	held	off	off	0	off	To Workspace1, c2/M2, Integrator1, c1+c2
x1	5	Auto	Port number	off	inherit	Inherit	auto	off	Dialog	held	off	off	0	off	To Workspace, Scope, k2/M2, k1+k2
X_1	1	Auto	Port number	off	inherit	Inherit	auto	off	Dialog	held	off	off	0	off	To Workspace, Scope, k2/M2, k1+k2

Table 34. Sum Block Properties

Name	Icon Shape	Inputs	Collapse Mode	Collapse Dim	Input Same DT	Accum Data Type Str	Out Data Type Str	Lock Scale	Rnd Meth	Saturate On Integer Overflow
Sum	round	-+-+-	All dimensions	1	off	Inherit: Inherit via internal rule	Inherit: Inherit via internal rule	off	Floor	off

System - x_PhiModel3dof/Subsystem/DOF2

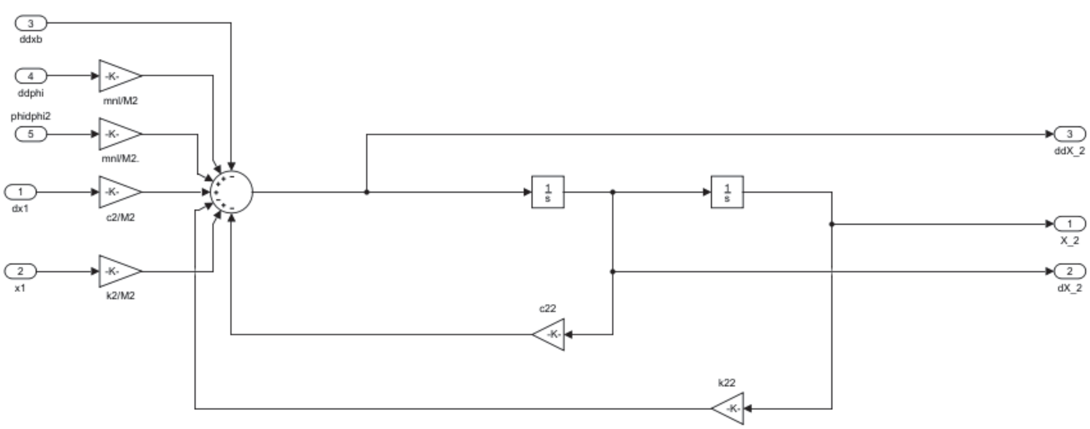

Table 35. Gain Block Properties

Name	Gain	Multiplication	Param Data Type Str	Out Data Type Str	Lock Scale	Rnd Meth	Saturate On Integer Overflow
c2/M2	c2/(m2+mn)	Element-wise(K.*u)	Inherit: Inherit via internal rule	Inherit: Inherit via internal rule	off	Floor	off
c22	c2/(m2+mn)	Element-wise(K.*u)	Inherit: Inherit via internal rule	Inherit: Inherit via internal rule	off	Floor	off
k2/M2	k2/(m2+mn)	Element-wise(K.*u)	Inherit: Inherit via internal rule	Inherit: Inherit via internal rule	off	Floor	off
k22	k2/(m2+mn)	Element-wise(K.*u)	Inherit: Inherit via internal rule	Inherit: Inherit via internal rule	off	Floor	off
mnl/M2	mn*l/(m2+mn)	Element-wise(K.*u)	Inherit: Inherit via internal rule	Inherit: Inherit via internal rule	off	Floor	off
mnl/M2.	mn*l/(m2+mn)	Element-wise(K.*u)	Inherit: Inherit via internal rule	Inherit: Inherit via internal rule	off	Floor	off

Table 36. Inport Block Properties

Name	Port	Defined In Blk
ddphi	4	Unit Delay
ddxb	3	Gain
dx1	1	Integrator
phidphi2	5	Multiply
x1	2	Integrator1

Table 37. Integrator Block Properties

Name	External Reset	Initial Condition Source	Initial Condition	Wrap State	Wrapped State Upper Value	Wrapped State Lower Value	Absolute Tolerance	Zero Cross	Continuous State Attributes
Integrator2	none	internal	IC(4)	off	pi	-pi	auto	on	''
Integrator3	none	internal	IC(2)	off	pi	-pi	auto	on	''

Table 38. Outport Block Properties

Name	Port	Storage Class	Icon Display	Lock Scale	Unit	Var Size Sig	Signal Type	Ensure Outport Is Virtual	Source Of Initial Output Value	Output When Disabled	Must Resolve To Signal Object	Output When Un Connected	Output When Unconnected Value	Vector Params As 1DFor Out When Unconnected	Used By Blk
ddX_2	3	Auto	Port number	off	inherit	Inherit	auto	off	Dialog	held	off	off	0	off	To Workspace3, mnl/Ig, Integrator2
dX_2	2	Auto	Port number	off	inherit	Inherit	auto	off	Dialog	held	off	off	0	off	To Workspace1, c2, c22, Integrator3
X_2	1	Auto	Port number	off	inherit	Inherit	auto	off	Dialog	held	off	off	0	off	To Workspace, Scope, k2, k22

Table 39. Sum Block Properties

Name	Icon Shape	Inputs	Collapse Mode	Collapse Dim	Input Same DT	Accum Data Type Str	Out Data Type Str	Lock Scale	Rnd Meth	Saturate On Integer Overflow
Sum1	round	-+++-+-	All dimensions	1	off	Inherit: Inherit via internal rule	Inherit: Inherit via internal rule	off	Floor	off

System - x_PhiModel3dof/Subsystem/Subsystem

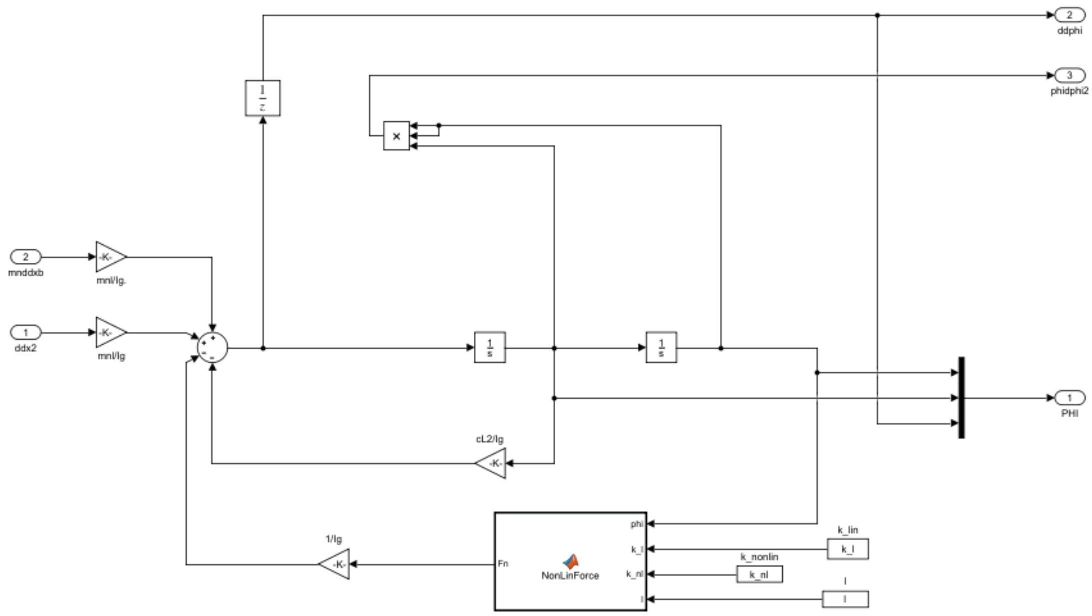

Table 40. Constant Block Properties

Name	Value	Out Data Type Str	Lock Scale	Sample Time	Frame Period
k_lin	k_l	Inherit: Inherit from 'Constant value'	off	inf	inf
k_nonlin	k_nl	Inherit: Inherit from 'Constant value'	off	inf	inf
l	l	Inherit: Inherit from 'Constant value'	off	inf	inf

Table 41. Gain Block Properties

Name	Gain	Multiplication	Param Data Type Str	Out Data Type Str	Lock Scale	Rnd Meth	Saturate On Integer Overflow
1/Ig	1/(I_G+mn*l^2)	Element-wise(K.*u)	Inherit: Inherit via internal rule	Inherit: Inherit via internal rule	off	Floor	off
cL2/Ig	c*l^2/(I_G+mn*l^2)	Element-wise(K.*u)	Inherit: Inherit via internal rule	Inherit: Inherit via internal rule	off	Floor	off
mnl/Ig	mn*l/(I_G+mn*l^2)	Element-wise(K.*u)	Inherit: Inherit via internal rule	Inherit: Inherit via internal rule	off	Floor	off
mnl/Ig.	mn*l/(I_G+mn*l^2)	Element-wise(K.*u)	Inherit: Inherit via internal rule	Inherit: Inherit via internal rule	off	Floor	off

Table 42. Inport Block Properties

Name	Port	Defined In Blk
ddx2	1	Sum1
mnddxb	2	Gain

Table 43. Integrator Block Properties

Name	External Reset	Initial Condition Source	Wrap State	Wrapped State Upper Value	Wrapped State Lower Value	Absolute Tolerance	Zero Cross	Continuous State Attributes
Integrator4	none	internal	off	pi	-pi	auto	on	''
Integrator5	none	internal	off	pi	-pi	auto	on	''

Table 44. MATLAB Function Block Properties

Name	Script

MATLAB Function	function Fn = NonLinForce(phi,k_l,k_nl,l)
	g = 9.81;
	mn = 0.13;
	
	Fn = (k_l*l^2 - mn*g*l*0)*phi + k_nl*l^10*phi^9;

Table 45. Mux Block Properties

Name	Inputs	Display Option
Mux	3	bar

Table 46. Outport Block Properties

Name	Port	Storage Class	Icon Display	Lock Scale	Unit	Var Size Sig	Signal Type	Ensure Outport Is Virtual	Source Of Initial Output Value	Output When Disabled	Must Resolve To Signal Object	Output When Un Connected	Output When Unconnected Value	Vector Params As 1DFor Out When Unconnected	Used By Blk
ddphi	2	Auto	Port number	off	inherit	Inherit	auto	off	Dialog	held	off	off	0	off	mnl/M2, Multiply
PHI	1	Auto	Port number	off	inherit	Inherit	auto	off	Dialog	held	off	off	0	off	Multiply
phidphi2	3	Auto	Port number	off	inherit	Inherit	auto	off	Dialog	held	off	off	0	off	mnl/M2.

Table 47. Product Block Properties

Name	Inputs	Multiplication	Collapse Mode	Collapse Dim	Input Same DT	Out Data Type Str	Lock Scale	Rnd Meth	Saturate On Integer Overflow
Multiply	3	Element-wise(.*)	All dimensions	1	off	Inherit: Inherit via internal rule	off	Floor	off

Table 48. Sum Block Properties

Name	Icon Shape	Inputs	Collapse Mode	Collapse Dim	Input Same DT	Accum Data Type Str	Out Data Type Str	Lock Scale	Rnd Meth	Saturate On Integer Overflow
Sum2	round	++--	All dimensions	1	off	Inherit: Inherit via internal rule	Inherit: Inherit via internal rule	off	Floor	off

Table 49. UnitDelay Block Properties

Name	Input Processing	State Storage Class
Unit Delay	Elements as channels (sample based)	Auto

Appendix

Table 50. Block Type Count

BlockType	Count	Block Names
Outport	22	Chirp, Custom, El Centro, IC, Impulse, Sine, ddXg, Acc_NL, X_1, dX_1, ddX_1, dx1, x1, X_2, dX_2, ddX_2, Disp_NL, PHI, ddphi, phidphi2, Vel_NL, X_NES
Gain	19	Gain1, Gain3, Gain4, Gain5, Gain, c1+c2, c2, k1+k2, k2, c2/M2, c22, k2/M2, k22, mnl/M2, mnl/M2., 1/Ig, cL2/Ig, mnl/Ig, mnl/Ig.
Inport	11	ddxb, dx2, x2, ddphi, ddxb, dx1, phidphi2, x1, ddx2, mnddxb, ddx_g
ToWorkspace	9	Input, time, Displacements, Displacements1, Displacements2, To Workspace, To Workspace1, To Workspace2, To Workspace3
Constant	7	Constant, switch constant, Constant, Constant, k_lin, k_nonlin, l
SubSystem	6	Base Excitation, BASE INPUT, Subsystem, DOF1, DOF2, Subsystem
Integrator	6	Integrator, Integrator1, Integrator2, Integrator3, Integrator4, Integrator5
Selector	5	Selector, MIMO, Selector1, Selector2, Selector3
Sum	4	Sum, Sum, Sum1, Sum2
Mux	4	Mux, Mux1, Mux2, Mux
Step	3	StepDwn, StepUp, Step

Product	3	Product, Multiply, Multiply
UnitDelay	1	Unit Delay
StateSpace	1	Primary Building
Sin	1	Sine Wave
Scope	1	Scope
MultiPortSwitch	1	Input Selector
MATLAB Function	1	MATLAB Function
FromWorkspace	1	From Workspace
FromFile	1	From File1
Clock	1	Clock
Chirp (m)	1	Chirp1
BusCreator	1	Bus Creator
Analog Filter Design (m)	1	Analog Filter Design

Table 51. Model Variables

Variable Name	Parent Blocks	Calling character vector	Value
Fs	Chirp1 Chirp1	`1/Fs` `Fs`	256

Table 52. Model Functions

Function Name	Parent Blocks	Calling character vector
Tf	Chirp1 Step	`Tf` `Tf`

pi	Integrator
	Integrator1
	Integrator2
	Integrator3
	Integrator4
	Integrator5
	Analog Filter Design
	Chirp1
	Sine Wave
	Integrator
	Integrator1
	Integrator2
	Integrator3
	Integrator4
	Integrator5
		`-pi`
		`-pi`
		`-pi`
		`-pi`
		`-pi`
		`-pi`
		`12*2*pi`
		`pi/2`
		`pi/2`
		`pi`
		`pi`
		`pi`
		`pi`
		`pi`
		`pi`

VITA

VITA

Christian E. Silva

School of Mechanical Engineering
Purdue University
West Lafayette, IN

Phone: +593 (98) 679 0598
Email: chrsilvas@gmail.com
ORCID iD: 0000-0003-2176-4918

Education

2014–2018 Ph.D., Mechanical Engineering, Purdue University

Dissertation Title: Design, Modeling and Experimental Validation of a Nonlinear Energy Sink Based on a Cantilever Beam with Specially Shaped Boundaries

Supervisors: Shirley J. Dyke and James M. Gibert

2011–2013 M.S.M.E., Mechanical Engineering, Purdue University

Thesis Title: Development, Numerical Demonstration and Experimental Verification of a Method for Model Updating of Boundary Conditions

2003–2007 B.Sc., Mechanical Engineering, Escuela Superior Politécnica del Litoral. Guayaquil-Ecuador

Appointments

2014–2015 Teaching Assistant, Mechanical Engineering, Purdue University

2013–2015 Research Assistant, Intelligent Infrastructure Systems Lab, Purdue University

Selected Honours and Awards

2017 The Graduate School. Purdue University (West Lafayette, IN). Bilsland Dissertation Fellowship for outstanding Ph.D. candidates.

2016 School of Mechanical Engineering. Purdue University (West Lafayette, IN). "Estus H. & Vashti L. Magoon" Award in recognition of excellence in academic achievement.

2014 SENESCYT (National Secretariat of Science, Technology and Innovation of Ecuador). Ph.D. grant under the Universities of Excellence Program.

2011 SENESCYT (National Secretariat of Science, Technology and Innovation of Ecuador). M.Sc. grant under the Universities of Excellence Program.

Publications

Preprint URLs available at ***https://orcid.org/0000-0003-2176-4918***

Journal Publications

1. **Silva, C.E.**, Maghareh, A., Tao, H., Dyke, S.J., & Gibert, J.M. (2019). Evaluation of energy and power flow in a nonlinear energy sink attached to a linear primary oscillator. Journal of Vibration and Acoustics, 141(6):061012. DOI: 10.1115/1.4044450

2. **Silva, C.E.**, Gomez, D., Maghareh, A., Dyke, S.J., & Spencer Jr., B.F. (2020). Benchmark control problem in real-time hybrid simulation. Mechanical Systems and Signal Processing. 135(January 1):106381. DOI: 10.1016/j.ymssp.2019.106381

3. Maghareh, A., **Silva, C.E.**, & Dyke, S.J. (2018). Parametric model of servo-hydraulic actuator coupled with a nonlinear system: Experimental validation. Mechanical Systems and Signal Processing. 104 (May 1): 663–672. DOI: 10.1016/j.ymssp.2017.11.009

4. Maghareh, A., **Silva, C.E.**, & Dyke, S.J. (2018). Servo-hydraulic actuator in controllable canonical form: Identification and experimental validation. Mechanical Systems and Signal Processing. 100(February 1):398-414. DOI: j.ymssp.2017.07.022

Conference Papers

1. **Silva C.E.**, Dyke, S.J. (2015). Numerical study and experimental validation of a method for model updating of boundary conditions in beams. In: Caicedo J., Pakzad S. Dynamics of Civil Structures, Volume 2. Conference Proceedings of the Society for Experimental Mechanics Series. Springer, Cham. DOI: 10.1007/978-3-319-15248-6-29

2. Gomez, D.., **Silva, C.E.**, Dyke, S.J. & Thomson, P. (2015). Interactive Platform to Include Human-Structure Interaction Effects in the Analysis of Footbridges. In: Caicedo J., Pakzad S. (eds) Dynamics of Civil Structures, Volume 2. Conference Proceedings of the Society for Experimental Mechanics Series. Springer, Cham: DOI: 10.1007/978-3-319-15248-6-6

Professional Activities

- Reviewer, Mechanical Systems and Signal Processing, 2018.
- Reviewer, Structural Control and Health Monitoring, 2019.